Superconducting Nanowire Single Photon Detectors (SNSPDs) properties and LIDAR applications

UNIVERSITÀ DEGLI STUDI
DI NAPOLI FEDERICO II

Daniela Salvoni

Supervisor: Prof. G.P. Pepe
Coordinator: Prof. S. Capozziello

PhD Thesis
32^o cycle - 2017/2020

List of constant and acronyms

Constants

k_B	Boltzmann constant	$8.617333262145 \times 10^{-5}$ $eV \cdot K^{-1}$
c	Speed of the light	299 792 458 m/s
$\hbar$	Planck constant	$4.135667696 \times 10^{-15}$ $eV \cdot s$
e	electron charge	$1.60217662 \times 10^{-19}$ C
m_e	electron mass	$9.10938356 \times 10^{-31}$ Kg
π	Archimedes'constant	3.14159...
Φ_0	Magnetic quantum flux	$2.067833848 \times 10^{-15}$ Wb
γ	Euler Mascheroni constant	0.57721...
μ_0	Vacuum permeability	1.256637×10^{-6} H/m
ϵ_0	Vacuum permittivity	$8.8541878128 \times 10^{-12}$ F/m

Acronyms

ALA	Advanced Lidar Applications
APD	Avalanche Photodiode
BCS	Bardeen-Cooper-Schrieffer
BKT	Berezinskii-Kosterlitz-Thouless
BS	Beam Splitter
CR	Count Rate
DC	Dark Counts
DC	Direct Current
DCR	Dark Count Rate
DIAL	Differential Absorption Lidar
DOS	Density of States
EBL	Electron Beam Lithography
GL	Ginzburg-Landau
HD	Heterodyne Detection
IPH	Inter-Pulse Histogram
LO	Local Oscillator
NEP	Noise Equivalent Power
NIR	Near Infrared
MMF	Multi Mode Fibre
MPS	Multiple Phase Slip
MQT	Macroscopic Quantum Tunnelling
PBL	Planetary Boundary Layer
PBS	Polarizing Beam Splitter
PMT	Photomultiplier Tube
PNR	Photon Number Resolving
PS	Phase Slip
qp	quasi particle
QPS	Quantum Phase Slip
RIE	Reactive Ion Etching
SC	Superconductor
SCD	Switching Current Distribution
SDE	System Detection Efficiency
SMF	Single Mode Fibre
SNR	Signal to Noise Ratio
SNSPD	Superconducting Nanowire Single Photon Detector
SPAD	Single Photon Avalanche Photodiode
SPD	Single Photon Detector
TES	Transition Edge Sensor
TOF	Time of Flight
UV	Ultraviolet
VAP	Vortex Anti-vortex Pair
VH	Vortex Hopping
VIS	Visible

List of Figures

List of Tables

Contents

Introduction

Single photon sources and detectors are important for several applications, especially quantum communication and computing [17]. Due to high-sensitivity, they unavoidably affected other fields such as high energy physics, remote sensing technologies, medical imaging, and many other fields where high timing resolution and high sensitivity to low photon levels are required.
Depending on the preferred wavelength and on the specific application, different SPDs can be used; Silicon based SPDs can reach 80% efficiency in visible domain (λ=600-1100 nm), while InGaAs avalanche photodiodes are recommended for $\lambda = 1.3\mu m$ and $\lambda = 1.5\mu m$, wavelengths widely used in telecommunication applications. APD efficiency in this regime is low while the noise is very high, resulting in a low signal to noise ratio which makes the use of these sensor limited to intense signals applications.
In this scenario, superconducting detectors, such as TES and SNSPD, play a crucial role in the improvement of detection techniques in near-infrared (NIR) wavelength domain. Although a temperature below 10 K is needed for operation, this is not a obstacle as it is possible to use liquid helium to reach this temperature as well as closed-cycle cryostates which make low temperatures affordable.
The first Superconducting Nanowire Single Photon Detector (SNSPD) was realized in 2001 [19, 20] but, since that moment, many improvements have been reached. The most impressive are near 100% system detection efficiency, few picoseconds response time, less than 1cps dark count rate, few nanoseconds dead-time; the last feature affects the maximum count rate which can be pushed up to 1GHz [4, 18, 21]. Moreover, due to a few meV energy gap, these quantum sensors exhibit a wide range of spectral sensitivity, from UV to IR, up to $\lambda \sim 5\mu m$ [5].
Besides the applications cited above, such performances promote SNSPD as one of the best candidates also for Lidar applications in the IR wavelength domain.
Light detection and ranging (Lidar), is a remote sensing technique introduced in 1963 [22] and used for atmosphere monitoring and molecules and aerosols profiling. Aerosols play a crucial role in climate changes and greenhouse effect. Indeed, they affect the radiative bal-

ance of the Earth by scattering and absorbing solar and terrestrial radiation and also act as condensation nuclei for water vapour, affecting fog, mist and rains.
It is possible to measure the vertical and horizontal aerosol content with elastic Lidar operating both in visible and NIR wavelengths (532nm-1064nm); moreover, further information can be obtained with a polarization Lidar which analyses the particles shape. However, the study of aerosols with Lidar systems, can be further improved with the use of longer wavelengths. That enhancement would enlarge the detectable species number and the maximum reachable distance, as the scattering (and hence the attenuation) due to the molecular composition of the atmosphere can be neglected in this range. The use of IR wavelength is limited by detector noise and low efficiency, hence, the use of SNSPD would give a significant contribution in this field.

Within the framework of European flagship Horizon 2020, whose mission is to promote innovation and technological advancement, Italy launched *PON Research and Innovation* project and, every year from 2014 to 2020, offered special PhD programs on innovative themes. The work presented here was supported by this special funding and the mission was to combine Lidar technology and SNSPD detectors for a measurement at $\lambda > 1\mu m$, for the reasons presented above. This project was guided by University of Naples *Federico II*, the company Advanced Lidar Application (ALA) S.r.l. whose mission is the development of Lidar systems for remote sensing, and Beijing Research Institute of Telemetry (BRIT), specialized in aircraft Lidar setups.

The work presented here was hence devoted to the realization of SNSPD detectors and of a transportable measurement setup to ease the adaptability to different Lidar systems. In order to pursuit that purpose, many superconducting materials for the realization of SNSPD have been tested and a special study of dark counts was carried on. Moreover, different techniques for the coupling with light have been experimented.

Outline

Chapter 1 is dedicated to the fundamental basics of the theory of superconductivity and to the definition of important parameters, such as coherence length, penetration depth, energy gap, critical current and so on. Then, a description of SNSPD detection principles and a definition of detector properties such as timing jitter, system detection efficiency, dead time and dark count is provided.

The transportable measurement setup and the fabrication process details used to produce the SNSPD are presented in Chapter 2. Here also the characterization of different materials and geometries is explored. In details, MoSi, NbRe, NbN detectors have been fabricated and tested in the geometry of simple micro-strips, nanowires, meanders and parallel meanders.

The ideal detector should have zero dark counts but this value is unattainable. Anyway, it is reasonably acceptable that the dark count rate can be lowered if their generation mecha-

nism is understood. In Chapter 3 a study of dark count rate models and experimental results are presented. A special focus is given to the measurement of switching current distributions in NbTiN and NbN SNSPD from 0.3K to 4K.

Chapter 4 is dedicated to the presentation of Lidar technique. After a brief introduction, elastic, Raman, Doppler and DIAL Lidars systems are described. Later on, the detection mechanism of the most used detectors for Lidars, namely APDs and PMTs, is provided.

In Chapter 5 the results of a Lidar measurement with a NbTiN SNSPD are presented. First, a prototype system for the measurement of hard target distance at $\lambda = 1550nm$ was realized in order to test the electronic, the acquisition programs, the cryogenic measurement setup and the detector. After that, the transportable system was used to measure the aerosol content with MALIA system in the shared lab of ALA and University of Naples Federico II. In this chapter the activities held at BRIT are also presented.

Due to the outbreak of coronavirus, the last measurement campaigns in China and with MALIA have been suspended and postponed to better times.

CHAPTER 1

Superconducting Nanowire Single Photon Detectors

Abstract: Superconducting nanowire single photon detectors (SNSPD) offer single photon detection in a wide range of wavelengths, from visible to infrared with high detection efficiency, low dark counts rate, high speed (small dead time) and small timing jitter. The first SNSPD was realized about twenty years ago by Gregory Gol'Tsman, Roman Sobolewski and colleagues [19] with a 5 nm thick and 200 nm wide NbN nanowire. Since that moment lots of improvements of the device have been done.
In this chapter a description of the main feature of the SNSPD will be provided, together with a brief overview of the theory of Superconductivity. The most important results achieved in the field of SNSPD during the last years are also presented.

1.1 A Description of the Superconducting State

In 1911 Heike Kamerlingh Onnes, at the Physics Labs of Leiden University, observed the abrupt drop to zero of the DC-resistance of the mercury when cooled below the temperature $T = 4,15K$ [23]. He discovered in this way a new solid state physics phenomenon, the superconductivity. He also found, a few years later, that at $T = 2,45K$ there is a threshold in the value of the current that can pass through the mercury (about $10^3 A/mm^2$) and, when this value is passed, the superconductor returns in the normal electrical state [24].
About twenty years later, the German Physicists Meissner and Ochsenfeld demonstrated a unique property of superconducting materials: they repeal the magnetic fields, or equivalently, they exhibit perfect diamagnetism [25]. The last property is not an effect of the zero-resistance value and a new theory was needed at that time to describe the *new state of matter* just discovered.
The first attempt of providing a theory which explains the phenomenon of superconductivity and Meissner effect was introduced by the two brothers Fritz and Heinz London in 1935. The

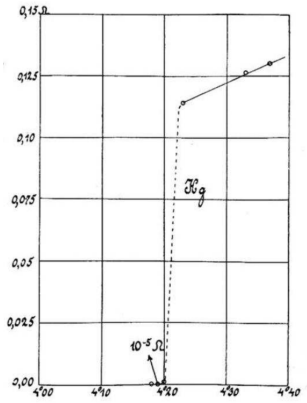

Figure 1.1: Superconducting transition in Mercury measured by K. Onnes in 1911.

next theoretical advance came in 1950 when Ginzburg and Landau gave a phenomenological description of superconductivity in terms of a phase transition order parameter. These two theories give a macroscopic description of the phenomenon.
In 1957 a complete microscopic theory of superconductivity was proposed by Bardeen, Cooper and Schrieffer [26]. In the picture presented in BCS theory, below the critical temperature T_C the electrons in a superconductor are paired in a bosonic state called *Cooper pair*. In this state, the two electrons have opposite spins and wave vectors and the interaction between them is mediated by virtual phonons.
As Cooper pairs are bosons, at low temperature they form a condensate in the energetic quantum state E_F.
In what follows, I will describe the main features of superconductors, with a special focus on the interesting characteristics for their use as detectors.

The theory of superconductivity phase transition

The phase transition between the superconductive and normal state can be described in terms of a order parameter; its value goes from zero in the symmetric (disordered) phase to a finite value in the ordered phase. In the case of superconductivity, we can consider as order parameter either the pseudo wave function Ψ in the picture of Ginzburg - Landau theory, either the energy gap in microscopic BCS theory. It has been demonstrated that the former is an approximation of the latter [27].

In **GL theory** [28], the current is carried by super electrons that have charge, mass and number density related to the electron counterpart as follows

$$e^* = \pm 2e \qquad m^* = 2m \qquad n_s^* \leq \frac{1}{2} n_e \tag{1.1}$$

and the order parameter $\psi(\mathbf{r}) = |\psi(\mathbf{r})|e^{i\phi}$ is a complex pseudo wave function, whose square module $n_s = |\psi|^2$ represents the local density of superconducting electrons. In GL theory,

close to the transition and below T_C, the Gibbs free energy can be expanded as a local function of the order parameter

$$G_s \simeq G_n + \frac{1}{V}\int d^3\mathbf{r}\left[\frac{1}{2m*}(-i\hbar\nabla + e^*A)\Psi^* \cdot (i\hbar\nabla + e^*A)\Psi + \frac{B^2(\mathbf{r})}{2\mu_0} + \right.$$
$$\left. -\mu_0 H(\mathbf{r}) \cdot M(\mathbf{r}) + a\Psi\Psi^* + \frac{1}{2}b\Psi\Psi^*\Psi\Psi^* + ...\right] \quad (1.2)$$

and, at equilibrium, the current flowing in the superconductor distributes in such a way to minimize the total free energy. In Eq.(1.2), a and b are two functions of the temperature, B is the external magnetic field and A the magnetic vector potential.
The minimization of Gibbs free energy with respect of small variations of Ψ, provides two coupled differential equations

$$\begin{cases} \frac{1}{2m*}(\hbar^2\nabla^2\Psi - 2i\hbar e^* A\cdot\nabla\Psi + e^{*2}A^2\Psi) - a\Psi + b|\Psi|^2\Psi = 0 \\ \nabla\times(\nabla\times A) + \frac{i\hbar e^*}{2m*}(\Psi^*\nabla\Psi - \Psi\nabla\Psi^*) + \frac{e^{*2}}{m^*}A|\Psi|^2 = 0 \end{cases}$$

that, once solved, provide a description of the superconducting state at equilibrium in terms of the order parameter.
The first GL equation is analogous to the Schroedinger equation for a free particle with a non linear term. The second equation can be rewritten with the use of the fourth Maxwell equation as

$$j_s = \frac{e^*\hbar}{i2m^*}(\psi^*\nabla\psi - \psi\nabla\psi^*) - \frac{e^{*2}}{m^*c}|\psi|^2 A \qquad j_s = \nabla\times(\nabla\times A) \quad (1.3)$$

and these equations describe the spatial variation of super-electrons number density, the supercurrent j_s and the influence of an external magnetic field on n_s and j_s.

With microscopic **BCS theory** the weak attractive interaction between electron which make favourable the formation of a Cooper pair is explained. Within the formalism of second quantization, one can demonstrate that the formation of Cooper pairs is energetically favourable with respect to the ground state of an electron gas (Fermi sea). The formation of Cooper pairs creates an energy gap $\Delta(T)$ in the electrons density of state (DOS) where there are no electron excited states.
Every input higher than 2Δ will break a Cooper pair into quasiparticles (qp)[1] with energy above $E_F + \Delta$.
The energy gap Δ plays the role of order parameter in the framework of BCS theory. Its

[1] A solid is composed by protons and neutrons of the lattice and electrons. The mass and charge of these particles is well defined in the absence of interaction. In the case of interacting particles the mass and charge are *dressed*, i.e. increased, by the interaction as predicted by quantum field theories. In the case of weakly interacting particles one refers to *quasi particles*. In this case hence, we will refer to quasi particles in the meaning of electrons produced after the braking of a Cooper pair state.

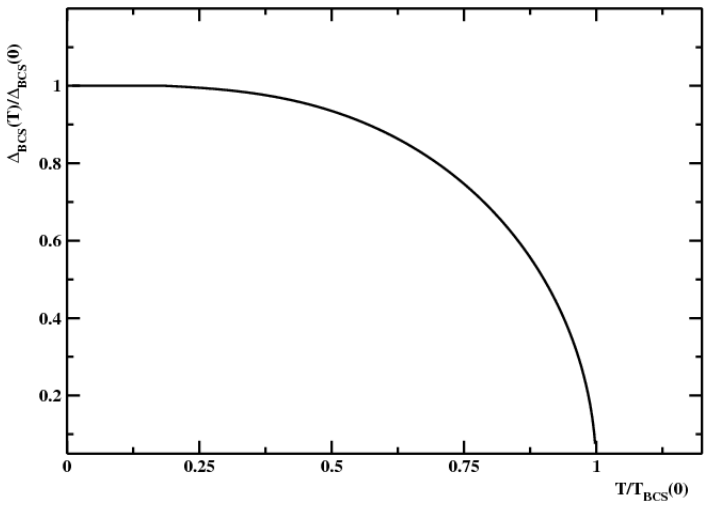

Figure 1.2: Temperature dependence of BCS energy gap.

value at $T = 0$ and $T = T_C$ can be calculated [28] and we report here just the resulting expressions

$$\Delta(T = 0) = 1,764 k_B T_C \qquad \Delta(T \to T_C) \approx 3,06\sqrt{1 - \frac{T}{T_C}}. \tag{1.4}$$

The energy gap plays also an important role in the use of superconductors materials as detectors. Indeed, it has been shown in [20] that the minimum detectable energy depends also on the energy gap.

Characteristic Lengths

The important scales in superconductivity are determined by two characteristic lengths : coherence length and penetration depth.

As we already mentioned at the beginning of this chapter, a superconductor expels magnetic field and this phenomenon is called Meissner effect. Inside the bulk superconductor the magnetic field is totally repealed while at the surface an applied magnetic field can penetrate slightly for a thickness of the order of **London penetration depth** λ_L. The supercurrent flowing in the surface redistributes in order to repeal the external magnetic field generating a *shielding current*.
The magnetic field can penetrate inside the superconductor for a short thickness and its value can be calculated from its value at the surface B_0 by the exponential law [28]

$$B(x) = B_0 e^{-x/\lambda} \tag{1.5}$$

where x is the distance from the surface.
A theoretical estimation of λ is $\lambda_L(T) = \sqrt{m/\mu_0 e^2 n_s}$ but the experimental data show that

this expression provides just a lower limit and λ is always bigger than λ_L.
London penetration depth also depends on the temperature trough the experimental law

$$\lambda_L(T) = \frac{\lambda_0}{\sqrt{1-(T/T_C)^4}} \tag{1.6}$$

where λ_0 is the penetration depth measured at $T = 0K$.

The **coherence length** ξ_{GL} represents the distance over which the order parameter ψ changes appreciably. More precisely, the Cooper pair state is rigid and it takes energy to change it, the more abrupt changes, the more energy is required. This characteristic of the superconducting state is expressed through the coherence length.
In BCS theory it is possible to estimate the Cooper pair size ξ as a function of its value at $T = 0$ as follows

$$\xi_0 = \frac{\hbar v_F}{\pi \Delta_0} \qquad\qquad \xi(T) = \frac{\xi_0}{\sqrt{1-T/T_C}} \tag{1.7}$$

where v_F is the Fermi velocity and Δ_0 is the energy gap.
In pure superconductors, ξ_{GL} depends on ξ_0 according with the relations [29]

$$\xi_{GL} = 0,74 \cdot \frac{\xi_0}{\sqrt{1-T/T_C}} \tag{1.8}$$

The coherence length represents a measure of the spatial variation of the density of superconducting electrons. A material with a short coherence length can accommodate a rapidly changing n_s while maintaining the superconductive state.

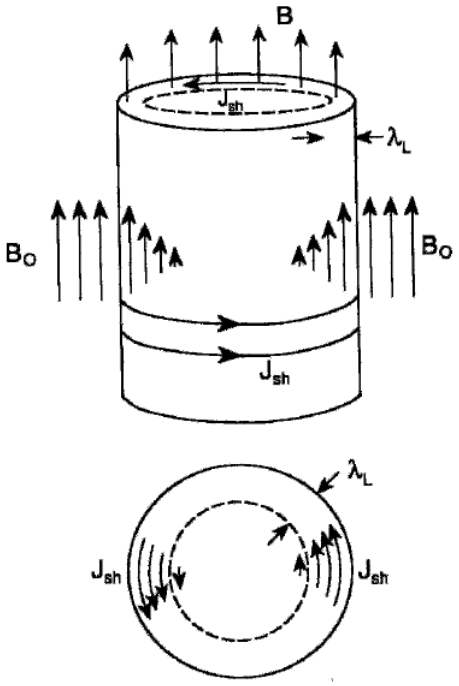

Figure 1.3: Type I superconducting cylinder (cooled in absence of external field) in an external magnetic field B_0. The shielding currents j_{sh} and magnetic field are shown. The London penetration depth λ_L is also indicated.

Depending on the material behaviour under the effect of an applied magnetic field, superconductors can be classified into two categories: type I and type II. In terms of the parameter $\kappa = \lambda/\xi$ one can distinguish the two families that express whether or not the superconductor can accommodate changes in the condensate on length scales shorter than the magnetic screening λ

$$\begin{cases} \kappa < \dfrac{1}{\sqrt{2}} & Type\ I \\ \kappa > \dfrac{1}{\sqrt{2}} & Type\ II \end{cases}$$

In type I superconductors, magnetic field is repealed while its value remains below $B_C(T)$, that is the critical field; above it, the superconducting state is destroyed.
In type II superconductors, once the critical field B_{c1} is passed, magnetic vortices with a flux value of $\Phi_0 = h/2e$ can penetrate inside the material. In this way, superconductive state remains unbroken until the second critical field value B_{c2} is passed.
Among the superconductors, pure elements are type I SC (Niobium excluded) and compounds are type II SC.
The coherence length is of the order of hundreds nanometres for Type I SC and a few nanometres in the case of Type II SC.
The thickness of a superconductor, that is a crucial feature for detectors fabrication, affects London penetration depth. In the case of very thin films, that is when the thickness is $d \ll \lambda$, we must consider hence the following expressions [30]

$$\lambda \approx \lambda_0 \sqrt{\frac{\xi}{d}} \qquad (d \leq \xi \qquad and \qquad B \parallel to \ \ film \ \ surface) \tag{1.9}$$

$$\lambda_\perp \approx \frac{\lambda^2}{d} \qquad (d \ll \lambda \qquad and \qquad B \perp to \ \ film \ \ surface) \tag{1.10}$$

Critical current and critical temperature

As mentioned before, the superconducting state can be broken if one of the relevant variables, that are current density, temperature and magnetic field, overcomes the critical value. This is sketched in Fig.(1.4).

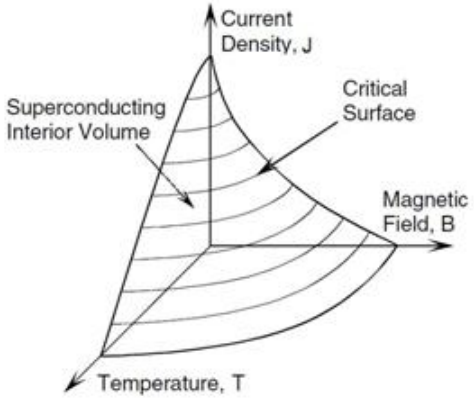

Figure 1.4: Critical surface of a type I superconductor.

The supercurrent flowing in the superconductor generates a magnetic field and hence its critical value j_c depends on B_c. For that reason also the current concentrates on the surface and than spatially decays with exponential law

$$j(x) = j_0 e^{-\frac{x}{\lambda}}. \tag{1.11}$$

The geometric parameter embedding the superconductor response to the magnetic field is London penetration depth, that depends on the temperature. Current density dependence on magnetic field, penetration depth and temperature, can be summarized in the useful expressions presented in [28] which are:

$$j_c = \frac{\Phi_0}{3\sqrt{3}\pi\mu_0\lambda_L^2\xi} = \frac{2\sqrt{2}B_c}{3\sqrt{3}\lambda_L\mu_0} \qquad j_c(T) = \frac{8\sqrt{2}B_c(0)}{3\sqrt{3}\lambda_L(0)\mu_0}\left(1-\frac{T}{T_c}\right)^{\frac{3}{2}} \tag{1.12}$$

and in the case of type II superconductors the field B_{c2} has to be considered.
The theoretical value calculated from Eq.1.12 is often called *depairing current* and it represents the upper limit of the maximum reachable current density [31]. The effectively measured value is called critical current density.

Another important property of a superconducting material is its critical temperature, T_c, the temperature below which the material is superconducting. The known range of critical temperatures is from a fraction of 1 K to slightly above 100 K. Superconductors with critical temperatures near this higher limit are commonly known as "high-temperature superconductors".
The critical temperature value depends on the density of states $D(0)$ and on the phonon interaction potential V_0 through the equation

$$k_B T_C = \frac{2e^{\gamma}}{\pi}\hbar\omega_D e^{-1/D(0)V_0} \tag{1.13}$$

In BCS theory it is possible to write the following equation for the energy gap

$$\Delta(0) = 2\hbar\omega_D e^{-1/D(0)V_0} \tag{1.14}$$

and hence we can write an expression for the critical temperature independent of the density of states

$$\Delta(0) = 1,76 k_B T_c. \tag{1.15}$$

According to Eq.(1.14), the critical temperature is proportional to the Debye frequency ω_D which in turn is inversely proportional to the square root of the atomic mass M:

$$T_c \propto \omega_D \propto \frac{1}{\sqrt{M}} \tag{1.16}$$

This law is in good agreement with experimental results obtained on isotopes.

The kinetic inductance

The kinetic inductance plays an important role in superconducting thin films. It is due to the kinetic energy of charge carriers rather than to the magnetic field. The kinetic energy, in

the simple case of a wire of length l and cross section A in which all carriers have the same velocity, can be evaluated classically [32]

$$E_K = \frac{1}{2}Mv^2 = \frac{1}{2}\left[\frac{m_e l}{n_s A e^2}\right] i^2 \tag{1.17}$$

and n_s is the electrons'number density and i is the current that flows in the wire.
Moreover, the energy stored in an inductor is

$$E_L = \frac{1}{2}Li^2 \tag{1.18}$$

hence we can define the kinetic inductance as

$$L_K = \frac{m_e l}{n_s A e^2} = \frac{l}{A}\mu_0\lambda_L^2 \equiv \frac{l}{A}\mathcal{L}_\mathcal{K} \tag{1.19}$$

where we introduced the inductivity $\mathcal{L}_\mathcal{K}$.
Typically, in normal metals and at low frequencies, the kinetic inductance is neglected because the energy E_K is quickly dissipated through collisions. This term becomes relevant in thin superconducting films ($d \ll \lambda$) and dominates over the magnetic inductance.
For thin films it can be useful to introduce also the sheet inductance $L_\square$ because it is a quantity that is independent of the specific geometry:

$$L_K = \frac{l}{w \cdot d}\mathcal{L}_\mathcal{K} = N_\square L_\square \tag{1.20}$$

here we called $N_\square$ the number of squares contained in the thin film.

1.2 Detection mechanism

In 1996 [33] a new type of detectors, based on ultra-thin metallic films, was proposed. A few years later, the first Superconducting Nanowire Single Photon Detectors (SNSPD) was fabricated and used to detect $\lambda \sim 800nm$ photons [19].
An SNSPD consists of a very thin (around 5nm) superconducting nanowire[2] with an approximate width of 50-100 nm deposited on a substrate. In order to increase the detector sensitive surface, the nanowire is folded and it is typically given a meander geometry (Fig.1.5).
Due to the superconductor thinness, the superconducting state is fragile and it can be broken by an incident photon with energy E_γ of a few eV and the precise value depends on the energy gap; in the case of NbTiN, it is about $E_g \approx k_B T_C \sim 5meV$ [34].

[2]In recent times, it was decided to rename these detectors as Superconducting Nano-stripes Single Photon Detectors, in order to make a distinction among wires which have both thickness t and width w of the order of a few nanometres $t \sim w \sim 1nm$ and wires in which $t \sim 1nm$ and $w \sim 100nm$, referred now as nano-stripes. Anyway, as the modification of the acronyms was agreed just in recent times and in literature we still name the detectors as *Nanowire*, I will maintain here the old nomenclature.

Figure 1.5: Superconductor nanowire single photon detector in a square meander geometry.

In the operating regime, the detector is cooled below the critical temperature T_c and it carries a direct current I_b close to the critical current I_c. According with the model presented in [2,19,20,35], when a photon is absorbed, a resistive *hot-spot* is formed and it forces the current to flow at the nanowire edges; as a consequence of this constriction, the current density at the edges may exceed the critical value and a fraction of the wire switches to the normal state. This transition is accompanied by the emission of a voltage pulse that exponentially decreases with a time constant which depends on the readout circuit.
In this section we provide a qualitative description of photon detection mechanism.

Non-equilibrium superconductivity

The superconducting detector consists of three coexistent subsystems: Cooper pairs, quasiparticles (QP), phonons (coming from the substrate and superconductor lattices). When a energetic photon enters the system, the equilibrium between these particles in the superconductor is destroyed.
The energy downconversion in the detector after photon absorption has been studied in several works and here just a simplified sketch is presented. According with the models presented in Ref. [3, 20, 35–37] photon downconversion occurs in three steps whose characteristics are sketched in Fig.1.6 .

In the first stage the photon energy $E_\gamma > 2\Delta$ breaks Cooper pairs, resulting in the formation of fast photoelectrons which ionize atoms along their trajectory generating a certain number of secondary *hot electrons*; at this point strong electron-electron scatterings occur with a characteristic interaction time τ_{ee}. After a few τ_{ee}, the hot electrons thermalize to an energy $E_1 \approx \omega_D$ (Debye frequency) defining the end of the first stage.
During the second stage, electron-phonon scattering, having a characteristic time $\tau_{ep} < \tau_{ee}$, becomes more probable and a large amount of energetic phonons is released around the Debye frequency. At the end of this thermalization process high energy phonons and quasiparticles have similar energies of $E_2 \approx 3\Delta$.
At this point more than one process occur at the same time:

- phonons break the Cooper pair
- two quasiparticles recombine in Cooper pair and a phonon with energy $E_{ph} = 2\Delta$ is emitted
- phonons escape in the substrate with a characteristic time τ_{es}.

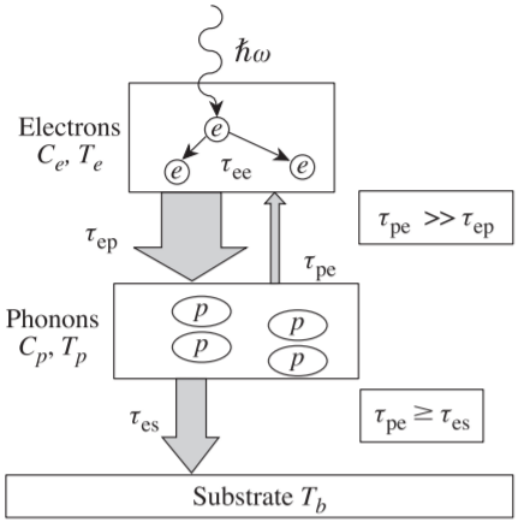

Figure 1.6: Recombination process occurring after the absorption of a photon [1].

There is a fourth stage during which phonons energy cannot break Cooper pairs $E_4 < 2\Delta$ and the system returns to the equilibrium state though phonon-phonon scattering and phonons escape in the substrate.
The values of E_1, E_2, τ_{es}, τ_{ee}, τ_{ep}, depend on the temperature, on the material[3], and on the substrate/superconductor lattice matching.

Hot spot model

It has been demonstrated in [20] that it is possible to detect a photon with a SNSPD if its energy is bigger than[4]

$$E_{min} \approx \Delta N_0 k_B T_C D \tau_{th} \qquad ; \tag{1.21}$$

when a photon satisfying this requirement hits the detector, it breaks the Cooper pairs and their number density n_s changes of δn_s. Below the critical temperature T_c the current density can be expressed as $I_b = n_s 2e\bar{v_s}wd$ where $\bar{v_s}$ is Cooper pairs mean velocity, $2e$ their charge and wd the cross section area. When Cooper pairs are broken, the supercurrent redistributes to keep the carriers mean velocity the same all over the cross-section and it becomes $I_b = 2e(n_s - \delta n_s)\bar{v_s'}wd$, where $\bar{v_s'} > \bar{v_s}$ (see Fig.1.7). If the carriers velocity exceeds the value $v_c = I_c/n_s wd$, a resistive hot spot is generated.
The condition on carriers velocity can be transferred in a condition on the critical number of QP to be created in order to overcome the critical current [2]

$$\delta N_c = (\delta n_s)_c V = \pi a w d n_s \left(1 - \frac{I_b}{I_c}\right) \approx \frac{\pi}{2} a w d N_0 \Delta(T, I_b) \left(1 - \frac{I_b}{I_c}\right) \tag{1.22}$$

[3]Some values of τ_{ep} are listed in [38]
[4]all the parameters meaning will be clarified in what follows

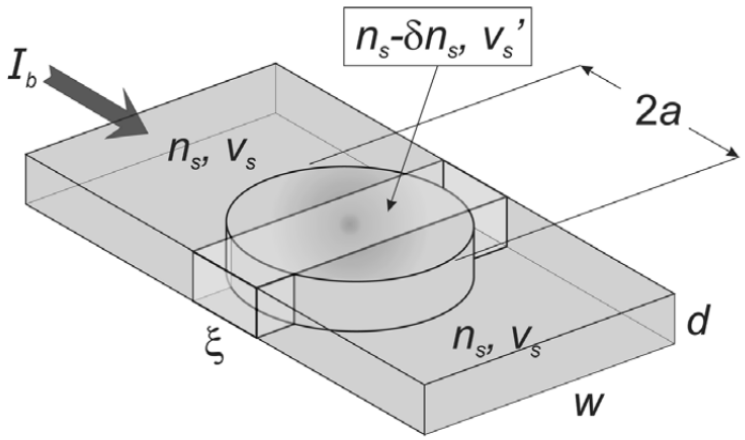

Figure 1.7: Hot spot formation in SNSPD due to Cooper pairs breaking as shown in [2].

where a is the hot spot radius and N_0 the DOS at E_F.

A more quantitative description of the hot spot model is presented in [20]. Here, when a photon is absorbed, Cooper pairs breaking leads to the formation of QP whose concentration can be expressed as a function of time and space as follows:

$$C(r,t) = \frac{M(t)}{4\pi Dd} \frac{\exp\left[\frac{-r^2}{4Dt}\right]}{t} e^{-t/\tau} + C_0; \tag{1.23}$$

here r is the distance from the site of the photon absorption, d, D and C_0 are, respectively, the detector thickness, the diffusion coefficient, the QP concentration at the equilibrium; τ is the effective cooling time which depends on phonons and electrons specific heats c_{ph} and c_e and relaxation times as follows

$$\tau = \tau_{ep} + \frac{c_e}{c_p}\tau_{es}. \tag{1.24}$$

$M(t)$ is a multiplicative factor depending on the thermalization time τ_{th}; rather precise results can be obtained with the simplified expression $M(t) = K(1 - e^{-t/\tau_{th}})$. The thermalization time is a function of the bias current and the temperature [39]. As shown in [40], at the time instant $t = 0,5\tau_{th}$, QPs concentration exceeds C_0, then they thermalize with the phonons and hot spot diffusion begins (stage II).
When the normal spot appears, the current is expelled from the resistive region and is confined between the hot spot and the edges; if in this volume the current density exceeds j_c, a resistive region arise. In the meanwhile, phonons thermalize and escape in the substrate (stage III) and the superconducting state is recovered (Fig. 1.8).
In the detection scheme presented by Semenov et *al.* in [20], the film thickness has to be $d << \sqrt{D\tau_{ee}}$ in order to have a uniform vertical QP distribution. The thickness plays hence

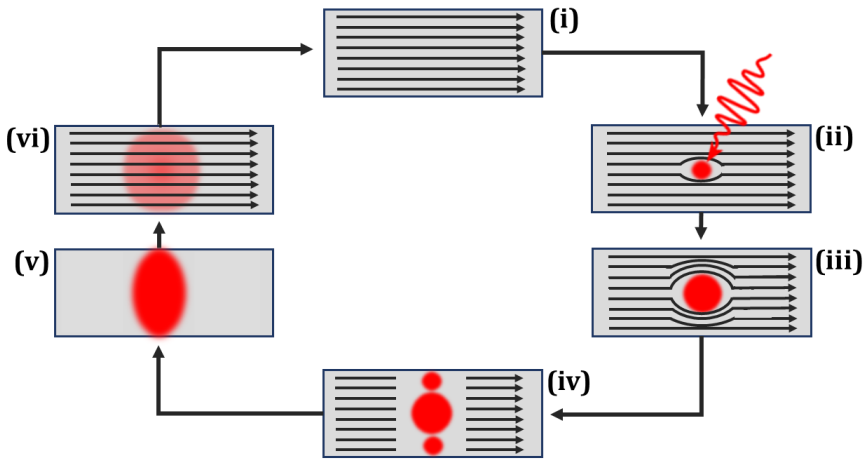

Figure 1.8: Hot spot detection mechanism scheme as presented in [3]. (i) The superconductor carries a current $I_b < I_c$.(ii) A photon is absorbed and an hot spot is generated. (iii) The hot spot diffuse and the current redistributes at the edges. (iv) The current density exceed the critical value j_c. (v) A normal resistive region arise and current flow drops abruptly. (vi) Phonons thermalize and QP recombines, superconductivity is recovered.

an important role because it has to be comparable with the cross section of the primary excitation phenomenon and, at the same time, it has to be small enough to guarantee the proper working of the detection mechanism and to get fast response. Moreover, the ability of the device to detect single photons is a trade-off between the quantum energy (hotspot size), bias current and width of the film whereas the fastness of response is related to the film thickness d, optimal reticular matching between film and substrate (small τ_{es}) and smallness of the coupling time.

1.3 Detector characteristics

SNSPDs combine many interesting features as high count rate, low timing jitter, high detection efficiency, low dark count rate, low dead time. In this section we provide a description of these properties giving an overview of the latest results.

Reset/Dead time

The dead time is the interval elapsed after detection during which the system is not able to record another event. Dead time limits the maximum count rate and the best values lay in the range of few nanoseconds.
The dead time is due mainly to the detection geometry and electronic readout circuit. There is also an intrinsic recovery time, that is the time required to restore the superconducting

state in the nanowire, but it lays in the picoseconds range and can be neglected at this level [19].

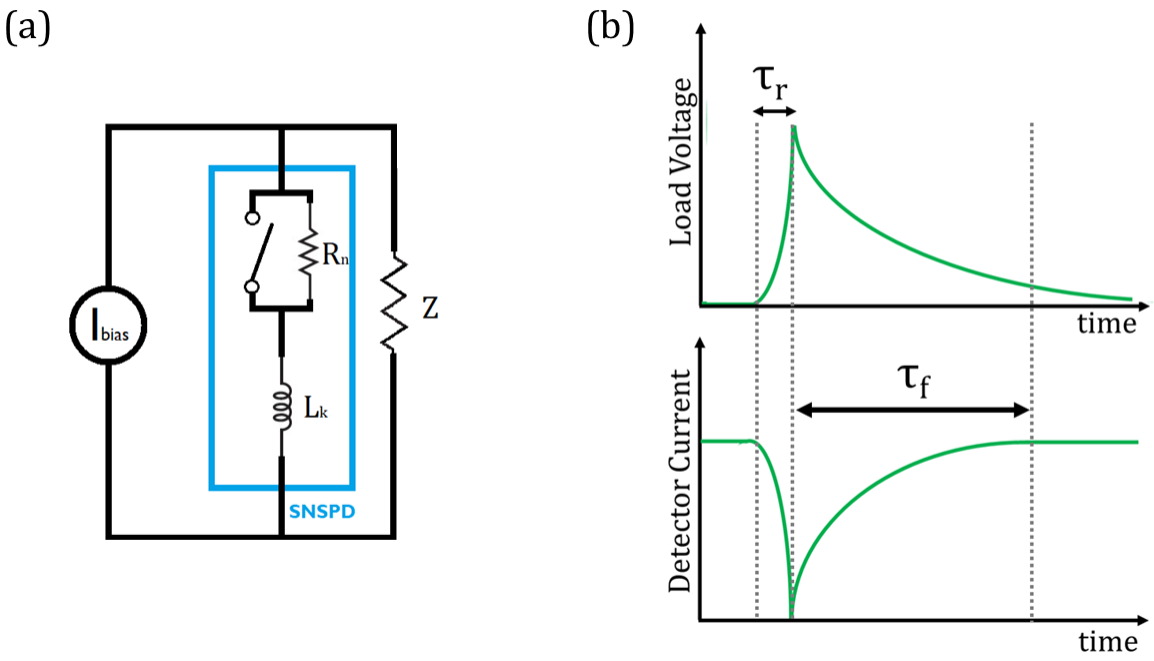

Figure 1.9: (a) Circuit model of SNSPD. (b) Detector current and load voltage during a photon detection event.

In Fig. 1.9 the electric model of SNSPD is drawn. The detector can be electrically represented though its kinetic inductance L_k in series with the parallel between a switch and a resistance R_n. Moreover, the detector is in parallel with Z, the readout circuit input impedance, whose typical value is 50Ω. When the detector is below the critical point, the switch is closed and the bias current I_b flows trough the inductance and the short; when the device switches in the normal state it is represented by the inductance in series with the normal resistance of the hot spot. It is assumed in this model that the normal region area is a small fraction of nanowire total length and, hence, it does not affect the kinetic inductance value.
The absorption of a photon is represented by the switch opening. When the detector switches, the current carried by the device decreases with the time constant $\tau_r = L_k/(Z + R_n)$ and it is diverted in the parallel load until it reaches the value $I_n = ZI_b(Z + R_n)$. At some point, the heating produced by $I_n^2(t)R_n$ becomes sufficiently small to allow the restoring of superconducting state and the current value at which it happens is called *return current* I_r [41, 42]. Then the switch closes again and the current returns to I_b with a time constant $\tau_f = L_k/Z$ (see Fig. 1.9).
The same dynamics can be read in terms of output voltage pulse. As $R_n >> 50\Omega$, the

voltage pulse can be written as

$$V_{pulse} \sim (I_b - I_r) \times 50\Omega \times G \tag{1.25}$$

where G is the readout circuit eventual gain. The difference $(I_b - I_r)$ is the current hysteresis. The voltage pulse decays with time constant τ_f that corresponds to the detector recovery time. Hence we can conclude that the dead time is strongly related to the kinetic inductance. In order to reduce τ_f, one can follow two ways:

- reducing the wire length: this solution would reduce the inductance (see Eq. 1.19) but, at the same time, the sensitive area would reduce too, yielding to a loss in efficiency;
- connecting more nanowires in parallel as suggested in [43]: N nanowires in parallel will have a total inductance that is $L = (\sum_{i=1}^{N} 1/L_i)^{-1}$ reducing the final value[5];
- increasing the parallel impedance Z: this can also be done but some care is needed to avoid electric reflections and to maintain the automatic reset because a higher Z will leave more current in the SNSPD during signal pulse.

Timing jitter

One of the key features of SNSPD is the low timing jitter. This parameter represents the magnitude of statistical fluctuations of the time delay between detection event and pulse emission (see Fig. 1.10).

For a typical Gaussian distribution, the jitter can be quantified using the full width at half

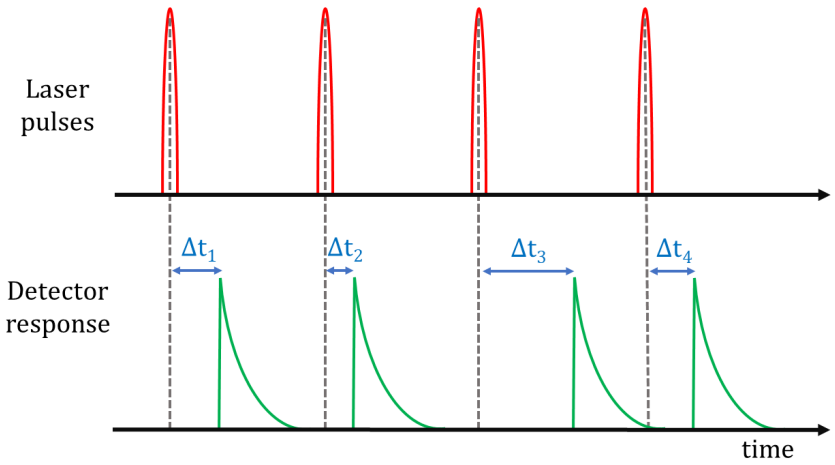

Figure 1.10: Time delay between photon emission and output pulse generation.

maximum (FWHM) of the distribution and the lowest measured value is 3 ps [18].

[5]See Chapter 2.

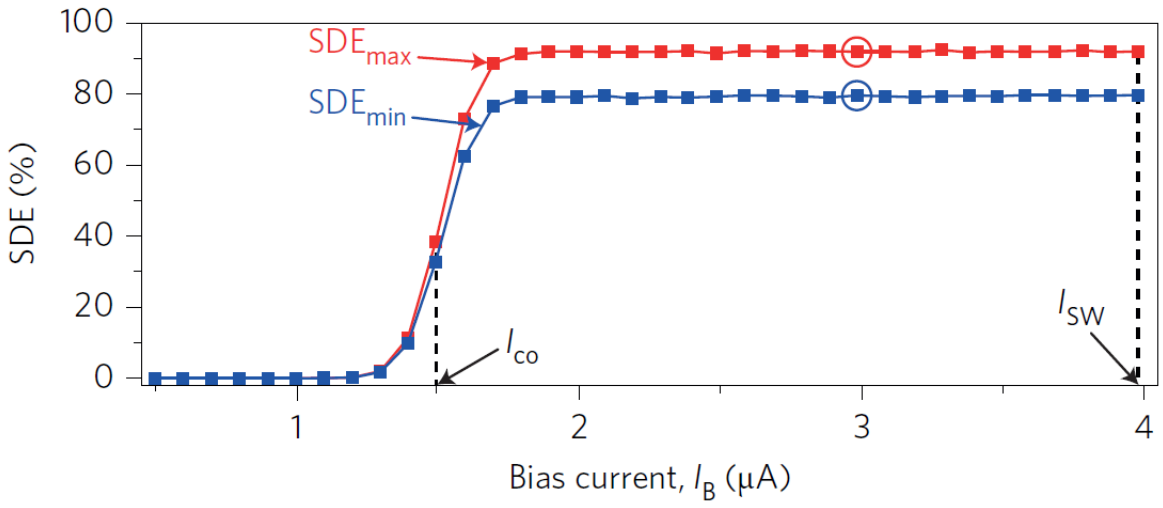

Figure 1.11: Highest system detection efficiency, measured of a WSi SNSPD [4]. The DCR is 10^{-1}cps.

Timing jitter is affected also by the measurement setup delay (setup jitter); once it has been isolated, it is possible to calculate the *intrinsic* timing jitter j_{intr}.
The origin of timing jitter is still unclear but it has been demonstrated in [44–46] that j_{intr} depends on the device area, on the bias current (and not on I_c), on the presence of inhomogeneities, and on signal to noise ratio (SNR). O'Connor et *al.* [47] indicate the hot spot size variation as possible mechanism for j_{intr}.

Detection efficiency

Reaching 100% system detection efficiency (SDE) in telecommunication wavelength is an important goal for SNSPD community, specially for quantum key distribution (QKD) applications. It has been demonstrated in [48] that, if the detector efficiency η is less than 50%, it is possible for a eavesdropper to hack the system without being caught. Also others applications (see next section) require high sensitivity and SNSPD satisfy that requirement. The highest detection efficiency value of 93% was measured by Marsili et. *al.* in [4] on a WSi SNSPD embedded in an optical stack designed to enhance absorption in the temperature interval between 120mK and 2K; the incident wavelength was around 1550 nm (see Fig.1.11). Another relevant result is [49] in which the authors realized a NbN SNSPD with $DE = 90\% - 92\%$ at $\lambda = 1550nm$ in a higher temperature region (1.8 K-2.1K).
The *quantum efficiency* η_Q is defined as the ratio between the number of detected photons and the number of incident photons and its value lays between 0 and 1. The quantum efficiency is often very low but the overall efficiency, called system detection efficiency, can be enhanced significantly with the use optical cavities [50]. The system detection efficiency

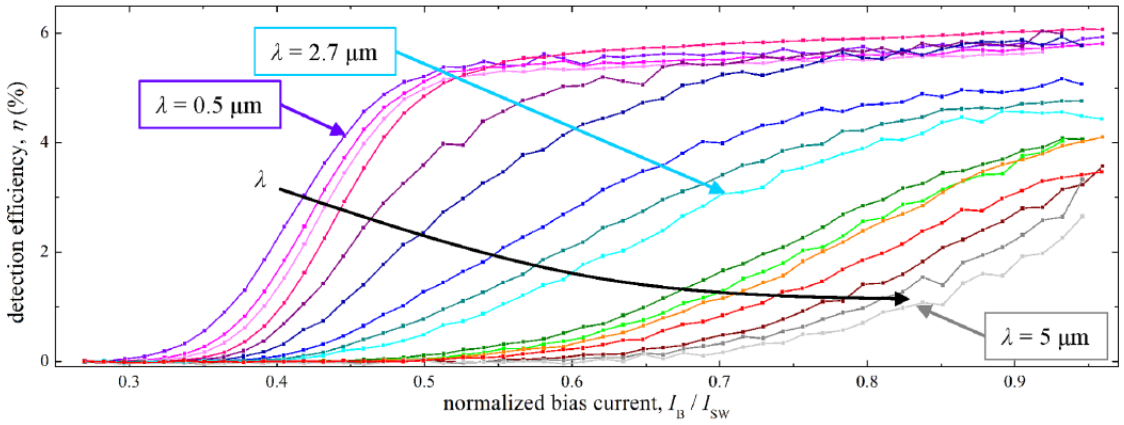

Figure 1.12: Detection efficiency of a 30nm wide parallel SNSPD realized with a 5.5 nm thick NbN film [5].

depends on the combination of three contributions:

$$\eta_{SDE} = \eta_Q \times \eta_{oc} \times \eta_{abs} \tag{1.26}$$

the first contribution η_Q depends on the material properties and on nanowire parameters; the second term takes into account the goodness of the cavity and of the optical coupling between the light source and the device; in the end, the third term of Eq. 1.26, is the absorption efficiency of the nanowire which also depends on both the material and the optical structure.
As shown in Fig.1.11, in the low bias current regime, SDE grows with current until it reaches a *plateau* around its maximum value. The bias current value is choose in order to work in the plateau region in order to avoid uncertainties in the count rate, arising from possible current fluctuations.

As one can see in Fig.1.12, with the use of SNSPD it is possible to detect single photons also at middle-infrared wavelength up to $\lambda = 5\mu m$ ([5]) even though the detection efficiency is lower in this case (about 5%). This result opens new perspectives in a broad range of applications.
In [51] authors also obtain a useful expression to estimate the detection efficiency at different wavelengths

$$\eta_{SDE}(\lambda) = \eta_{pl}(T)\frac{1}{(1+\lambda/\lambda_c)^n} \qquad \lambda_c \propto \left[\Delta\sqrt{\tau_{th}D_q}\left(1-\frac{I_b(T)}{I_c(T)}\right)^{-1}\right] \tag{1.27}$$

where $\eta_{pl}(T)$ is the efficiency value at the plateau (which depends on the temperature), n is an empirical parameter, Δ is the energy gap and D_q is quasi particles diffusion constant. In this expression λ_c is the cut-off wavelength and sets the lowest energy limit for detectable

photons.

Dark counts

Dark counts are pulses spontaneously emitted by the detector in absence of a light source. Dark counts are due mainly to two causes:

- background noise produced by spurious photons reaching the detector or by the room temperature black body radiation coupled to the device by the fiber;
- intrinsic dissipative processes occurring in the superconductor.

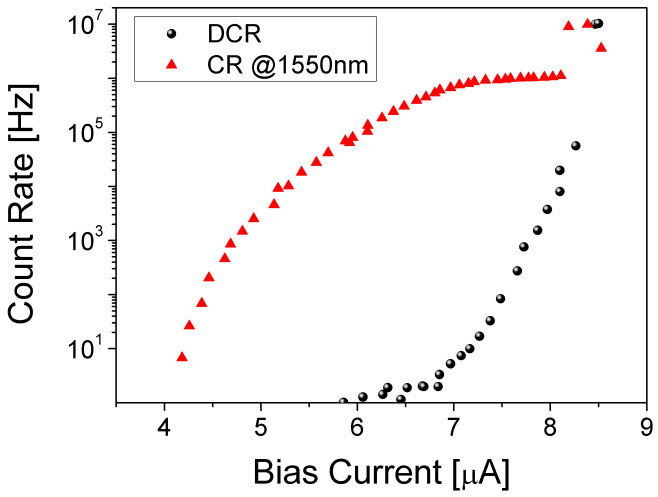

Figure 1.13: Measured Count rates of a $\emptyset = 15\mu m$ NbTiN SNSPD. Black spheres represent the Dark counts rate and red triangles the photon count rate at 1550nm. The device was realized at *State Key Laboratory of Functional Materials for Informatics, Shanghai Institute of Microsystem and Information Technology, Chinese Academy of Sciences*, Shanghai 200050, P. R. China

It was demonstrated in [52] that the noise due to the fiber can be reduced with the use of a on fiber band-pass filter. On the contrary, the mechanism through which a intrinsic dark pulse is generated is not fully understood and it is not yet possible to adjust the fabrication process with the aim of reducing dark counts, even though lot of efforts are being putted in this direction.
The most valued dark count models are related to the presence in type II superconductor of vortices with a normal core and to their dynamic [6]. Furthermore, Ejrnaes et *al.* [53] observed that the dark count generation mechanism might also change with the temperature.

Dark counts origin will be treated in details Chapter 3.
In all dark counts models, dark count rate (DCR) exponentially increases with the bias current (see Fig. 1.13) and decreases as the temperature is lowered.
In SNSPDs, the dark count rate can be pushed to very low values, namely less than 1 cps [21]. The lower the DCR is, the higher the signal to noise ratio (SNR) becomes; for this reason, they are considered good candidates for ultra low signals experiment, as dark matter detection [54].
In the operating conditions, the bias current is set to the lowest value in the count rate plateau region of Fig. 1.13 in order to maximize the count rate (and hence the efficiency) and minimize the dark count rate. This heed is taken to have the highest signal to noise ratio.

1.4 SNSPD Applications

Due to their high level specifications, especially to the high detection efficiency in the infrared wavelength and the low dark count rate, SNSPD appear very suitable for quantum information applications. Moreover, they can also be considered as a substitute of InGaAs [55] single photon detectors at telecommunication wavelengths.
In this section I briefly describe the main applications of SNSPDs.

Quantum Key Distribution (QKD)

Quantum cryptography, or quantum key distribution, is a method through which two parties can create a secure key distribution channel on the classical network [56]. This cryptography method is referred as *quantum* because the key used to decrypt the messages is generated and transmitted by using quantum properties of the light, as polarization and orbital angular momentum.
In principles, quantum cryptography protocols are inviolable but it has been demonstrated in [48] that, by taking advantage of the system losses and the low detector efficiency, it is possible to get the key without being caught. High detection efficiency in telecommunication wavelength region (1550nm) is hence required.
Up to now, QKD at 1550 nm with an SNSPD has been demonstrated over a range from 102km to 509km with a key rate from 10^5 cps to 10^{-3} cps [57–59].

Boson sampling and quantum computing

Boson sampling [60,61] is a quantum computation method with non interacting bosons, typically photons, implemented using a linear-optical network, in which n identical photons in m possible modes pass through a collection of simple optical elements (beam splitters and phase shifters), and are then measured to determine the number of photons in each mode. The input is the photons initial configuration and the output is the number of photons in each mode.

A boson computer can be simulated by a quantum computer but, on the other hand, it cannot perform every classical computation because of the intrinsic quantum nature of indistinguishable particles statistics. Hence, boson sampling can be used either to demonstrate the *quantum supremacy* either as a quantum computing technique.
The photonic implementation of the boson sampling requires reliable sources of single photons, as well as a linear interferometers and high efficiency single photon-counting detectors, such as SNSPDs, which perform the measurements at the output of the circuit.
In [62–64] the authors introduced the SNSPD in boson sampling experiments with the result of reduced losses and increased number of photons processed simultaneously (up to 20).

Bell's inequalities validation

The EPR paradox, rose the suspicion about the non completeness of quantum theory; indeed, the apparently extraluminal and non local correlation among the spins of two fermions in a singlet state could be explained by the hypothesis of the existence of hidden local variables. Under this hypothesis, the causality and Lorentz invariance are preserved.
Many experiments have been carried out to test the locality of quantum mechanics and to prove or deny the existence of hidden variables and a powerful tool was provided by Bell in 1964. With his theorem, he demonstrated that quantum mechanics is a non-local theory if there are no hidden variables.
An experimental verification of quantum mechanics non-locality can be performed by using the Bell's inequalities [65]. These inequalities provide a practical tool to verify Bell's theorem. Many experiments have been carried out and the first was realized with photon polarization in 1981 [66].
The reason why the Bell theorem is still an open issue, is that all the experiments suffer of two *loopholes* which generate doubts about the likelihood of the results: the locality and the detection accuracy. In order to guarantee the locality of each measurement, the distance between the observers should be larger than the space covered by light within the measurement time. In order to avoid errors due to imprecise detection efficiency, Bell's inequalities tests with photons require 83% efficiency when the DCR is 1%[6].
Given the low DCR and the high detection efficiency, SNSPDs are good candidates to be used in Bell's inequalities experiments. In [67], the authors used a SNSPD to realize a loopholes-free Bell's inequalities test and with the tested system they could realize a pure and quantum random numbers generator.

Space to ground communication

Today the space to Earth communication is entrusted to radio frequencies signals but the use of optical signals can improve the data rates of hundred times. This is becoming an important issue as Mars and spatial mission are pushing forward great technology innovations. The problem in using optical signals lays in the requirement of large area telescopes coupled with

[6]The minimum efficiency is DCR dependent.

high efficiency detectors in telecommunication wavelength.
A proof of principle demonstration has been carried by Shaw et al. [68] with the use of a WSi SNSPD.In this paper they measured the data transmission rate of 45Mbps.

Dark matter detection

A variety of astrophysical observation, such as the galaxies rotation velocity, gravitational lensing effects and cosmic microwave background anomalies cannot be explained by simply applying general relativity equations. The approaches used to account for these experimental observations are two: one is to introduce a modified gravitational theory [69] and the other is to suggest the existence of and dark matter [70].
In the second hypothesis, 90% of the Universe mass is due to weakly interacting matter called *dark matter* (DM) which interacts with the gravitational field but not with the electromagnetic field. Several experiments have been setted up in order to detect DM but they could just set an upper limit to the mass (and energy) of these particles.
Hocheberg et al. [54] suggest that, trough the use od SNSPD, it can be possible to explore lower energy regimes due to the low energy gap and low dark count rate provided by the device. They measured a DCR of 10^{-5} cps and a 800 meV of energy threshold on a WSi nanowire at 300mK; in this conditions it would be possible to detect sub-GeV DM.

Lidar

Light Imaging Detection And Ranging (LIDAR) is a technique used to rebuilt the spatial distribution of a distant target by collecting the backscattered signals generated by the object when invested by a laser beam. This technique is widely used to measure a variety of different quantities such as oceans and forests profiles, wind speed, water vapour and aerosols content in the atmosphere, atmospheric temperature profile and so on.
The use of infrared wavelengths in Lidar may opens the way to the investigation of other pollutants content in the atmosphere. Indeed, in [71] it was demonstrated that by using a Lidar operating at 1570nm, it is possible to determine the CO_2 concentration. As claimed in [72], it would be possible, with far infrared Lidar, to study the presence of others molecules in the atmosphere but it can be possible only with low noise detectors able to cover a broadband wavelength range, as SNSPD.
The combination of SNSPD and Lidar technologies has already been used to measure the sea fog [73], the wind speed [74] and aerosol polarization ratio [13]. Lidar technique will be widely described in Chap.4 and, in Chap. 5, the experimental results of a Lidar measurement with SNSPD at λ=1064nm are presented in details.

Summary

In this Chapter we described the main properties of Superconducting Nanowire Singe Photon Detectors; we first gave a short introduction to superconductivity, focusing on the physical

parameters useful for the SNSPDs and then we concentrated on the detector characteristics. We also provided a brief list of the applications of SNSPD. Due to their high level performances, they are very promising and through a deeper understanding of the working principles their specifications can probably be further improved.

CHAPTER 2

SNSPD - Fabrication and Measurement Setup

Abstract: As largely illustrated in the previous chapter, SNSPDs are advanced detectors with very promising characteristics. They are realized by using a very thin (few nanometres) superconducting film deposited on a substrate. In order to increase the effective detection area and the sensitivity, the film is given a meander geometry that is a long and narrow nanowire (approximate width 100nm) bent to form a square or a circle and embedded in a optical cavity.
The ideal detector should have 100% detection efficiency, short time response and a large amplitude output signal. The last requirement translates in high critical current density ($j_c \propto T_c^2$) and low retrapping current (see eq. 1.25). The retrapping current can be reduced with the choice of a thin film with high resistivity close to the critical temperature ($I_r \propto 1/\sqrt{\rho_n(T = T_c)}$). A high normal resistivity $\rho_n(T \sim T_c)$ can also enhance the fraction of I_b diverted in the load resistance after the detection event, reducing the intrinsic recovery time.
As explained in the previous chapter, the fall and recovery times depend on the kinetic inductance which increases with the square of the penetration depth. So that, a superconducting material with a small magnetic penetration depth and a high normal resistivity will contribute to reduce the total response time.
Another important property of the material used to realize the SNSPD is the coherence length ξ. The current assisted hot spot formation is enhanced in very thin films but the lowest thickness cannot be smaller than the coherence length, otherwise the superconducting state would be compromised.
As also mentioned before, the small coupling time τ_0 will reduce the electron-phonon interaction time τ_{ep} which sets the intrinsic limit to detector response time.
The choice of material, geometry, fabrication technique affects the detector performances and in this chapter we will describe the techniques used to fabricate the SNSPDs with a focus on different geometries and materials.

SNSPDs are measured in cryogenic environment that can be a liquid helium container (dewar) as well as a closed cycle cryostat. Hence, the coupling with an external light signal is not straightforward and in this chapter we will also describe our measurement setup and optical coupling methods.

2.1 Fabrication

During this work of thesis four materials have been studied: NbN, NbTiN, NbRe, MoSi. The intrinsic characteristics that the SNSPD should have are high critical temperature T_c, small penetration depth λ and coherence length ξ_0, short coupling time τ_0, high normal resistivity $\rho_n(T_C)$ and critical current density j_c. The listed materials all satisfy these requirements but also the fabrication process must be adjusted for the specific superconductor. During this PhD I worked at the optimization of the fabrication process of NbN, MoSi and NbRe micro-strips, nanowires, meanders and parallel nanowires. In this section, the fabrication process of NbN is presented. The steps followed for the fabrication of MoSi and NbRe are the same as NbN when not specified and some details will be provided in Sec. 2.4.

Thin film deposition

The first step in the fabrication of an SNSPD is the deposition of a thin film of superconducting material on a substrate. The choice of the substrate may also affect the characteristics of the detector [75] and we choose $SiO_x/Si(100)$ because it is more versatile than others.

To realize the thin films, we used DC magnetron sputtering deposition technique (See Fig.

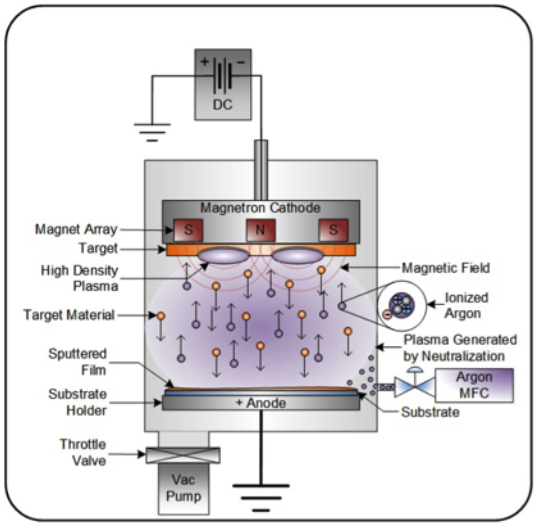

Figure 2.1: Magnetron sputtering sketch. Ar^+ ions are accelerated towards the target and the atoms are detached from the material and can reach the substrate.

2.1). The process is carried on in a high vacuum chamber ($P_B = 5 \times 10^{-9}$ torr) which contains the substrate and the superconductor material target. Ar gas is injected in the chamber ($P_{Ar} = 10^{-3}$ Torr) and, as a consequence of natural cosmic rays radiation, some Ar^+ atoms are ionized. When high voltage is applied, Ar-ions plasma is accelerated towards the target and materials atoms and electrons are free. The free electrons further ionize the gas and this process is enhanced with the use of a magnetic ring (magnetron sputtering).

When the ionization rate is sufficiently high, the plasma becomes stable and the deposition process starts. The sputtering time duration t_d sets the film thickness according with the expression $d = r \times t_d$ where r represents the deposition rate.
For NbN deposition we use a Nb target and inject N_2 gas in the vacuum chamber; NbN deposition rate is $r = 0.75nm/s$ and we setted the deposition time as the shortest possible in order to achieve the minimum thickness. In order to do that, the substrate never stops under the target and the reached thickness is about 6nm. The substrate is a ultraflat oxidized silicon wafer with $\oslash = 3''$ and the NbN film thickness is uniform within a distance of 1cm from the border.

Photolithography and RIE (reactive ion etching)

Before the realization of a meandered nanowire, it may be preferable to remove with photolithography technique the superconducting film that will not be used. In order to do that,

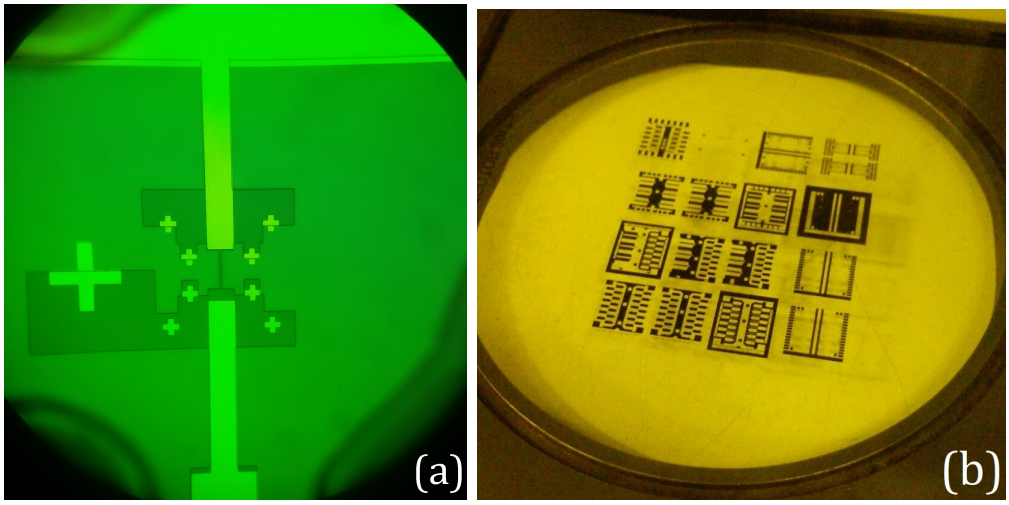

Figure 2.2: (a)Negative photoresist mask aligned on patterned superconductor.(b) Chromium master mask for the photo lithography steps in the SNSPD fabrication process.

the *photoresist* AZ1514H is spinned on the film at 3000rpm and baked at the temperature of 88°C for 15 minutes. At this point, the pattern impressed with chromium on glass mask (Fig.2.2[b]) can be transferred to the photoresist trough the use of a mask aligner. The exposition time is 15s. The UV light in the mask aligner modifies the molecular structure

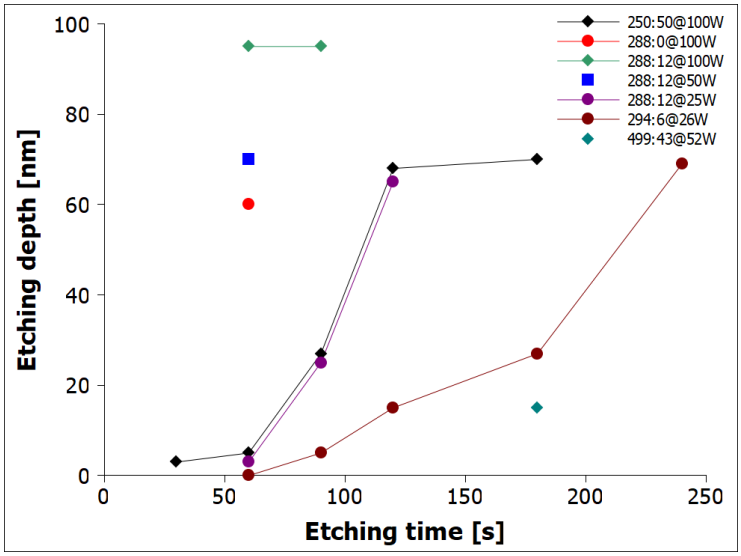

Figure 2.3: RIE etching depths as a function of the etching time. Different concentrations of $CF_4 : O_2$ at different powers are shown.

of the photoresist in the areas where it is not covered by the chromium mask. After soaking the film 30sec in AZ351b developer (diluted in a ratio 1:4 with distilled water) and 30sec in distilled water, just the photoresist covered by the mask remains.
After that, the reactive ion etching process (RIE) removes the superconductor where it is not covered by the photoresist and the mask geometry (microns size) can be impressed on the superconductor.
In the case of NbN, the RIE etching depths are presented in Fig.2.3 as a function of the etching time, for different powers and relative concentrations of CF_4 and O_2 gases.
With a photolithographic process it is possible to realize down to 500nm narrow strips (see Fig.2.2[a]). Below this resolution electron beam lithography is required.

Electron beam lithography

Trough electron beam lithography (EBL), it is possible to realize down to 20nm narrow strips with uniform edges. For this step PMMA (polymethyl methacrylate) is spinned on the device. This resist is spinned at 2000 rpm and baked afterwards at 170° C for 15 minutes. The spinning speed and concentration ensures a layer thickness of approximately 70 nm.
The EBL technique consists of scanning an electron beam across a surface covered with the PMMA that is sensitive to those energetic electrons. Thus, electrons deposit energy in the PMMA as the beam moves in the desired pattern. The exposed PMMA is removed with the developer, and reactive ion etching technique is use again to transfer the pattern to the superconductor. The remaining resist can be removed by a solvent. A simple scheme of the photolithography and EBL process in given in Fig.2.4.

With EBL technique, we were able to realize NbN meanders with 92nm wide strips (see

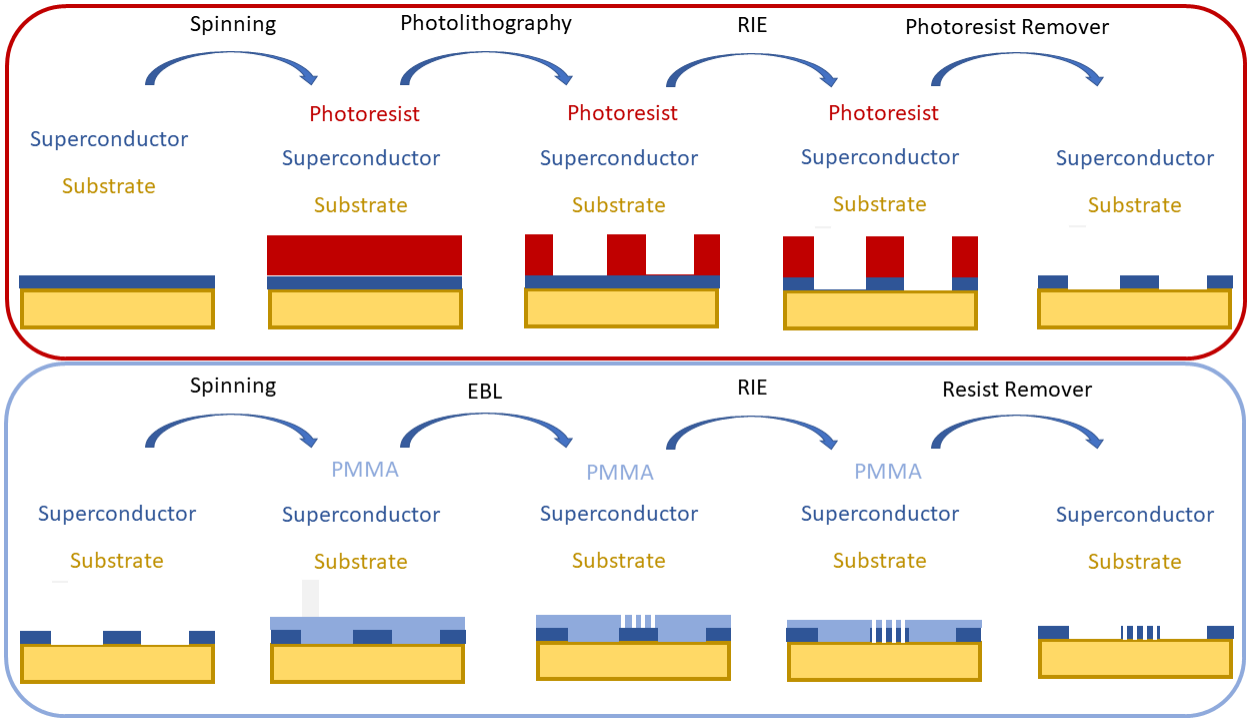

Figure 2.4: Photolithography (red box) and EBL (blue box) fabrication processes.

Fig.2.5).

Contact pads deposition

The last step is the contact pads deposition. The material used is typically a bilayer of Ti and Au for a total thickness of about 30nm but we also fabricated devices with Al contact pads; indeed, in our case Al and Nb targets are located in the same vacuum chamber and they can be deposited together, without breaking the vacuum, resulting in a very clean interface.
The contact pads are deposited with the use of lift-off lithographic technique. Before the Al (or Ti/Au) deposition, the negative photoresist AZ5214E is spinned for 1min at 4000rpm on the substrate and backed at 88^oC for 15min.
With the use of a mask aligner, the reversed contacts pattern is impressed on the photoresist with an exposition time under UV lamp of 4sec and a reverse backing of 3min at 120^oC on a hot plate. Then, sample is exposed again under UV lamp for 20sec (without mask) and soaked 30sec in the AZ351b developer (1:4 with H_2O) and 30sec in distilled water.
After that, Al (or Ti/Au) and, eventually, NbN are deposited on the contact pads mask. In the end, the sample is soaked in AZ-remover or acetone which remove the exceeding photoresist. As a result, the photoresist, covered by the metal and the superconductor,

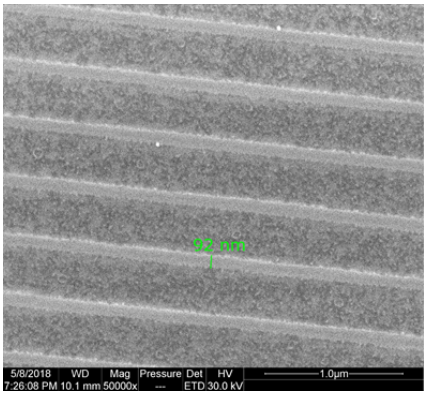

Figure 2.5: NbN strips in of a square meander SNSPD realized with EBL technique. The width is 92nm.

remains just in th contact pads sites. After contact pads deposition, the photolithography process can be repeated in order to adjust the shape of the superconductor. The SC mask can be aligned to the pattern with the use of markers (crosses) and a mask aligner. Some realized samples are shown in Fig.2.6.

2.2 Geometries: Large areas and parallel configuration

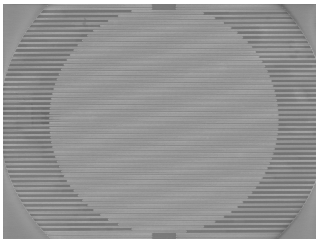

Figure 2.7: Round SNSPD. Picture on behalf of SIMIT, Chinese Academy of Sciences (CAS), Shanghai, China.

The choice of SNSPD geometry depends on the application. The most commonly used is a circle meander with a diameter that fits with the optical fiber core size as the one shown in Fig.2.7. Depending on the application, also larger areas can be required. In the case of Lidar, the beam to be coupled with the detector has a diameter of approximately 1cm and multimode fiber with larger core are preferred as well as a larger area device.

The simplest way to increase the area would be to fabricate a larger meander with a longer nanowire. Anyway, that solution would increase the kinetic inductance (Eq. 1.19) affecting the SNSPD dead time and maximum count rate.

In [76], the authors fabricated a $40\mu m \times 40\mu m$ meander and improved the count rate though the use of parallel nanowires. Recently, with the same technique, a round SNSPD with $\oslash = 300\mu$m was realized [77]. This configuration, first presented in [43], consists of N parallel nanowires arranged in a series of n_B blocks having n_S parallel strips ($N = n_B \times n_P$), as sketched in Fig.2.8. In the operating regime, the detector is biased close to the critical current that is $I_C = n_S \times I_{CS}$, where I_{CS} is the critical current of a single strip. When the photon absorption leads one strip into the normal state, the current is

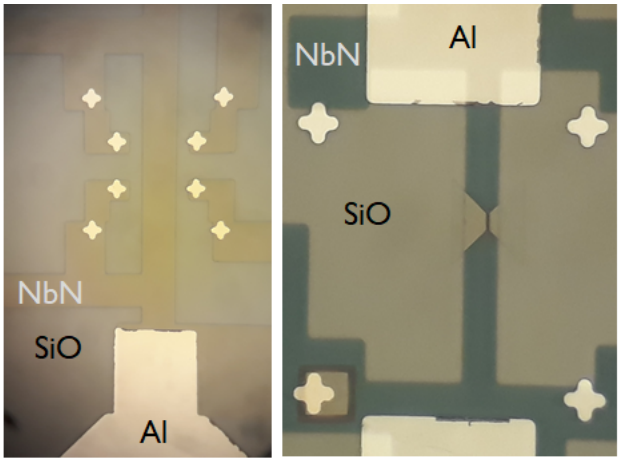

Figure 2.6: NbN micro and nano strips on Al contact pads and SiO substrate realized with lift-off technique.

diverted in the other strips of the same block; at this point, the current in the block's strips overcomes the critical value and all the block switches to the resistive state, the current flows in the load Z and a voltage pulse is observed.
The advantages in using the parallel configuration are the following:

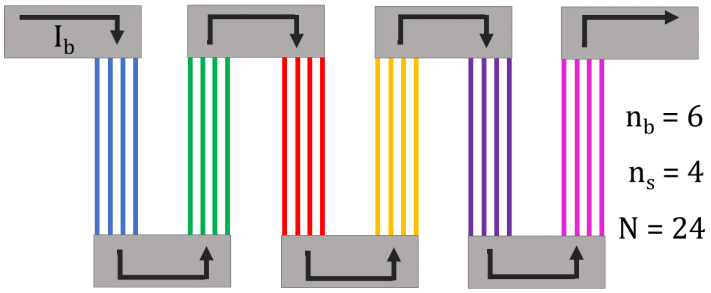

Figure 2.8: Sketch of parallel meander configuration.

- *Larger signal amplitudes.* The critical current of the device is higher than the single line meander one according with the equation $I_C = n_S \times I_{CS}$. Hence the pulse amplitude, given by Eq.1.25, is enhanced.
- *Smaller recovery time.* Thanks to the parallel configuration, the new kinetic inductance (L_P) will be smaller than the single line meander one (L_M) according with the relation

$L_P = L_M/n_s^2$. Consequently, the fall time becomes $\tau_{fP} = \tau_{fM}/n_S^2$ (Sec.2.4).

- *Increase in maximum count rate.* The shorter recovery time leads to higher maximum count rate as the two quantities are inversely proportional.

- *large detection area.* The detection area can be increased by adding other parallel strips and other blocks. Anyway, in doing it, a special care has to be taken to avoid the latching phenomenon [78].

About the rise time, it is not possible to say *a priori* whether it will be smaller in the case of parallel strips. Indeed, we can write

$$\frac{\tau_{rP}}{\tau_{rM}} = \frac{L_P}{Z + R_{nP}} \cdot \frac{Z + R_{nM}}{L_M} = \frac{1}{n_S^2} \cdot \frac{Z + R_{nP}}{Z + R_{nM}} \tag{2.1}$$

in which we see clearly a dependence on the normal resistance.

2.3 Measurement Setup

Measurement Setup and Readout Circuit

An SNSPD can be cooled down by putting the cryogenic insert in liquid helium dewar directly if the critical temperature is higher than 4,2K. In the case of a Lidar measurement, 90% efficiency is not mandatory because the signal is expected to be very intense and additional attenuation may also be needed. Hence, it is not required to reach a temperature in the regime of mK.
The detector can also be cooled, eventually, with another measurement setup which, through the use of a pump, can reach the temperature of 1K.
The measurement setup is sketched in Fig.2.9. The SNSPD is cooled down in liquid helium dewar and the bias current is controlled by a DC generator. The current is supplied by a 5V battery connected to a variable resistor ($0 - 100k\Omega$) and the value is kept stable by multiple stages of filters and it is injected in the DC plug-in of a bias tee. A coaxial cable leads the bias current into the device, often shunted with a 50Ω resistor (fixed on the cryogenic insert head, nearby the detector). The SNSPD, eventually, generates a voltage pulse that also travels on the coaxial cable and is separated from the DC component by the bias tee. The RF signal is hence amplified by a factor 400. The pulses (RF signal) are read on an oscilloscope and analysed with the acquisition programs. We use a ground decoupler to avoid loops.
Part of my work was also dedicated to the realization of a transportable electronic setup measurement. In order to do that I learnt how to program a digital to analog converter (DAC) and wrote the programs to control the bias current from laptop. I also realized the program to count the pulses which collects the signal from the oscilloscope and distinguishes, by means of a hysteretic trigger, the pulses from the noise. On the new electronic I carried

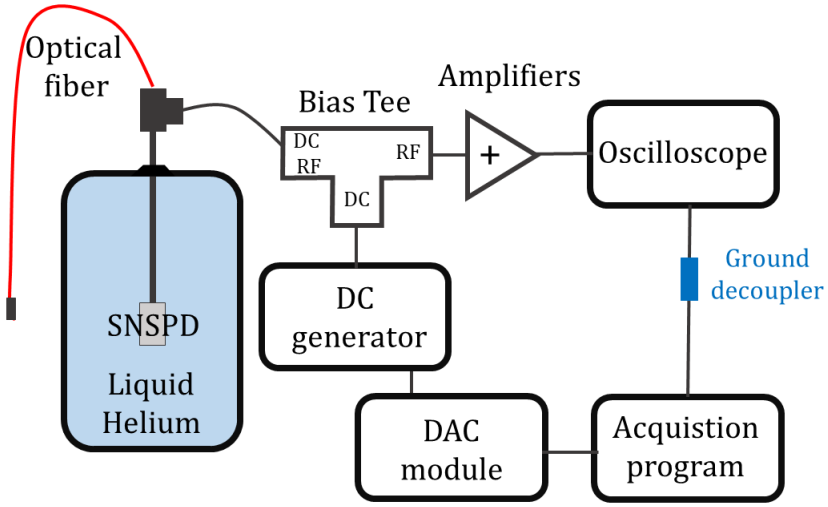

Figure 2.9: Measurement setup.

out a noise spectral analysis and then realized the filters in order to reduce it.

In order to have a more portable measurement setup, I also realized a small bias box (10cm×2cm×6cm) powered with common power banks, to ensure a low noise and stable current from 0μA to 50 μA with an error of 3nA (see Fig. 2.10). The box can generate two different and independent bias current values, and the voltage gain can be set to 1 or 1000[1]. Several stages of filters are used in order to keep the bias current value very stable.
The advantage in the use of this bias box is that the DC generator and the DAC module in Fig.2.9 are not necessary. Moreover, it is powered by a common power bank which make it extremely adaptable to all measurement conditions.

Optical coupling

SNSPDs can detect photons with nearly 100% efficiency [4, 49] but a special care has to be taken when the experimental system is optically coupled with the SNSPD; indeed losses can occur in the optical coupling with the cumulative effect of a reduction of system efficiency. We developed two methods to couple the light with detectors. The first method is to use a liquid helium continuous flux cryostat with a optical window and we mainly use this system for the simultaneous characterization of many SNSPDs at T=4,2K (Fig.2.11). The second method, specially created for the Lidar measurement with an SNSPD, involves the use of optical fiber and it has the advantage of being easily transportable and adaptable to other measurement setups.

[1]The gain G=1000 is suitable when a 50Ω resistor is placed in parallel to the SNSPD.

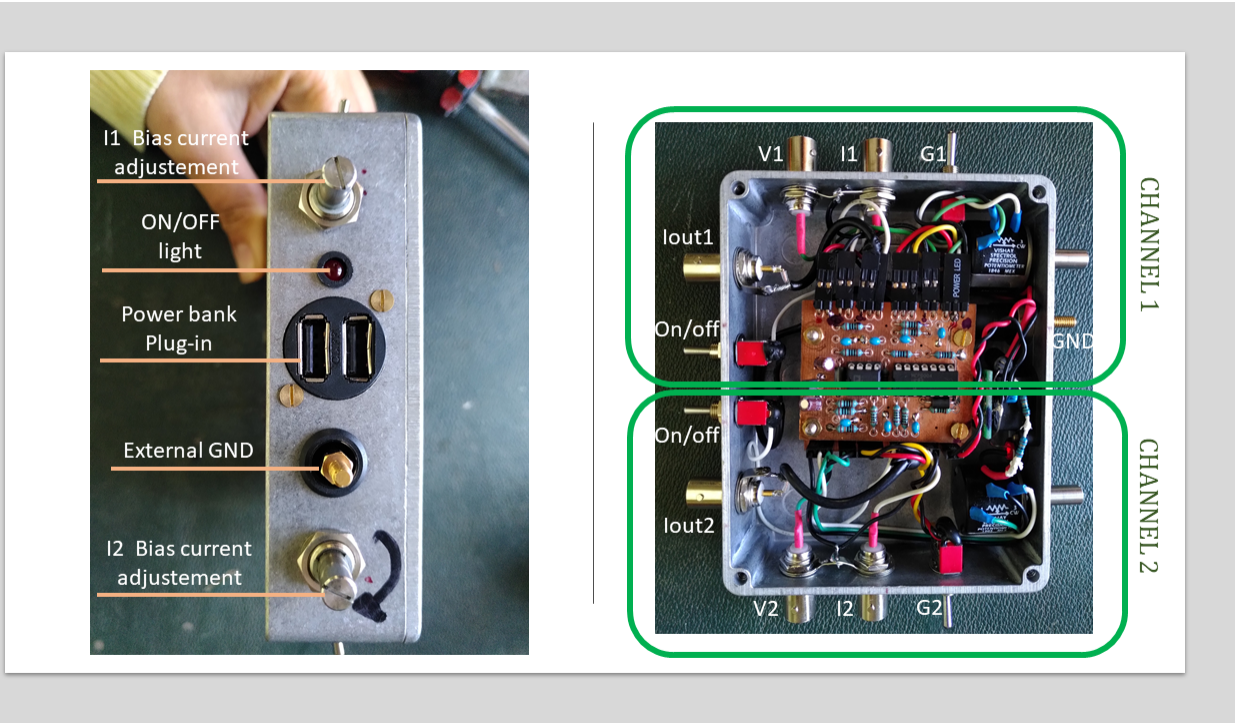

Figure 2.10: Bias Box details. I1. I2, V1, V2 can be connected to a oscilloscope to measure the current and voltage. Iout1 and Iout2 are the bias currents applied to SNSPD1 and SNSPD2. The voltage gain (G1 and G2) can be set to 1 or 1000.

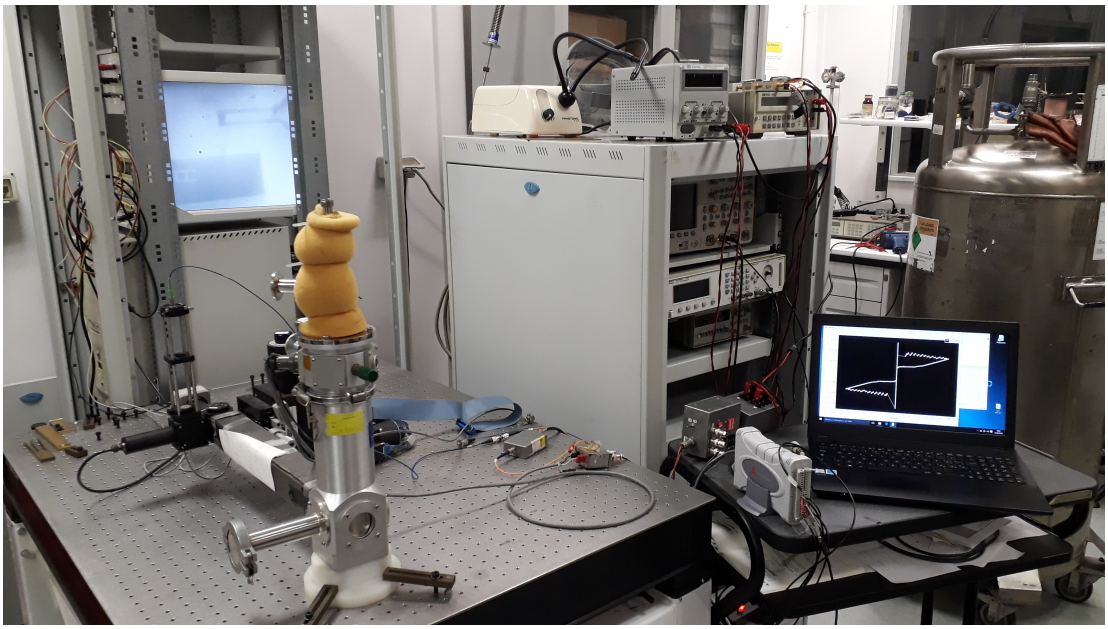

Figure 2.11: SNSPD lighting by optical window. The laser (blue fiber) is attenuated and diverted in a black corridor that shields the cryostat optical window from the background. By using a camera it is possible to align the laser with the device and measure the optical response.

In Fig.2.12 I show the details of the cryogenic insert used to measure optical fiber coupled SNSPD. I designed and assembled this setup in order to test simultaneously the devices on two different chips with the possibility of using two wavelengths. This was done in the perspective of a comparison between lidar measurements with SNSPD at different IR wavelengths.

The upper flange in Fig.2.12 has two vacuum sealed FC/PC connectors with 400-2200 nm wavelengths multimode fibers which runs along the tube in two separated straws, and the insert is equipped with two coaxial cables and two stages of filters. The two fibers can be connected to the SNSPD or removed if not needed. The cryogenic insert head can easily be changed to fit with device's packaging.

On the SNSPD we fix a fiber which can be either single or multi mode, according with the application and with the detector size. The fiber has a FC/PC connector on one side to be fixed on the cryogenic insert and a bare zircon ferrule on the other; the latter is aligned with the detector by mean of a XYZ micro-handler and a IR camera. In details, a metallic support holds the device and it is perforated in order to check the alignment with a camera placed below. The ferrule is held by another metallic support connected to XYZ micro-handlers and the other side of the fiber receives a continuum laser signal (see Fig.2.13). After the alignment, the ferrule is fixed to the SNSPD with a UV cure epoxy. A mechanical support

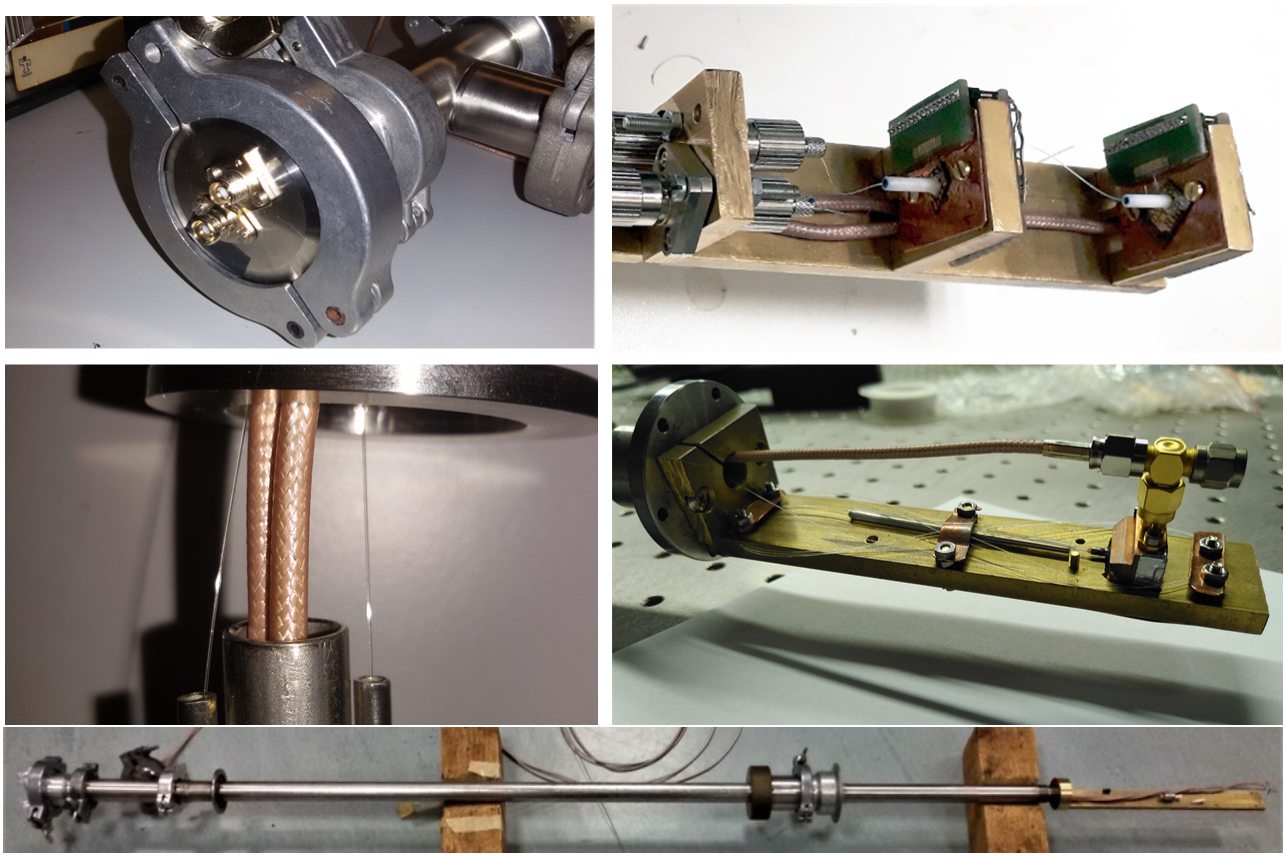

Figure 2.12: Cryogenic insert used for the measurements of SNSPD photo-response.

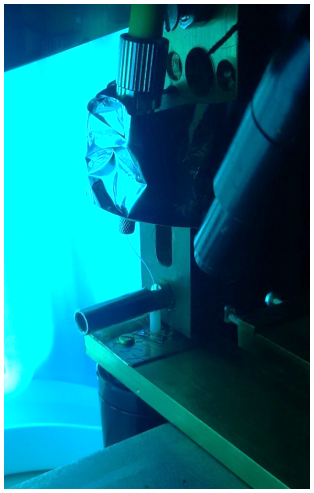

Figure 2.13: Fiber epoxy fixing to the SNSPD with UV light.

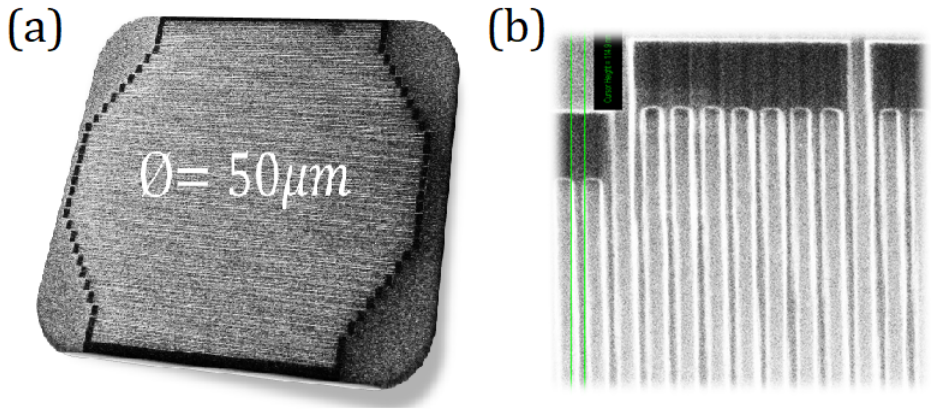

Figure 2.14: (a) SEM picture of a $\oslash = 50\mu m$ diameter NbN SNSPD realized with parallel nanowires. (b) Detail of four parallel nanowires of width w=100nm.

on the insert head prevents any eventual detachment of the ferrule.

2.4 Experimental results

Even if it has been demonstrated that the same SNSPD can be used to detect a broadband range of photons [5], the choice of materials can be crucial in the optimization of a specific property. Some materials are more suitable for infrared photons, some can provide faster device and some others can lower the dark counts and it has not yet been found the material that can be appointed as the best, regardless the application.
Furthermore, some properties as dead time and active area, can be tuned with the opportune choice of the geometry as mentioned before.
In this section I present the results of the fabrication of parallel NbN nanowires and a study of four different materials SNSPD with a focus on the new features that cannot yet be found in literature.

NbN parallel meander

A consistent part of this work of thesis was devoted to the demonstration of a Lidar measurement with SNSPD detector and a transportable electronic setup. One of the possible ways of coupling the Lidar signal with the SNSPD is to use a optical fiber (both multimode and single mode).
In order to couple the SNSPD with the Lidar, I designed and fabricated a 6nm thick NbN larger area detector with $50\mu m$ core multimode fiber. Niobium Nitride is the most commonly used material for SNSPDs. It is a Type II superconductor which exhibits many practical advantages: the bulk critical temperature is $T_C \sim 16$ K and it permits measurement in liquid

helium, the coherence length is $\xi \sim 3-5$ nm, the critical current density j_C is high and the electric response is fast.

The thin film was deposited with magnetron sputtering and the nano-patterning and the

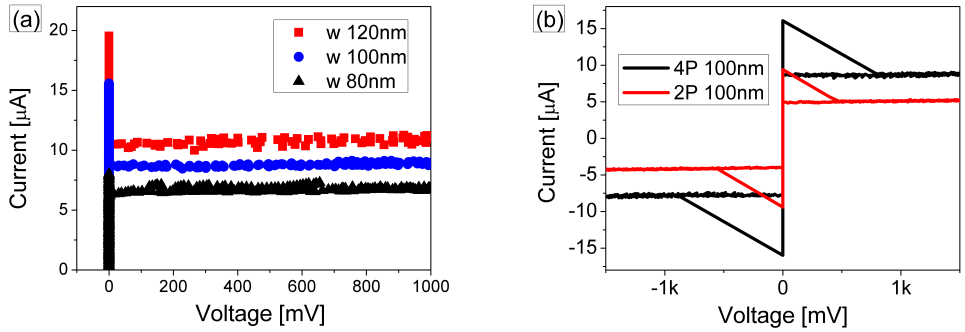

Figure 2.15: IV curves for different round NbN SNSPDs ($\oslash = 50\mu m$). (a) Meander with $n_S = 4$ parallel strips of different widths (80-100-120 nm). (b) 100 nm width meanders with $n_S = 2$ and $n_S = 4$ parallel strips.

contact pads deposition were realized by the Institute of Photonics and Nanotechnologies in Rome (IFN, National Research Council CNR). We fabricated three different width meanders with 2 and 4 parallel nanowires (Fig.2.14).

In Fig.2.15 we see that the critical and return currents scale with the number of parallel nanowires and with their widths; for w=120nm, we measured current hysteresis up to $18\mu A$ (4 parallel nanowires).

We measured that the signal pulse fall time of 120nm wide SNSPD (4 parallel lines) is $20ns$ (see Fig.2.16) corresponding to a count rate upper limit at 1550nm of 40MHz.

We could not estimate the efficiency as laser light power was too close to the powermeter

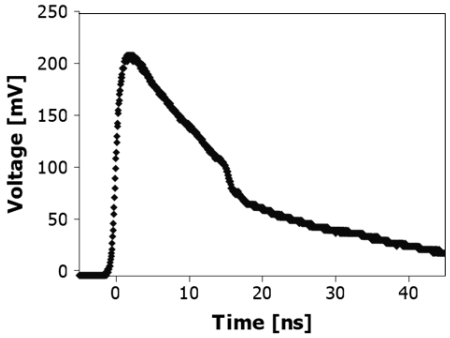

Figure 2.16: Voltage pulse amplitude of a NbN SNSPD realized with four parallel nanowires (w=120 nm).

lower limit; moreover, the optical coupling was not optimized and the losses were very high. From the results obtained in the characterization measurements, we can claim that these devices are good candidates for a Lidar measurement in the IR wavelength region after the optimization of light coupling.

MoSi/Al

The use of NbN and NbTiN has some limits when a detector for infrared wavelengths applications is required ($\lambda > 1.5\mu m$). This is because the energy gap Δ of these superconductors is relatively high and, as shown in Eq.1.21, it affects the minimum detectable photon energy. For the use of SNSPD in infrared applications, other materials, as amorphous Molybdenum silicide (MoSi), have been suggested [79] as they have lower energy gap and should thus move the detection limits to longer wavelengths.

In order to couple the SNSPD detectors to Lidar systems in the IR, we fabricated[2] a 10nm

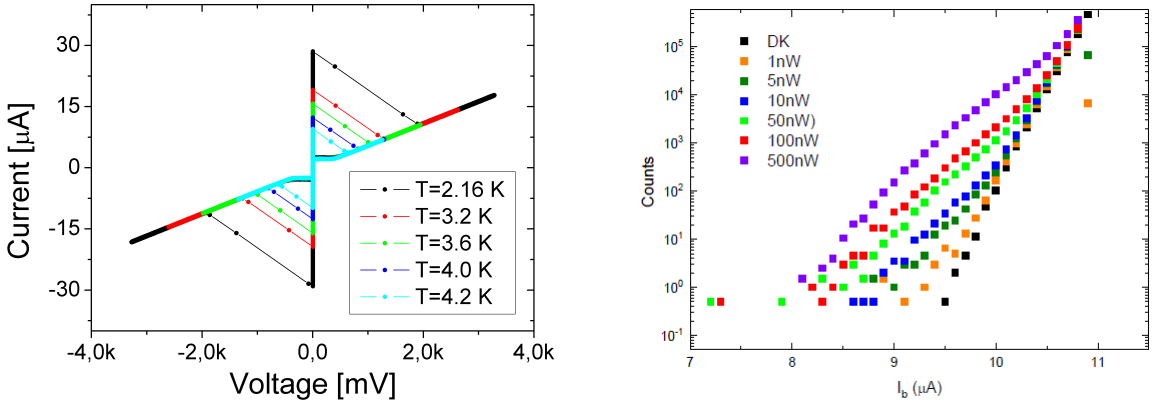

Figure 2.17: MoSi IV curves at different temperatures and count rates with variable 1550nm laser power at 3,3K.

thick and 120nm wide square MoSi meander ($5\mu m \times 5\mu m$). We also added 2nm Al layer to prevent the oxidation of the thin film and this step considerably enhanced the device properties. A picture of the sample is presented in Fig.2.18.

The thin film of MoSi was deposited with sputtering technique in a vacuum chamber ($P_B = 1.8 \times 10^{-7}$ torr) at a deposition rate $r = 23pm/s$ with $P_{Ar} = 1.5 \times 10^{-}3$ torr and a sputtering power of 50W. The Al thin layer is deposited in the same chamber, without breaking the vacuum, with a sputtering power of 20W at the same deposition rate. The meander were realized with EBL technique with doses 1520-1550-1580 $\mu C/cm^2$ on a PMMA

[2]In collaboration with the Institute of Photonics and Nanotechnologies (INF, National Research Council CNR), Rome, Italy.

resist (6% in distilled water) spinned for 60sec at 4000rpm and baked 5min at 170^oC. Au/Ti contact pads were deposited though lift-off and evaporation.

In Fig.2.17 we show the IV curves of MoSi/Al SNSPDs and one can clearly see that the current hysteresis amplitude, a clear indicator of the presence of thermal instability of a normal domain, is acceptable also at 4,2K; for MoSi devices, we could measure the hysteresis just at lower temperatures.

We measured the device optical response at T=3,3K and we observed a saturation of the

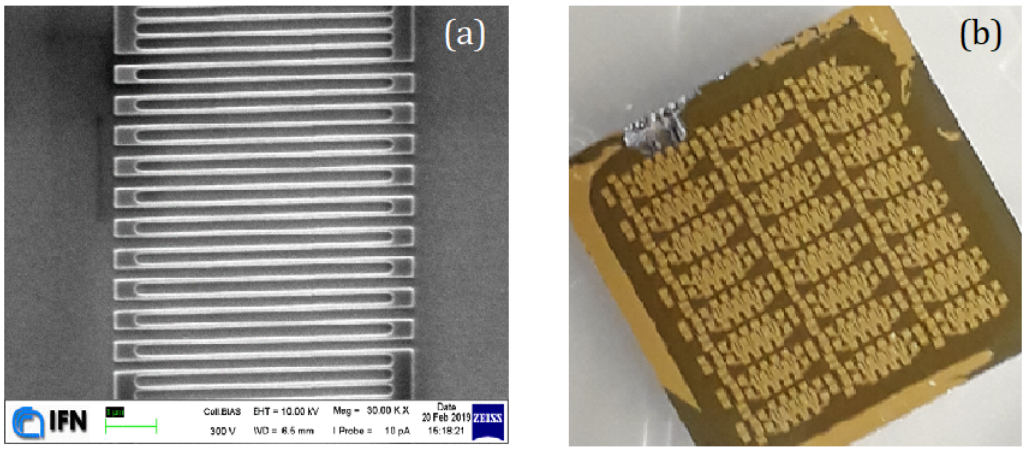

Figure 2.18: Molybdenum Silicide chip (b) containing SNSPDs(a) and nano-stripes with Ti/Au contact pads.

count rate at 650nm and demonstrated the single photon detection regime at 1550nm. The dead time is 5ns and the pulse amplitude after 52dB amplification is 45mV.

NbRe

Amorphous materials as MoSi present high detection efficiency in infrared wavelength domain at temperatures in the region below 2K ([4]) with the disadvantage that complicated and expensive refrigerators are needed.

In order to reach high detection efficiency in the infrared domain at higher cryogenic temperatures, $Nb_{0.18}Re_{0.82}$ is being studied. This material has a bulk critical temperature $T_c \sim 9K$ [80] and also for thin films it remains bigger than $4,2K$ [81]. $Nb_{0.18}Re_{0.82}$ can be a good candidate for IR photons detection because it has, similarly to NbN, high critical current density and short coherence length (3-4nm [82]) but, compared to NbN, it has a lower energy gap. In [82] the authors estimated the values of $\Delta(0)$ to be $\Delta(0)_{NbN} = 2,73$ meV and $\Delta(0)_{NbRe} = 1,03$ meV.

To further investigate the use of this new material as SNSPD, we realized NbRe strips[3] with different widths and measured the current-voltage characteristics (see Fig.2.20). The strip length is 400 μm and the thickness is 5nm; the different widths are 4 μm, 2 μm, 400 nm (see Fig.2.19).

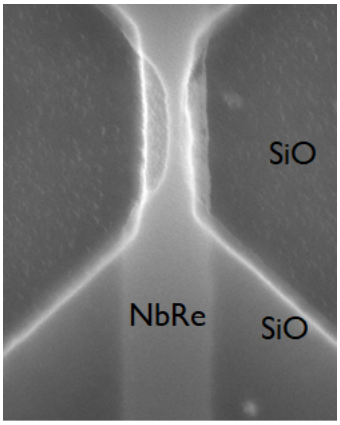

Figure 2.19: 400nm wide NbRe nano-strip realized with EBL on SiO substrate.

We realized the micro-strips by lift off and the procedure is the following:

1. AZ5214E photoresist is spinned for 1min at 4000rpm
2. the sample is baked at 88^oC for 15min
3. UV light is applied to the sample covered by inverted mask for 4sec
4. reverse backing at T=120^oC for 3min is performed
5. the sample is exposed to UV light within 20sec
6. the sample is soaked in AZ351B developer and H_2O (1:4) 30 sec and in H_2O for 30 sec.

Details about the thin film deposition can be found in [82].
The 400nm wide strips were realized with the use of EBL, with a dose factor of $200\mu C/cm^2$. The initial settings are 30kV voltage and 69pA Faraday cup current (spot-size=2).

We initially measured micro-strips both because this measurement provides preliminary information to prepare the SNSPD fabrication, both because recent studies demonstrated that it is possible to realize SNSPD with $2\mu m$ wide strips [83].
As shown in Fig.2.20, we measured a deep hysteresis in the IV-curve for wider strips [84]. We also realized w = 400 nm and observed the hysteretic behaviour in the temperature

[3]The film was fabricated by *CNR-SPIN* Salerno and Department of Physics *"E. R. Caianiello"*, Università degli Studi di Salerno, Fisciano, Salerno

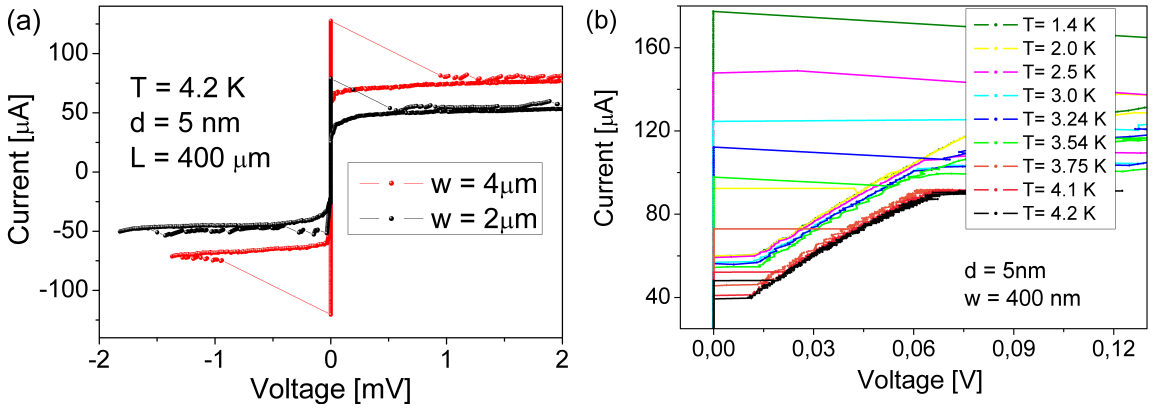

Figure 2.20: Current-voltage characteristics of 400 μm long NbRe strips. (a) IV curve for w = 4 μm and w = 2 μm at T=4,2K. (b) Hysteretic IV curves measured from T = 1,4 K to T = 4,2 K. The strip width is 400 nm.

interval $1,4-4,2$ K. According with Eq.1.25, the hysteresis is necessary to observe a pulse in correspondence of photon absorption. At 4,2K the measured hysteresis is about $\Delta I \approx 10 \mu A$ and it becomes bigger as the temperature decreases; hence we can claim that NbRe nanowires can be used as detectors also at 4,2K.

Summary

In this chapter the study of the fabrication process, materials, measurement setup, is presented.
I first described the fabrication process used to realize the SNSPD and the parallel nanowires geometry. A special care was given to the study of different materials, namely the well known superconductors NbN - NbTiN and other amorphous materials, such as MoSi and NbRe.
During this thesis, lot of work was dedicated to the realization of innovative SNSPDs, to the realization of a new and easily transportable cryogenic insert as well as a portable electronic measurement setup.

CHAPTER 3

Study of Dark Counts in SNSPDs

Abstract: As mentioned before, the low DCR is one of the attractive features of SNSPD detectors but, despite the low noise value, a deeper understanding of the phenomenon which leads to the generation of intrinsic dark counts would open the way to a even lower DCR device. Indeed, it is not possible to discriminate dark pulses with a trigger level as they exhibit the same amplitude of photon pulses[1] and just a microscopic description can address the fabrication and measurement processes towards a zero noise detector.
Even though dark count generation mechanism is still poorly understood, there are models which identify the thermally activated movement of vortices as the cause of dark counts. A vortex is a normal region which arises because of magnetic field and imperfections in the fabrication; moreover, when a specific temperature (BKT temperature) is passed, a phase transition occurs and vortices enter a disordered phase [85,86].
All vortices are shielded by shielding currents and move under the effect of the applied bias; such a movement may give rise to a change of the wave function phase of 2π also called phase slip event and one or more of them lead to the generation of a dark count.
In this chapter a description of phase slips and vortices is provided and two models which pretend to predict the dark count rate are described. First we will focus on one-dimensional nanowires, then some experimental results on 2D systems are presented.

3.1 Dark counts theoretical models

The spontaneous transition from the superconducting state to the normal state below the critical temperature, which triggers the emission of a dark count in the SNSPDs, is ascribed to stochastic dissipative processes such as the change of 2π of the wave function phase, also

[1] Dark pulses averaged amplitude is slightly higher from the photon respective, but it's still indistinguishable within the experimental uncertainty.

called *phase slip*, introduced by Little in 1967 [87]. Phase slips are physically related to the motion of vortices in type-II superconductors which give rise to a finite resistance below T_c [88]; in a 1D system, they produce a sudden change of phase by 2π which gives rise to a voltage pulse [89]. In 2D superconductors, the appearance of a resistance below $T_c(0)$ is described by Berezinsky-Kosterlitz-Thouless (BKT) transition [85].
In this section I briefly describe the dark count models in 2D superconductors.

Vortices in 2D systems

As shown in [6, 90–92] the origin of fluctuations in 2D superconductors is due to the motion of vortices. A vortex is a normal core of approximate diameter ξ surrounded by shielding currents and each vortex contains a quantum flux of $\Phi_0 = h/2e$. The motion of vortices in a superconducting strip is described in [93] and in the absence of external current vortices are *pinned* by the imperfections and cannot move while, for a sufficiently high current, they move under the effect of Lorentz force. The quasi-particles excited in the normal core of a vortex interact with the lattice and the effect is a viscous drag. Magnetic vortices in two-dimensional superconductors, either due to an externally applied magnetic field, to the magnetic self-field caused by the bias current I_b or by thermal fluctuations of strengths $k_B T$, are energetically stable as soon as the width w satisfies the inequality [94, 95]

$$w \approx 4.4\xi(T). \tag{3.1}$$

Vortices can appear in a 2D superconductor for two different phenomena:

- vortices overcoming the edge barrier (VH)
- unbinding of vortex-antivortex pairs (VAP)

and, in each case, a energetic barrier appears which is passed when the dark count event occurs. Indeed, the dark count rate depends exponentially on the bias current (see Fig.1.13) and on the temperature and this dependence can be expressed in terms of Boltzmann factor in the presence of an energy barrier $U(I_b, T)$

$$\Gamma_{DC}(I_b, T) = \Omega \exp\left[-U(I_b, T)/k_B T\right] \tag{3.2}$$

where Ω is the expected rate.
If the energy can be expanded in power series in terms of $I_b \sim I_c$

$$U(I_b, T) \approx U(I_c, T) + \left.\frac{dU(I_b, T)}{dI_b}\right|_{I_b = I_c} (I_b - I_c) \tag{3.3}$$

where I_c is the critical current, eq.3.2 becomes

$$\Gamma_{DC}(I_b, T) = \Omega' \exp\left[-\frac{I_c}{k_B T} \left.\frac{dU(I_b, T)}{dI_b}\right|_{I_b = I_c} \cdot \frac{I_b}{I_c}\right] \tag{3.4}$$

which gives the measured dependence on the bias current and on the temperature, independently on the DC model.

Vortices overcoming the edge barrier. When a Type II SC enters in the mixed state[2], according with the theory of Abrikosof and Pearl [28, 29] the magnetic field can enter in the superconductor as normal core vortices yielding a quantum flux Φ_0. In the case of SNSPD, where the device is polarized close to the critical current, the condition to reach the mixed state is often accomplished.
Gibbs free energy for the entrance of a vortex at the edge of the strip, which depends on the bias current I_b, the temperature T and the distance x from the edges of the strip, is given by [6]

$$G(T, I_b, x)_{VH} = E_B(T, I_b) \left\{ \ln \left[\frac{2w}{\pi\xi(T)} \sin\left(\frac{\pi x}{w}\right) \right] - \frac{I_b}{I_B(T, I_b)} \frac{\pi}{w} \left[x - \frac{\xi(T)}{2} \right] \right\} \tag{3.5}$$

where the first term is the vortex nucleation energy and the second term represents the

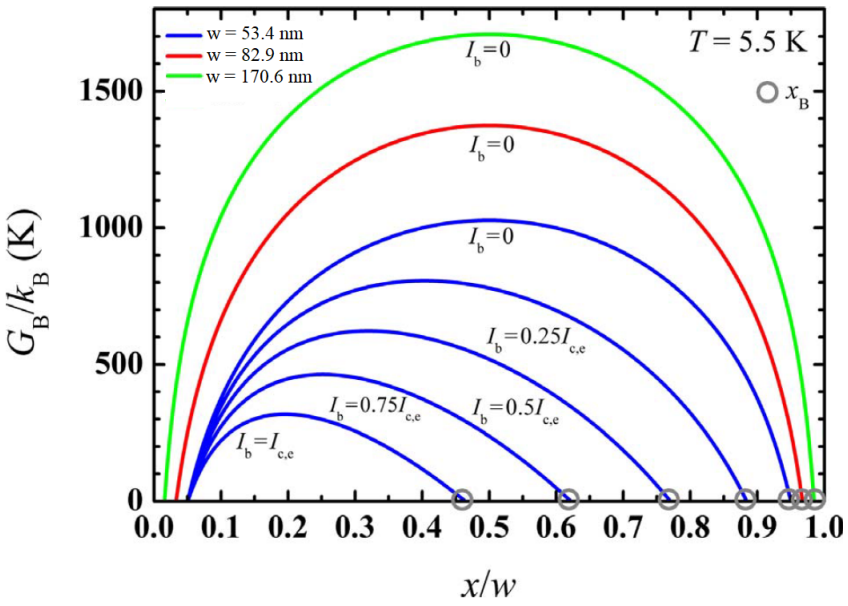

Figure 3.1: Plot of Gibbs free energy for different widths and bias current values at the fixed temperature of 5.5K [6]. The term x_B represents the barrier width.

interaction of a vortex with the bias current; E_B and I_B are, respectively, the energy and current scales, given by

$$E_B(T, I_b) = \frac{\Phi_0^2}{2\pi\mu_0\Lambda(T, I_b)} \qquad I_B(T, I_b) = \frac{\Phi_0}{2\mu_0\Lambda(T, I_b)} \qquad \Lambda = 2\frac{\lambda^2}{d} \tag{3.6}$$

In eq.3.5 the effects due to external fields or to the vortex finite size are neglected.
As one can see from the plot of eq.3.5 in Fig.3.1, there is an energy barrier for vortex entrance

[2]A type II SC is found in the mixed state when the applied field H is $H_{c1} < H < H_{c2}$.

in the strip in any case; the barrier increases with the strip width and decreases as the bias current increases.
The rate at which a vortex overcomes the energy barrier is given by the Boltzmann factor calculated in the maximum $G_{max}(T, I_b, x)$ [96,97]

$$\Gamma_{VH}(I_b, T) = \alpha_{VH} \frac{I_b}{I_c} \exp\left[-G_{max}(T, I_b)/k_B T\right] \tag{3.7}$$

where α_{VH} is a term which accounts for the attempted rate and the geometry. As we'll see later, this rate corresponds, in a specific temperature regime, to the dark counts rate.

Unbinding of vortex-antivortex pairs. In thin films, thermal fluctuations can excite vortex-antivortex pairs (VAP) which consist of two coupled vortices with shielding supercurrents circulating in opposite verses. The two vortices in the VAP bound state can dissociate when the temperature T_{BKT} is overcome.
The interaction between two vortices of a VAP depends logarithmically on the distance r among cores [98]

$$U(r) = A(T) ln\left[\frac{r}{\xi(T)}\right] + 2\mu_c(T), \qquad A(T) = \frac{\Phi_0^2}{\pi \mu_0 \Lambda(T)} \tag{3.8}$$

where $A(T)$ is the vortex interaction scale and μ_C is the core potential. The VAPs are bound at temperatures below T_{BKT}, whereas for higher temperatures, the superconductor enters a disordered phase in which vortices and anti-vortices move in opposite directions under the effect of Lorentz force [6]. Below T_{KBT} the pair is still bound and the applied current interacts with the bound VAPs via the Lorentz force that exerts a torque which orients the pair perpendicularly to the current. Under the effect of an increasing bias current, the vortices in the pair are then pulled apart through a reduction of their binding energy (see eq.3.9). Consequently, under the effect of a bias current, the binding energy passes in a minimum (pair oriented perpendicularly to the current) and than increases again (pairs moving in opposite directions). The minimum is reached when the condition $r_m = 2.6\xi(T) I_c/I_b$ and the energy is given by the expression

$$U_{VAP,m}(T, I_b) = \frac{A(T)}{\epsilon} \left[ln\left(\frac{2.6 I_c(T)}{I_b}\right) - 1 + \frac{I_b}{2.6 I_c(T)}\right] \tag{3.9}$$

where ϵ is the VAP polarizability.
A thermal fluctuation $k_B T$ overcomes the binding energy with a rate given by the Boltzmann factor

$$\Gamma_{VAP} = \Omega_{VAP} \exp\left[-\frac{U_{VAP,m}(T, I_b)}{k_B T}\right] \tag{3.10}$$

where Ω_{VAP} is the attempted rate. When the binding energy is overcome, the VAP is broken and the two vortices move in opposite directions leading to dissipation and to the appearance of normal domains, registered as dark counts events [99].
If the distance between the vortices in a pair differs from r_m, the energy $U(r)$ in eq.3.8 will exceed the value of 3.9 and the probability of pair breaking will be smaller than 3.10.

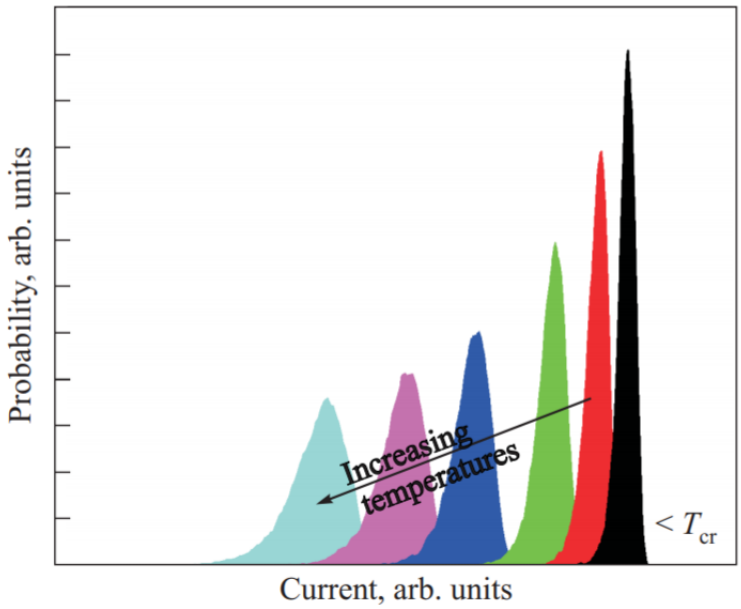

Figure 3.2: A general scheme of switching current distributions as a function of the bias current at different temperatures [7].

3.2 Study of the switching current distributions

A powerful tool to investigate the shape of a potential barrier or the behaviour of fluctuations in a SC as a function of temperature, bias current and magnetic field, is the analysis of switching current distributions [7]. When this method is applied, the bias current is slowly ramped from $I_b = 0$ to $I_b \to I_c$ and the device may switch from a zero-voltage to a finite voltage state at $I_b < I_c$. This corresponds to the state escaping from a energy minimum by a thermally or quantum activated process. The value of bias current at which the escape occurs is referred as *switching current* I_{SW}.

The study of switching currents distributions as a function of temperature and magnetic field is widely used to study the potential well of Josephson junctions[3] and gave a markable contribute to the experimental analysis of macroscopic quantum tunnelling (MQT[4]) phenomenon [100].

In Fig.3.2 one can observe a simulation of typical measurements of switching current distributions $P(I)$. This distribution is generally asymmetric and left tailed due to the asymp-

[3]A Josephson junction is a device composed by two superconducting electrodes separated by a physical barrier which consists of a normal material as well as an insulator, a ferromagnet, a bridge or a constriction [29].

[4]In Josephson junctions Cooper pairs can cross the insulator barrier by tunnelling without applying and voltage with the effect of a measurable current flow. This phenomenon is referred as Josephson effect [29] and it is an example of macroscopic quantum tunnelling because the tunnel effect, which is a pure quantum phenomenon, can be observed trough a macroscopic quantity, i.e. a measurable current.

totic approach of I_b to I_c. The mean switching current value $< I_{SW} >$ decreases with the temperature like the critical current, as expected. The distributions generally broaden by increasing the temperature and, as they are normalized (i.e. $\int_0^{I_c} P(I)dI = 1$), the probability of $< I_{SW} >$ decreases with the temperature.
The broadening, the asymmetry and the tail of a distribution are important parameters which can be quantified by calculating the standard deviation, the skewness and the kurtosis.
The standard deviation σ is a measure of the spreading of a distribution around the mean value and it is defined as the square root of the variance σ^2

$$\sigma = \sqrt{\frac{\sum_{i=1}^{i=N}(x_i - \bar{x})^2}{N-1}} \tag{3.11}$$

where x_i are the data points, $\bar{x}$ is the average value and N is the number of points.
The skewness is a measure of symmetry, or more precisely, the lack of symmetry and it can be calculated as follows

$$s = \frac{\sum_{i=1}^{i=N}(x_i - \bar{x})^3/N}{\sigma^3}; \tag{3.12}$$

for symmetric distributions $s = 0$ while for left (right) skewed[5] distributions $s < 0$ ($s > 0$).
Kurtosis is a measure of whether the data are heavy-tailed or light-tailed relative to a normal distribution. That is, data sets with high kurtosis tend to have heavy tails, and data sets with low kurtosis tend to have light tails. The kurtosis can be calculated with the expression

$$k = \frac{\sum_{i=1}^{i=N}(x_i - \bar{x})^4/N}{\sigma^4}. \tag{3.13}$$

The kurtosis for a standard normal distribution is $k = 3$.
All the parameters introduced here are used to quantify the deviation of a dataset from the normal distribution and will be widely used in what follows.
Switching current distributions and dark count are strictly related. Indeed, the spontaneous switching registered ad $I_{SW} < I_c$ is equivalent to a dark count event occurred at $I_b = I_{SW}$. The DCR can hence be calculated from the distributions trough the formula introduced by Fulton and Dunkleberger [101]

$$\Gamma_{DC} = \frac{dI}{dt}\frac{1}{\Delta I}\ln\left(\frac{\sum_{j=1}^{k} P(j)}{\sum_{i=1}^{k-1} P(i)}\right) \tag{3.14}$$

where ΔI is the bin size, dI/dt the current sweep rate and i, j are the bins; k corresponds to the bin of the specific bias current value taken in exam.

[5] With left skewed distributions we mean that the left tail is longer than the right tail.

Phase slips in 1D nanowires

A nanowire is considered one dimensional when its width and thickness (or diameter) are smaller than the size of Cooper pairs, i.e. smaller than the coherence length ξ. In this case, the fluctuations can lead to the vanishing of the order parameter and to a phase slip [87]. A quantitative description of this phenomenon was developed by Langer, Ambegaokar, McCumber and Halperin [102, 103], and the results are taken here as starting point[6].
Non-trivial thermal fluctuations of the order parameter lead to the vanishing of Δ accompanied by a phase slip of $\pm\pi$ [104]. According with Josephson equation [29]

$$\dot{\varphi} = \frac{2eV}{\hbar} \tag{3.15}$$

this change in the phase produce a finite voltage. In absence of applied current or voltage, the rate of positive and negative phase slips is the same $\Gamma_+ = \Gamma_-$, $\dot{\varphi} = 0$ and, hence, no net voltage across the device can occur. The applied bias current breaks the symmetry between Γ_+ and Γ_- and this unbalance leads to a change in the phase and, hence, to a voltage.
The bias current makes phase slippage in the direction antiparallel to I_b more probable than in the direction parallel to the current and the free-energy difference between these two possibilities is $\delta F_{PS} = h/2eI_b$ [6]. Therefore, the phase slip rate can be written as

$$\Gamma_{TPS}(T, I_b) = \alpha_{TPS} \exp\left[-\frac{\Delta F_{PS}(T, I_b)}{k_b T}\right] \sinh\left(-\frac{\delta F_{PS}}{2k_B T}\right) \tag{3.16}$$

The term $\Delta F_{PS}(T, I_b)$ is the energy required to destroy the order parameter and equals the condensation energy contained in a volume of the cross section of the wire, times the coherence length

$$\Delta F_{PS}(T, I_b) = \frac{8\sqrt{2}}{3} \frac{B_c^2(T, I_b)}{2\mu_0} A\xi(T); \tag{3.17}$$

the second term in eq.3.16 accounts for the unbalance between positive and negative phase slips.
According with theoretical models and simulations (see [10]), the potential barrier can be overcome also by tunnel effect. In this case the *quantum phase slip* rate becomes

$$\Gamma_{QPS}(T, I_b) = \alpha_{QPS} \exp\left[-\frac{\Delta F_{PS}(T, I_b)}{\hbar/\tau_{GL}}\right] \sinh\left(-\frac{\delta F_{PS}}{2\hbar/\tau_{GL}}\right) \tag{3.18}$$

where the energy $k_B T$ was replaced by the quantum scale energy $\hbar/\tau_{GL}$ The Ginzburg-Landau time τ_{GL} depends on the temperature as follows

$$\tau_{GL} = \frac{\pi\hbar}{8k_B\left[T_c(0) - T\right]}. \tag{3.19}$$

Establishing the relationship between individual phase slips and switching current distributions (SCD) provides a tool to study phase slips, to help establish whether they are caused by thermal fluctuations or by macroscopic quantum tunnelling.

[6] A complete description of the fabrication process and superconductivity in a nanowire can be found in [89].

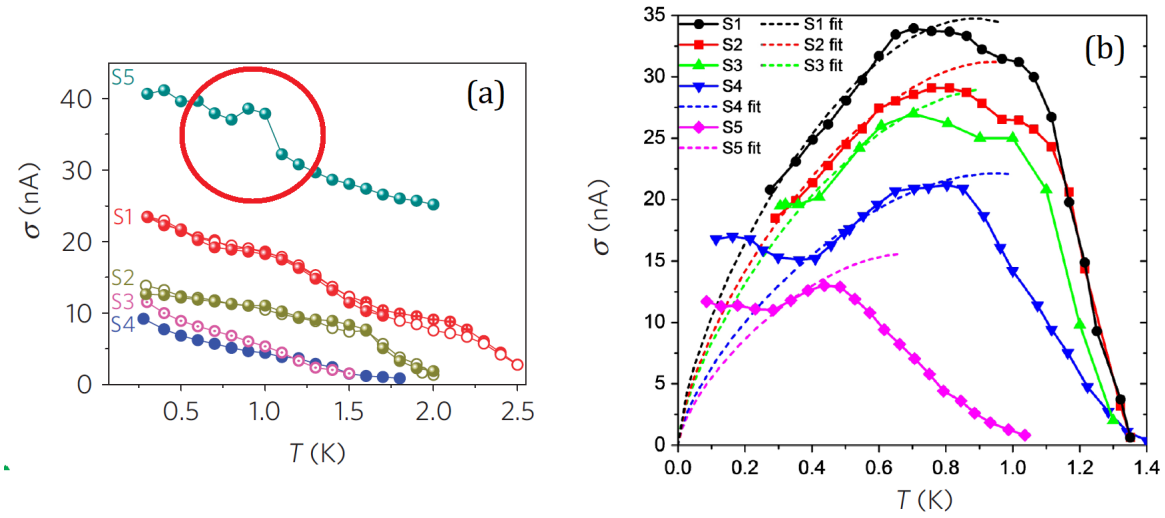

Figure 3.3: Standard deviations of switching current distributions in (a) MoGe [8] and (b) Al [9] nanowires. The standard deviations indicates that the distributions broaden as the temperature decreases. Red circle may indicate a single phase slip induced switching.

Heating model in 1D. In the paper presented by Fulton and Dunkleberger, where SCD are introduced to study dissipation phenomena in Josephson junctions, the distributions become narrower as the temperature decreases. This is a reasonable result in the scenario which identifies thermal fluctuations as a cause of spreading.
In [9] the authors measure the switching current distributions of Al nanowires and they observe that the spreading, quantified by σ has a non-monotonous dependence on the temperature. The same result was found in some MoGe nanowires measured in [8].

In Fig.3.3 the standard deviation of switching currents distributions of MoGe (a) and Al (b) nanowires are shown. As one can see, there is a temperature regime in which the distributions become broader as T increases; in this regime $\sigma \propto T^{2/3}$ and this is the same dependence as the critical field in eq.3.17. This means that, before a crossover temperature T^*, after which the broadening decreases, the phase slip rate is the same as the switching rate. Hence, below T^*, a single phase slip can produce the switching.
Conversely, above T^* the model and the simulations presented in [10,105] prove that multiple phase slips are required to produce the switching. According with this model, a phase slip produce a Joule heating which can be estimated with the use of Josephson equation

$$\frac{d\varphi}{dt} = \frac{2eV}{\hbar} = \frac{2\pi V}{\Phi_0} \longrightarrow W_{ps} = \int dt IV = I \int_0^{2\pi} d\Phi \frac{\hbar}{2e} = \Phi_0 I \tag{3.20}$$

$$R = \frac{V}{I} = \frac{1}{I}\frac{\Phi_0}{2\pi}\frac{d\varphi}{dt} = \frac{\Phi_0 \Gamma(T,I)}{I} \tag{3.21}$$

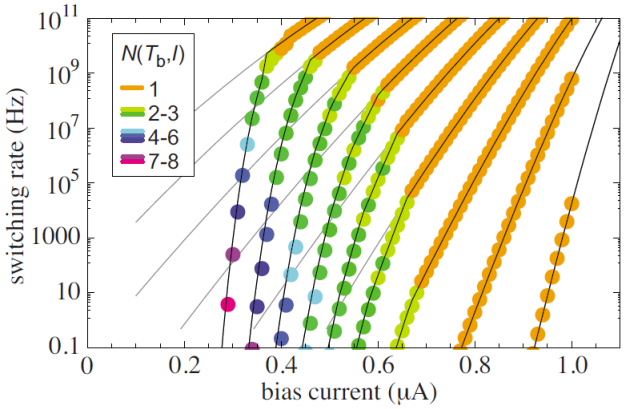

Figure 3.4: Simulation of the switching rates as a function of bias current, temperature and number of phase slips [10].

which gives the following expression for the heat

$$Q_{ps} = \frac{I^2 R(T,I)}{AL} = \frac{W_{ps}\Gamma(T,I)}{AL} \tag{3.22}$$

where $\Gamma = (\Gamma_- - \Gamma_+)$, A is nanowire cross section and L its length.
One can now introduce the parameter η which express the temperature jump due to a phase slip as $\eta = T_f - T_i$ where T_f and T_i are the nanowire temperatures before and after the PS event. With this quantity it is possible to write a Langevin equation for the effective temperature T in the nanowire as a function of the bath temperature T_b and the current I

$$\frac{dT}{dt} = -\alpha(T,T_b)(T - T_b) + \eta(T,I)\Gamma(T,I); \tag{3.23}$$

the first term accounts for the thermalization with the bath in the hypothesis that the nanowire is suspended and hence it can thermalize just trough the edges, connected to contact pads at $T_p = T_b$ and here α is a term which accounts for the thermal conductivity. The second term is a source term which accounts for the Joule heating due to the PS event, calculated above.
Eq.3.23 can be expressed in a discrete form where the time evolution is translated into steps at which the temperature T_i and hence η change. The number of steps $N(T,I)$ required to reach the switching is an output that can be estimated by numerical simulation. The number of steps is nothing but the consecutive PS required to reach the temperature $T = T_{SW}$ and the result of simulations is that, above a temperature T^*, this number is higher than one.
It is important to notice that, as $N(T,I)$ increases, the switching rate calculated with the expression 3.14 bends as shown in Fig.3.4 and this result is significant to enlighten the experimental results presented below.
In [9,105] the authors also observe a temperature regime in which the PS barrier is overcome by tunnelling. This regime is identified by the saturation of σ in Fig.3.3. The quantum

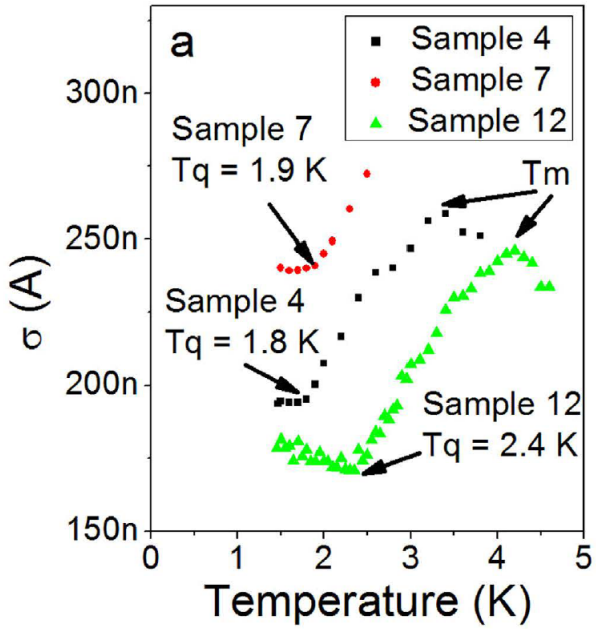

Figure 3.5: Standard deviation of the switching currents distributions on NbN SNSPDs as a function of the temperature [11].

phase slip regime is not explored in the experimental data presented below and hence this result is not described here in details.

Multiple fluctuations regime in SNSPD: experimental results

The measurement of SNSPD switching currents distributions to investigate the origin of dark counts, started in 2015 [11]; the authors here measure the SCD of a NbN SNSPD and they observe, as in the 1D cases, three different dependences of the standard deviation σ on the temperature.

By looking at Fig.3.5, it is possible to notice a saturation zone for $T < T_q$, a region between T_q and T_M where $\sigma \propto T^b$ and a regime for $T > T_M$ in which the standard deviation decreases as the temperature is raised. By making a parallelism with the 1D case, the authors of [11] claim that the processes producing the switching are three: quantum tunnelling for $T < T_q$, single phase slip for $T_q < T < T_M$, multiple phase slips at $T > T_M$.

Inspired by the work of Murphy *et al.*, in [53] we measured the SCD in a round NbTiN SNSPD [7] from T=0.3K to T=4K in order to investigate the multiple phase slip regime. During the experiment, the sample was anchored to the ^3He pot chamber of HELIOX Oxford cryostat, whose filters and electronics are described in [106]. Each SCD includes 10000

[7] See Fig.2.7

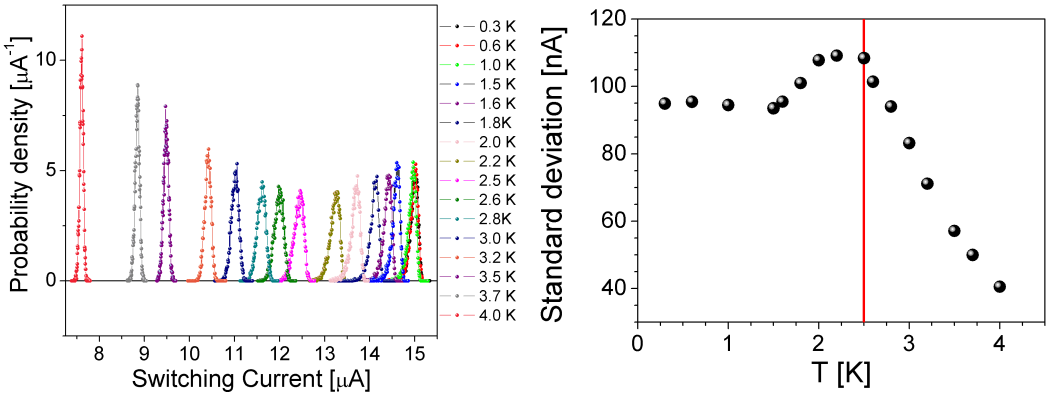

Figure 3.6: Switching current distributions and standard deviation of a NbTiN SNSPD from 0.3K to 4K.

switching events and the sweep rate is 845μA/s.
As shown in Fig.3.6 we could distinguish three temperature regimes:

- $0.3K < T < 1.5K$ - in this regime the distributions are *frozen* and the width does not depend on the temperature. We cannot claim that this is a quantum regime because we cannot exclude other effects as a saturation of the Joule heating compensation;
- $1.5K < T < 2.5K$ - the distributions become broader as the temperature increases;
- $T > 2.5K$ - the distributions become narrower as the temperature is raised.

Keeping in mind the results shown in the previous paragraph, the standard deviation trend suggests that also in wider strips (here w=80nm$\gg \xi$) there is a regime in which a single thermal fluctuation event can produce the switching while, at higher temperatures, more fluctuations are required. Anyway, it is not possible to apply the same formalism as in the case of 1D nanowires for two reasons: first, the SNSPD strip can be considered a pseudo-2D system because the width and length are larger than the coherence length but the bias current verse breaks the symmetry just in the direction of carriers flow, then, in Type II SC we cannot ignore the vortices which appear in the strip as VAP and VH. Hence, we will indicate each discrete event which produces a local heating as a thermal fluctuation, despite its nature.
To further investigate if $T = 2.5K$ is a crossover temperature between a single to multiple fluctuations regime, we calculated the skewness and kurtosis with eq.3.12-3.13 and the results are shown in Fig.3.7. It can be clearly seen that T=2.5K is a crossover temperature not only for the spreading but also for the symmetry of the distributions. Indeed, the skewness passes from the value -1, which indicates a left tail, to slightly less than zero that is the value assumed by a normal distribution. The kurtosis also indicates that the distributions have long tails before 2.5K and then become similar to normal distributions which has k=3.

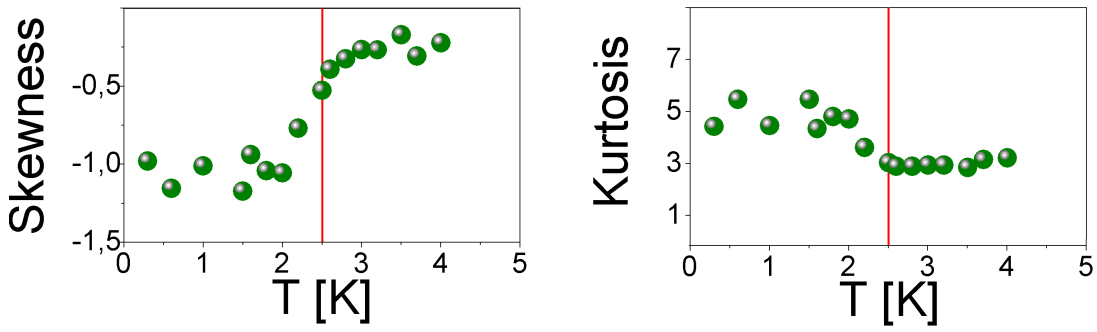

Figure 3.7: Skewness and Kurtosis of NbTiN SNSPD switching current distributions measured from 0.3K to 4K.

In order to explain this change in the symmetry, we introduced in [53] the fluctuation rate

$$\Gamma_F = \Omega_F(I_b, I_c, T) \exp\left[-\frac{U_F(I_b, I_c, T)}{k_B T}\right] \tag{3.24}$$

which represents the rate at which a single fluctuation event occurs as a function of a general potential barrier. In the hypothesis that the barrier $U_F(I_b, I_c, T)$ vanishes at $I_b = I_c$ one can write

$$U_F(I_b, I_c, T) \approx \left.\frac{dU(I_b, I_c, T)}{dI_b}\right|_{I_b=I_c} \cdot (I_b - I_c) \equiv \alpha(I_B - 1)k_B T \tag{3.25}$$

where we introduced the normalized current $I_B = I_b/I_c$ and α to express the derivative term multiplied by $I_c/k_B T$. Hence the fluctuations rate becomes

$$\Gamma_F = K e^{-\alpha I_B} \qquad\qquad K = \Omega_F e^{\alpha}. \tag{3.26}$$

In the hypothesis that a single fluctuation produces the switching, we have $\Gamma_F = \Gamma_{SW}$. If more than one fluctuation event are required, we should estimate the probability that two (or more) stochastic and independent events occur in a close time and position. In this case the combined rate will be the product of the single rates and a coefficient that accounts for the correlation between the thermal events

$$\Gamma_n(I_B, T) = \frac{(\Delta t p_s)^{n-1}}{(n-1)!} [\Gamma_F(I_B, T)]^n \tag{3.27}$$

where Δt accounts for the thermalization time, n is the number of events and p_s is the probability that a fluctuation event occurs within a spatial region sufficiently close to another to sum the cumulative heating. The switching rate due to n multiple events heating can be expressed as

$$\Gamma_{SW}(I_B, T) = \Gamma_n(I_B, T) = A_n(I_B, T) \cdot e^{n\alpha I_B} \qquad\qquad A_n = K^n \frac{(\Delta t p_s)^{n-1}}{(n-1)!} \tag{3.28}$$

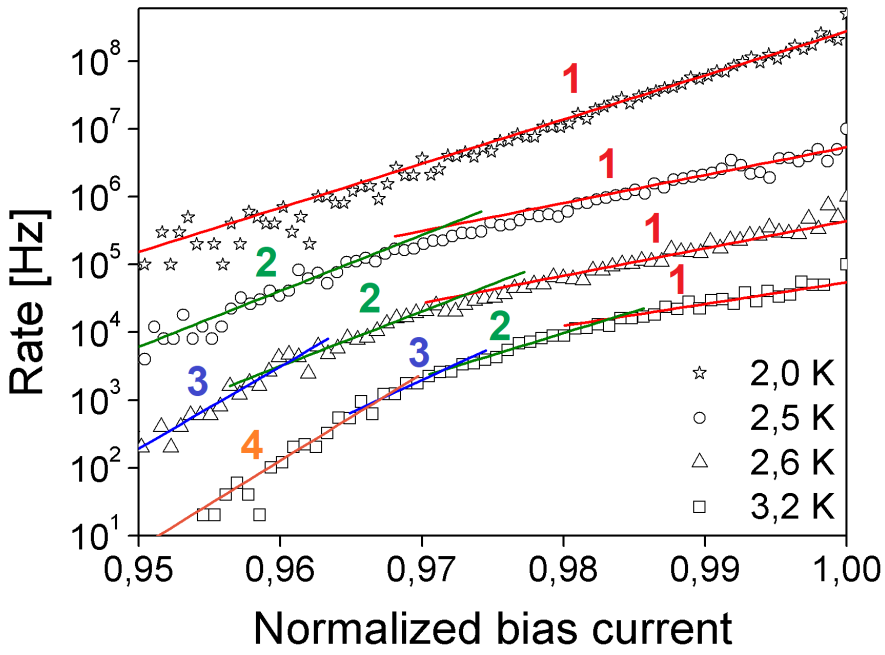

Figure 3.8: Switching rates at 3.2K, 2.6K, 2.5K and 2.0K multiplied, respectively, by 1, 10, 100, 1000. The lines correspond to the fitting procedure results and the numbers indicate the fluctuation events required in order to produce the switching.

The hypothesis of multiple events switching explains the crossover temperature observed in the standard deviation, skewness and kurtosis. Indeed, when multiple events are required, the statistics is not governed by the physical process itself but by the probability that two (or more) stochastic events occur *simultaneously*[8]; the combination of two stochastic events is governed by a normal distribution and that explains the symmetrization observed in the distributions.
To verify our hypothesis, we calculated the switching rates with eq.3.14. The switching rate corresponds to the DCR and the results are presented in Fig.3.8.

The fitting procedure is the following: in high bias current region we fitted the data to calculate the parameters α and A_1. The other lines in Fig.3.8 are obtained by multiplying the exponent in eq.3.28 for the number of fluctuations n and by adjusting the prefactor A_n. The fact that dark count rates bend just as predicted by simulations of multiple phase slips in Fig.3.4 and the fact that this trend can be guessed by multiplying Γ_F by itself as much time as the number of events, prove that also in SNSPD there is a temperature above which multiple thermal fluctuations are required to produce a dark count.

[8]Within a time interval and an area which make the action of the heating due to each event cumulatively affects the same particles inside the superconductor.

Moreover, as the bias current decreases, more events are required to produce a dark count. This result further clarifies the dependence of σ on the temperature; indeed, if the energy released by a thermal fluctuation is proportional to the current (as expected in the case of Joule heating), the lower the temperature, the higher the mean switching current. Hence, when the temperature is lower, the current flowing in the strip is higher and each fluctuation releases a larger amount of energy. In this case a single fluctuation causes a dark count. As the temperature increases, the mean switching current and the maximum bias current flowing in the strip are lower, as well as the energy released by a fluctuation event. In the case of higher temperature (lower current) more events are required and their number increases with the temperature. This observation explains the decrease of σ in the third temperature regime.
This important experimental result proves that also in SNSPD the operating temperature can be tuned to change the mechanism which leads to the switching and, hence, to a dark count. The bending in the switching rate demonstrates that, for SNSPD, it is not always true that the lowest the temperature the better the DCR because, at higher temperatures and lower bias ($I_B \sim 0.95$) the curve bending is more pronounced and the rate is lower.

Comparison of NbN and NbTiN switching current distributions

With the same technique described in the previous paragraph, we compared the dark counts of two $\oslash = 15\mu m$ round meanders from 0.3K to 6K. The samples are fabricated from 5nm thick films of NbTiN and NbN[9] and the geometric layout is the same [107] for both devices. The fabrication details can be found in [108].
In recent times, NbTiN was introduced because the DCR for this material is lower than for NbN [34]. Moreover, in [108], the authors also observed that in NbTiN SNSPD the timing jitter and the kinetic inductance are smaller, yielding hence to faster devices. In our measurement we confirmed that, in a wide range of currents and temperatures, the dark counts are higher in NbN than in NbTiN, but we also found that this is not always true.

In Fig. 3.9 we show the ratios between DCR in a NbN SNSPD and DCR in a NbTiN SNSPD as a function of the temperature for three fixed bias current values. As one can see from the black curve, when the bias current is relatively small (i.e. $I_b/I_c = 0,975$), the dark count rate in NbN device is 1,5-4 times higher than in NbTiN. However, as the bias current approaches the critical current I_c, the ratio decreases and for $I_b/I_c = 0,995$ one can see that $DCR_{NbN} \leq DCR_{NbTiN}$ (i.e. the ratio is slightly smaller than one).
To give a deeper understanding, we also show separately the DCR as a function of the temperature for three different bias current values in Fig.3.10. It can be noticed that, while for $I_b/I_c = 0,975$ and $I_b/I_c = 0,985$, the dark count rate is higher in NbN, when the relative

[9]The SNSPDs have been fabricated in State Key Laboratory of Functional Materials for Informatics, Shanghai Institute of Microsystem and Information Technology, Chinese Academy of Sciences.

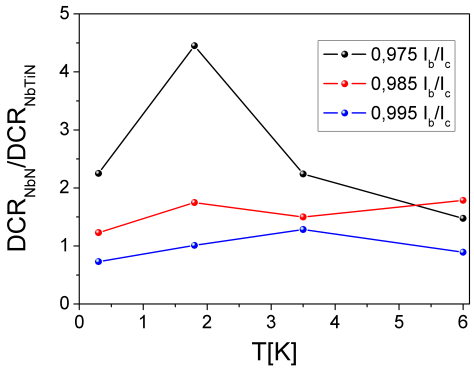

Figure 3.9: Ratio between NbN and NbTiN SNSPDs dark count rates. The black, red and blue curves are the ratios measured at $I_b/I_c = 0,975$, $I_b/I_c = 0,985$ and $I_b/I_c = 0,995$, respectively.

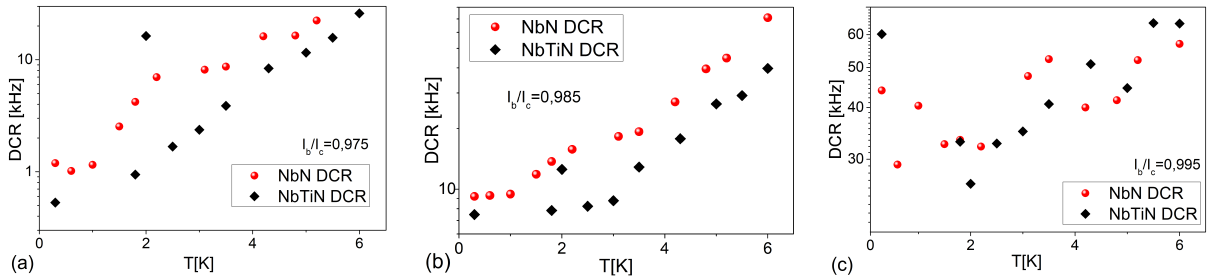

Figure 3.10: NbN and NbTiN dark counts as a function of the temperature at three fixed bias current values:(a) $I_b/I_c = 0,975$, (b) $I_b/I_c = 0,985$, (c) $I_b/I_c = 0,995$.

current is higher, namely $I_b/I_c = 0,995$, the two DCRs become similar and also exhibit a minimum in correspondence of $T \sim 2K$. This result might indicate the best operating current and temperature values, to be tuned in order to maximize the efficiency and minimize the DCR.

As shown in [107], we also repeated the switching currents distributions analysis performed in [53] and the standard deviation and skewness are presented in Fig.3.11. As in [53], we observe the same dependence of σ on the temperature and an inversion at $T = T^*$. With a quick look at Fig.3.11, one can see that the temperature where the σ has a maximum is different from the one of zero-skewness. In details, the zero value of the skewness is reached just at T=6K. Just for this temperature value, we can observe a bending of the switching rate and hence we can conclude that the entrance in the multiple events regime is indicated by the skewness value.

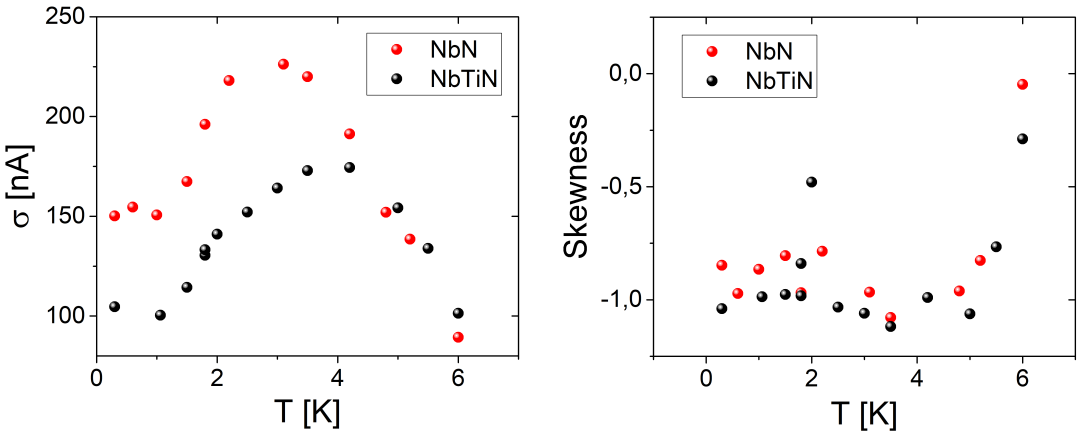

Figure 3.11: A comparison of the skewness and standard deviation of the switching currents distributions from 0.3K to 6K in a NbN and NbTiN SNSPDs

3.3 Study of inter-pulse histograms

To further investigate the dark counts physics in NbTiN SNSPD, we measured the time intervals elapsed between two consecutive dark pulses at fixed bias current and temperature (T=4.2K). Then, we calculated the inter-pulse histogram, the statistic distribution of the measured time intervals.
The resulting distribution is expected to be Poissonian due to the stochastic nature of the observed phenomenon but, as one can see in Fig.3.12, the data exponentially decay but with two different rates.

In the case of a Poissonian inter-pulse histogram, the integral in time of the distribution provides the mean time interval between two consecutive dark counts and its inverse corresponds to the DCR. Here we observe that the mean DCR Γ can be expressed in terms of two decay rates

$$\Gamma = Ke^{-\Gamma t} = \alpha(I_b)\Gamma_1 e^{-\Gamma_1 t} + [1-\alpha(I_b)]\Gamma_2 e^{-\Gamma_2 t} \tag{3.29}$$

which combines two processes occurring with a relative weight *alpha* at two different rates Γ_1 and Γ_2.
We fitted the inter-pulse histogram (IPH) with the function 3.29 with Γ_1, Γ_2, α considered as parameters and repeated the procedure at different bias current values. The results are presented in Fig.3.13. The rate Γ_1 accounts for the contribution in the first branch of the IPH while Γ_2 for the long tail.
In Fig.3.13 one can notice that rate Γ_1 is three order of magnitude higher than Γ_2 at $I_b/I_c = 0.95$ while they approach to each other in high bias current region.
The result presented here can be explained in two ways:

- two distinct processes occur at different rate and with a different dependence on the bias current; the result is that the strip can be found in two different states and the

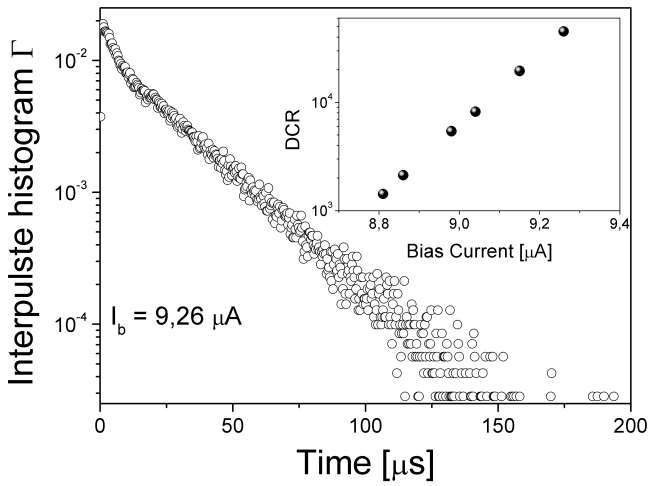

Figure 3.12: Inter-pulse histogram measured at $I_b = 9.26\mu$A.

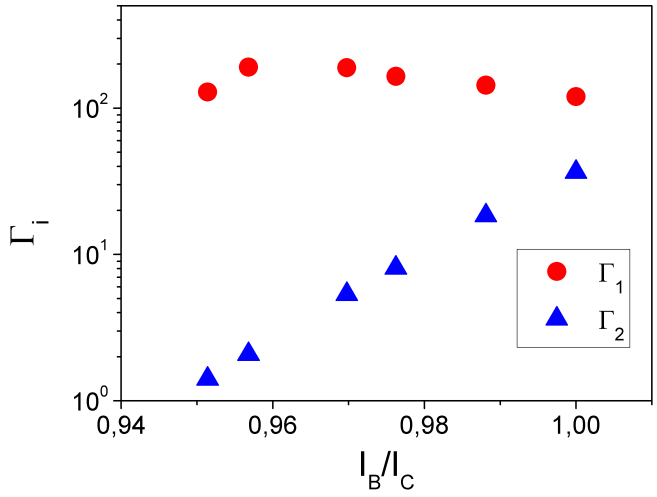

Figure 3.13: Rates calculated by fitting the inter-pulse histograms at different bias currents.

parameter α quantifies the time interval spent in each state;

- The strip has a memory of the previous dark count event (a sort of afterpulse); in the time interval affected by the memory, the DCR is Γ_1, otherwise the rate is Γ_2.

By comparing these results with the data of multiple fluctuation events presented in the previous paragraph, in the first hypothesis, the dependence on the current suggests that Γ_1 is related to multiple fluctuation rate and Γ_2 with single fluctuations rate and double slope observed in the IPH is due to a combined effect of single and multiple fluctuation driven switching.
At the moment, we have no data to support one hypothesis or the other but future measurement at different temperatures can make clear if the two rates are related with single and multiple events. Indeed, if the hypothesis is correct, as the temperature is lowered, Γ_2 should increase.

Summary

In this chapter a brief overview of dark count models in SNSPD is provided. Then I presented the model of thermal dissipation phenomena in one dimensional nanowires and some significant experimental results found in literature. The study of 1D nanowires enlightens the scenario presented by the measurement of switching current distributions of a NbTiN SNSPD. On this device we observe that the phenomenon which produces a dark count depends on the temperature: below a crossover temperature, a single thermal fluctuation can produce a DC, then more events are needed. This results give a deeper understanding of the physics of DC in SNSPD.
The crossover temperature is also observed in a NbN SNSPD and I presented a comparison between SCD analysis in NbN and NbTiN.
Finally, the results of a measurement of mean time between consecutive dark pulses are discussed. The experimental results presented here can confirm what demonstrated with the previous experiment or open the way to a more complicated scenario in which more processes occur at the same time.

CHAPTER 4

Lidar

Abstract: The presence of aerosols in the atmosphere considerably influence the Earth's climate but their concentrations, properties and dynamics are still poorly known. Continuous observational data are required in order to validate models and gain a deeper understanding about the aerosols role in weather changes. What is needed are spatially and temporally observations; both can be provided by using the Lidar technique.
Light detection and ranging (Lidar) method was introduced in 1963 [22] and it is one of the most effective methods to resolve locally the vertical distribution of the absorbing species, which can be located over a distance of about 30km from the sensor. Lidar provides high 4D resolution[1] and consists of a transmitter and a receiver: it is an active sensor that sends into the atmosphere a short laser pulse and measures the elastic backscattered signal from molecules and aerosols. The delay of the received pulse leads to the measurement of the scattering elements position. Further analysis of the backscattered radiation provide other important optical properties of the absorbing species as the backscattering and extinction coefficients, position and altitude of the layers, colour index and so on.
It is possible to observe the aerosols by measuring their light scattering or absorption properties and remote sensing can act as a powerful tool.
In this chapter we give a description of the Lidar technique with a special focus on aerosols detection systems. We will also give an overview of the commonly used detectors types and their properties.

4.1 Lidar - basic concepts

Lidar is a measurement setup used to study the spatial and temporal distribution of remote targets properties. The system configuration consists of a transmitter and receiver as shown

[1] The 4D accounts for spatial and temporal resolution.

in Fig.4.1; the former is composed by laser, beam expander and mirror (MT), the latter by a telescope, filters and detector.

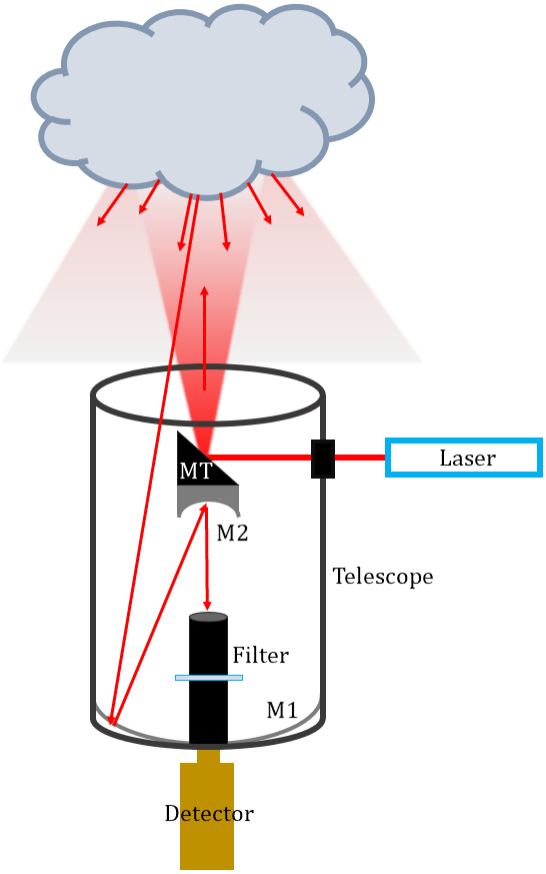

Figure 4.1: Lidar system

Lidar systems are widely used nowadays to study the terrestrial atmosphere and surface both from ground and satellite or aircraft. The working principle is the same of radars: a Lidar measures the time of flight (TOF) of a laser pulse from the moment it is emitted, labelled by the trigger, and the instant in which the pulse, reflected by a distant target, is detected. Then, trough the straightforward formula $d = c \cdot \Delta t/2$ the target distance can be calculated. The difference between Lidars and radars is the wavelength: while radio waves have $\lambda \sim 10^{-3}$ m, the visible/NIR light used in lidar systems has $\lambda \sim 10^{-6}$ m. This means that it is possible to study the presence of smaller objects and to reach higher resolution. Radar can hence be used when the detection of the object is more important than its size and shape. In this case, Lidar si preferable.
In this work I studied the way to include a SNSPD detector in Lidar system and realized and tested the final setup. In order to do that I used the Lidar from different ground based systems in Naples and China[2] used to investigate the presence of aerosols.

Lidar equation

The received signal's intensity depends on many factors, some depending on the acquisition system (telescope geometry, laser power etc.) and others on the atmosphere (transmissivity, scattering cross section and so on). One can write a simple expression to account for these

[2]The system used in Naples is located at University of Naples Federico II. In China I worked with Bejing Research Institute for Telemetry with Lidar systems located in Beijing and Wuhan.

factors [109]

$$P(R) = KG(R)\beta(R)T(R) \tag{4.1}$$

where R is the target's distance, $P(R)$ is the power of backscattered signal, K contains the emitter's performances, $G(R)$ measures the range-dependent geometric factors. The other two parameters, $\beta(R)$ and $T(R)$, are the backscatter and transmission coefficients, which are object of investigation during the measurement. The coefficient $\beta(R)$ stands for the ability of atmosphere to scatter light back into the direction $\theta = \pi$ and it depends on the number N_j of scattering centres and on the scattering cross section $d\sigma(\pi, \lambda)/d\Omega$, according with the formula

$$\beta(R) = \sum_j N_j(R) \frac{d\sigma_j^{scatt}(\pi, \lambda)}{d\Omega} \tag{4.2}$$

where the sum index j refers to different particles and scattering processes.
The transmission term $T(R)$ considers the part of light that gets lost in the pathway between the emission and detection due to absorbance and the scattering by molecules and aerosols in the atmosphere. $T(R)$ can assume the values between 0 and 1 and can be expressed as

$$T(R, \lambda) = \exp\left[-2\int_0^R \alpha(r, \lambda)dr\right]; \tag{4.3}$$

in this expression a factor 2 stands for the two-way transmission path and α is the extinction coefficient defined, similarly to β as

$$\alpha(r, \lambda) = \sum_j N_j(R) \frac{d\sigma_j^{ext}(\pi, \lambda)}{d\Omega} \tag{4.4}$$

where σ_j^{ext} is the cross section of the extinction process.
Emitter performance coefficient K in Eq.4.1 contains the average laser power P_0, the temporal pulse length τ, the telescope's area $A = \pi r^2$ (where r is the telescope radius) and the system efficiency η[3]. It can be written as

$$K = P_0 \frac{c\tau}{2} A\eta. \tag{4.5}$$

The factor $Ac\tau/2$ is the volume from which backscattered light is received at an instant time. Indeed, when the lidar signal is detected at an instant time t, the backscattered light from the initial edge of the pulse comes from the distance $R_1 = ct/2$ and, at the same time, light produced by the last edge arrives from distance $R_2 = c(t - \tau)/2$. Hence, for each pulse, the system receives the signal coming from a volume $A\Delta R = A(R_1 - R_2) = Ac\tau/2$. The laser repetition rate is often expressed as f_{rep}.
The geometric factor $G(R)$ contains the overlap function $O(R)$ and a term R^2 arising from the fact that the telescope area is the centre of a sphere containing the scattering volume.

[3]This factor accounts for the alignment likelihood and the losses due to the optics sizes, reflections and aberrations.

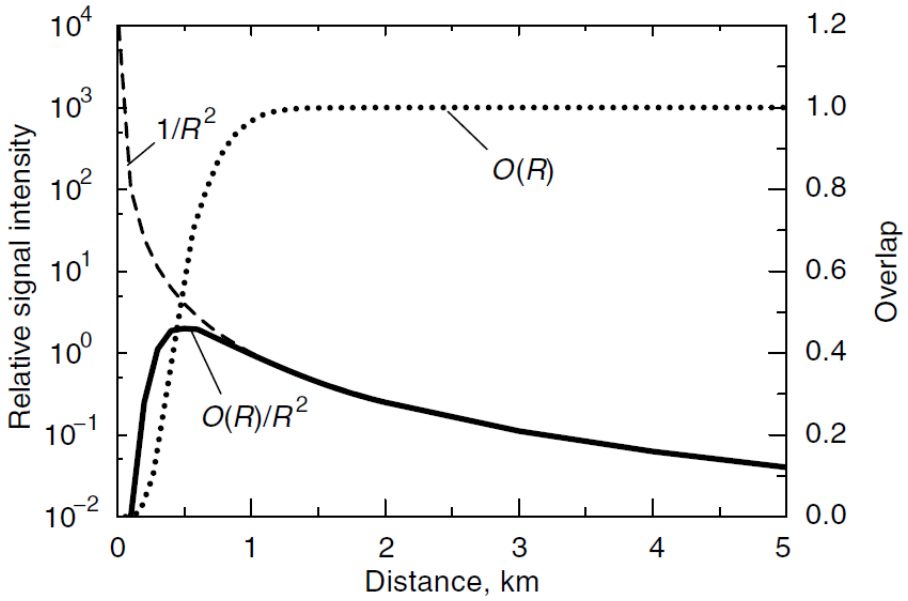

Figure 4.2: Overlap function effect on the signal. The continuous line is the signal, dotted line the overlap function and dashed line the signal after overlap correction.

As shown in Fig.4.1, $O(R)$ varies from 0 to 1 and is a function which accounts of the overlap between the laser beam and the telescope field of view.
In the end, one can rewrite the lidar equation (4.1) as follows

$$P(R,\lambda) = P_0 A \eta \frac{c\tau}{2} G(R)\beta(R,\lambda) \exp\left[-2\int_0^R \alpha(r,\lambda)dr\right] \qquad G(R) = \frac{O(R)}{R^2}. \tag{4.6}$$

4.2 Scattering processes

The atmosphere is composed by molecules, as N_2, O_2, H_2O and aerosols, as salt, ashes, dusts and so on. The dimension of these particles can cover a wide range of amplitudes and their size a is an important parameter to identify the kind of scattering process which will occur when the light is emitted. Indeed, if a is much lower than λ, the elastic scattering can be described by Rayleigh theory while, as the size increases, Mie theory is required (Fig. 4.3). If the wavelength is close to the molecular bonding length also inelastic Raman scattering occurs. The specific scattering process will affect the cross section values and hence β and α parameters.
The cross section is related to the backscatter efficiency Q and the the particle size a though the equation [110]

$$\sigma = \pi a^2 Q. \tag{4.7}$$

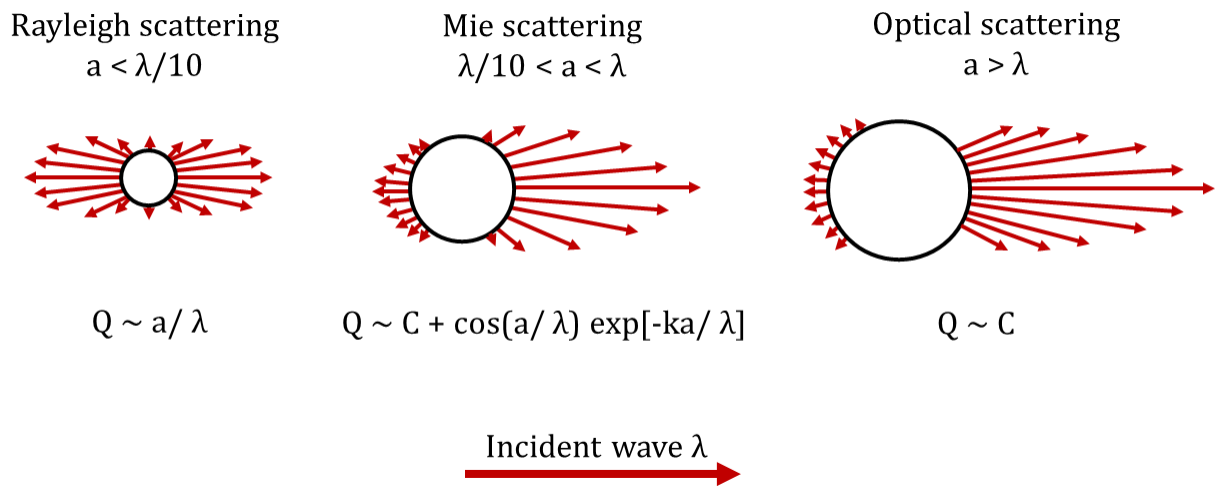

Figure 4.3: Different elastic scattering processes.

Rayleigh scattering. This process refers to the light scattered by air molecules with size up to one tenth of the wavelength. In this model the particle shape is assumed to be spherical and the light is absorbed and emitted again without changing polarization state, orbital angular momentum and energy. Only the momentum direction is modified. When the electromagnetic wavelength passes by the molecule, schematized as a dipole, it will be polarized by the electromagnetic field $\vec{E}$ according with the relation $\mathcal{P} = \epsilon\vec{E}$, where ϵ is the molecule polarizability. If the incoming wave is sinusoidal, the radiation $I(\theta)$ emitted by the molecule at the angle θ depends on the incident radiation I_0, on the wavelength and on the distance R as follows

$$I(\theta) = I_0 \frac{8\pi^4\epsilon^2}{2\lambda^4 R^2}(1 + \cos^2\theta); \tag{4.8}$$

it is important to notice that, in this equation, the scattered light depends on the fourth power of the wavelength hence the smaller the wavelength, the larger the scattered light intensity. Moreover, I depends on the angle θ between the light source and the scattering direction, and we can see from eq.4.8 that it reaches the maximum for $\theta = 0, \pi$. The factor R^2 account for the dependence on the distance between source and target.

Mie scattering. When the particle diameter is roughly the same as the wavelength, then the scattering properties of the medium are described by the Mie theory. The most important difference with Rayleigh scattering is the direction of scattered signal; in particular, as the particle size increases ($a \sim \lambda$), the backscattered intensity decreases and the light mainly moves forward. When $a > \lambda$ we enter in the *optical scattering* regime.
Mie scattering is a complex theory because accounts for the particles' internal interactions.

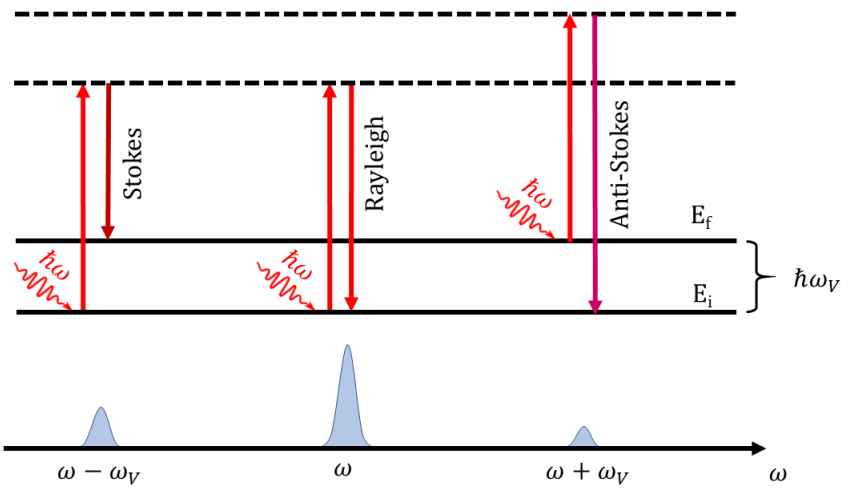

Figure 4.4: Raman effect picture. The incident wavelength can be red-shifted (Stokes lines) or blue-shifted (anti-Stokes lines).

The backscatter efficiency Q in the case of Mie scattering is

$$Q \propto C + \cos\left(\frac{a}{\lambda}\right) e^{-k\frac{a}{\lambda}} \tag{4.9}$$

where C is a constant whose value is determined by the observed molecule and k is a coefficient depending on the backscatter and extinction coefficients β and α. For Rayleigh scattering $Q \propto r/\lambda$ while for optical scattering $Q \propto C$.
As we'll see later, aerosol size lays between 0,1 μm and 1cm. This means that when visible light is used ($400 \leq \lambda \leq 700$ nm) the scattering process is mainly governed by Mie theory.

Raman scattering. This is an inelastic scattering of light which means that there is wavelength shift in the backscattered signal. Raman effect occurs when the incident light frequency is closer to ω_v, the angular frequency associated to molecule vibrations. In this case, the molecule polarizability ϵ oscillates and induces a dipole momentum

$$\mu = \epsilon_0 E_0 sin(\omega t) + \frac{1}{2}\epsilon_1 E_0 cos(\omega - \omega_v)t - \frac{1}{2}\epsilon_1 E_0 cos(\omega + \omega_v)t \tag{4.10}$$

where E_0 is the incident electromagnetic wave amplitude, ω is its frequency and ϵ_0 and ϵ_1 are the equilibrium and oscillating amplitudes of the total polarizability ϵ ($\epsilon = \epsilon_0 + \epsilon_1 sin\omega_v t$).
The three terms in eq.4.10 are responsible, respectively, for the Rayleigh scattering, Stokes and anti-Stokes components in Raman scattering. Hence, if $\omega \sim \omega_v$ it is possible to observe a shift of ω_v in the wavelength (Fig. 4.4).
Hence, the incident photon $\hbar\omega$ leads the molecule to an unstable excited state which will

decay into the initial energy level E_i or to the shifted level $E_v = E_i \pm \hbar\omega_v$. If ν is the vibrational level's quantic number, the selection rule $\Delta\nu = \pm 1$ decrees the allowed energetic levels. The energy released in the decay is transferred to the emitted photon which can produce Stokes ($\Delta\nu = -1$) or anti-Stokes ($\Delta\nu = +1$) lines.
Molecules' dynamic can be very complex and also rotational modes can lead to Raman scattering. The process is the same as the one described above, with the only difference in the resonance frequency ω_r that is the rotational angular frequency. Scattered photons will be shifted of $\pm 2\omega_r$, according with the selection rules $\Delta J = 0, \pm 2$.
The specific value of ω_v and ω_r depends on the molecular species and temperature; indeed Raman effect is used in Lidar technique to identify the molecules or to calculate atmospheric layers' temperature.

4.3 Aerosols detection with elastic Lidar

Aerosols are liquid or solid particles suspended in a gas and they have a size going from $0,1\mu m$ up to $1cm$. The reason of the presence of aerosols in the atmosphere is due to natural and anthropic causes and among them there are vegetal transpiration, volcanic ash, marine salts, desert dust, fossil combustion products, biogenic and anthropic compounds etc. (see Fig. 4.5). Due to their size, the main scattering process which occurs when the light invests the aerosols, is the Mie scattering.
Aerosol particles affect the radiative balance of the Earth by scattering and absorbing solar and terrestrial radiation in the planetary boundary layer[4] (PBL), contributing to greenhouse effect; aerosols are also hygroscopic particles and can act as condensation nuclei of water vapour, playing hence a special role in clouds and humidity formation [111,112]. In particular, the presence of aerosols reduces the amount of solar radiation reaching the ground, dulling the diurnal temperature evolution in the PBL. The weak temperature dynamic reduces the turbulences in the PBL, preventing the entrainment of dry air. The combination of these two effects, the near-surface temperature lowering and the increased moisture int the PBL, leads to the increasing of air humidity which in turn favours the hygroscopic growth of aerosols and enhances the scattering of solar radiation. Moreover, higher air humidity enhances the formation of secondary aerosols.

Accurate measurements of aerosols distribution and dynamics are required to validate atmosphere models and to make predictions. Such measurements can be performed both *in situ* and through remote sensing. The latter provides vertical profiles of aerosols properties while the former furnishes chemicals and physical parameters.
Elastic backscatter Lidar permits the localization of particles when the wavelength of the incident radiation remains unchanged during the scattering process. With this lidar it is

[4] The planetary boundary layer (PBL) is the lowest part of the atmosphere and its behaviour is directly influenced by its contact with a planetary surface. On Earth it usually responds to changes in surface radiative forcing in an hour or less. In this layer physical quantities display rapid fluctuations (turbulence) and vertical mixing is strong. Above the PBL is the *free atmosphere*, where the wind is not affected by surface drag.

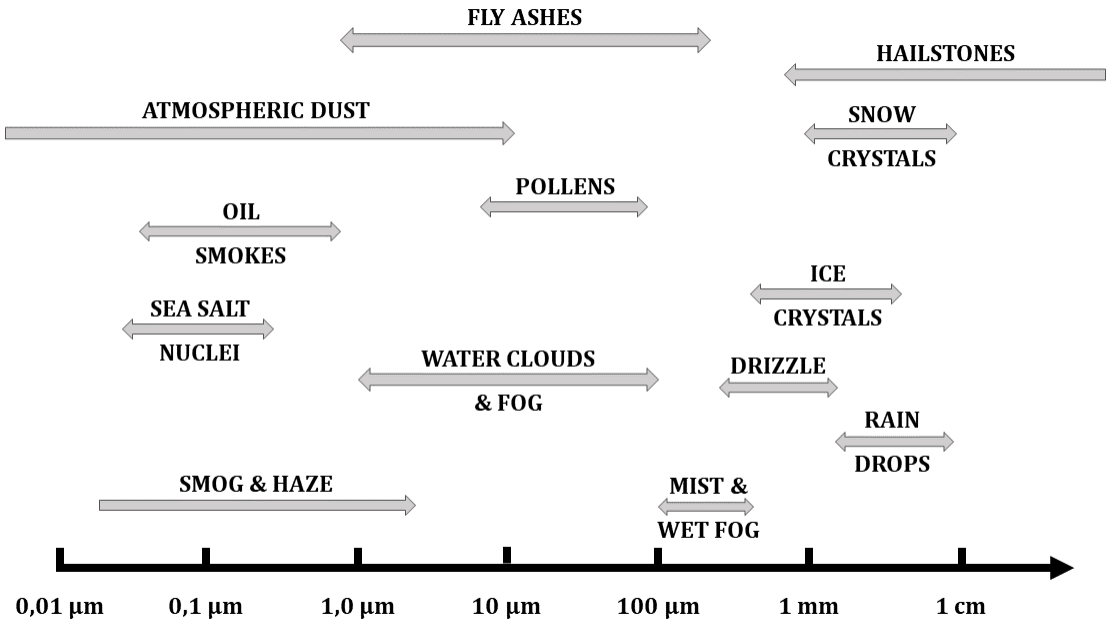

Figure 4.5: A classification of aerosols as a function of their size.

possible to localize clouds, aerosols and molecules.
From eq.4.6 one can estimate the expected number of photons detected in a time bin Δt

$$N(R, \lambda) = P(R, \lambda)\Delta t/hc \tag{4.11}$$

and by summing up the number of photons coming from different pulses in the same time bin, the aerosol profile can be built up. The acquired profile depends on the wavelength and on the distance from the emitter.
In order to investigate the presence of aerosols, two wavelengths are mainly used

- $\lambda = 532$ nm. At this wavelength the Rayleigh scattering due to N_2 molecules is strong and the so called *molecular signal* can be used as a reference to quantify the relative concentration of aerosols.

- $\lambda = 1064$ nm. At this wavelength Rayleigh contribution is attenuated as its power decreases as λ^{-4}. The advantage in using this wavelength is that one can reach longer distances avoiding the attenuation due to Rayleigh scattering.

An example of the difference between the signal at 532nm and the one at 1064nm is shown in Fig.4.6; the signal at λ=1064nm, even though its absolute intensity is lower, can be more clearly distinguished from the molecular signal and the result is a more defined and detailed structure.

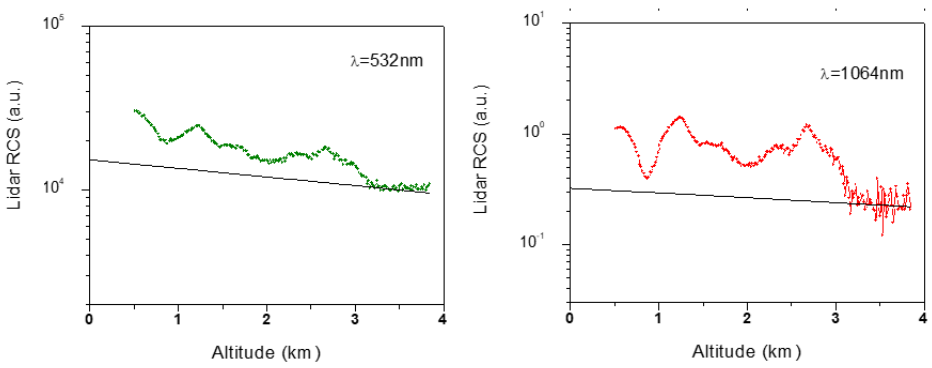

Figure 4.6: A comparison of aerosol signals at two different wavelength.

One could, in principle, move further in the infrared wavelength regime and use eye-safe lasers, enhancing also the maximum distance. This is not straightforward as a limit in the wavelength is setted by the detectors used in the receiver, whose signal to noise ratio (SNR) drastically drops in IR.
Superconducting Nanowire Single Photon Detectors (SNSPD) can provide high SNR also in the IR domain and lot of efforts in this work of thesis have been devoted to the realization of an elastic Lidar measurement with a SNSPD.
In [73] the authors measured the position of a 38km distant hard target with a Lidar at λ=1064nm and a NbN SNSPD. With the same system they studied the horizontal distribution of sea fog over a distance of 80km. With this result the authors demonstrate that the use of a SNSPD can appreciably increase the maximum reachable distance from about 20-30km to 80-90km.

4.3.1 Lidar ratio and depolarization ratio

Simple backscatter signal provides only the localization and the extension of the target. Measurements of the optical parameters such as backscattering and extinction coefficients and of their spectral dependence are needed to gain more information. Among the parameters useful for a characterization of the target, one can analyse lidar ratio and the depolarization ratio.
Lidar ratio is defined as extinction to backscatter coefficients ratio at a fixed wavelength

$$S(\lambda) = \alpha(\lambda)/\beta(\lambda) \tag{4.12}$$

and it depends on target's refractive index and size. The extinction and backscatter coefficients can be simultaneously measured by an elastic/Raman lidar [113].

An analysis of the signal's polarization can provide further information about the shape of the particles ([114, 115]). Indeed, the radiation emitted by the laser is polarized and the backscatter signal can be separated trough a beam splitter in parallel (P-channel) and

Table 4.1: Lidar ratios and depolarization ratios for different species as measured in [14]

Particle	**S(λ) [sr]**	$\delta(\lambda)$ **[%]**
Marine salt	10 - 30	0 - 5
Burning biomass	35 - 50	8 - 12
Pollution	45 - 60	0 - 5
Smoke	45 - 100	0 - 5
Dust	40 - 100	15 - 25
Volcanic ash	50 - 60	35 - 40

perpendicular (S-channel) polarized signals. The depolarization ratio Δ is defined as the ratio of the return signal in perpendicular to parallel polarization relative to the emitted laser light, as given by the following equation:

$$\Delta = P_{\perp}/P_{\parallel} \tag{4.13}$$

which reduces to

$$\delta = \beta_{\perp}/\beta_{\parallel} \tag{4.14}$$

in the assumption that only the backscatter coefficient values is sensitive to the polarization.

The value of δ is bigger if the scattering particles suspended in the atmosphere are not

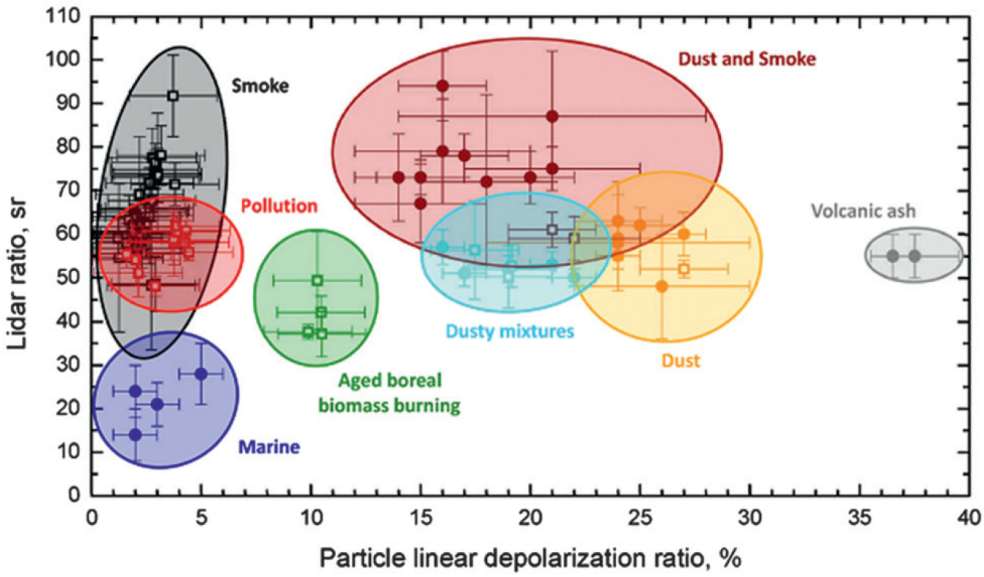

Figure 4.7: Aerosols classification according with depolarization ratio and Lidar ratio values [12].

spherical, as in the case of dusts, ice crystals, marine salt, crystallized nitric acids etc.

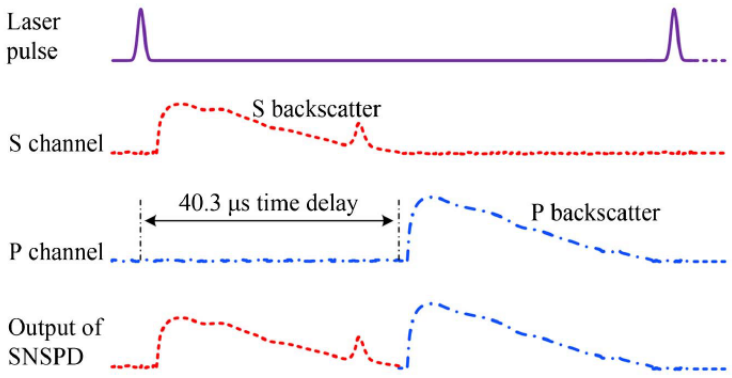

Figure 4.8: Scheme of a polarization lidar with SNSPD at 1550nm as presented in [13].

In Tab.4.1, a collection of data shows how a combined analysis of $S(\lambda)$ and $\delta(\lambda)$ permits the identification of the target species ([14]).
A clear picture of aerosols identification based on lidar and depolarization ratios is presented in Fig.4.7.
A measurement of depolarization ratio with a λ=1550nm Lidar and an SNSPD was demonstrated in [13]. In this work the signal is injected in a single mode fiber and the two polarizations are separated trough a in-fiber PBS (polarization beam splitter); they introduce a time delay module (TDM) on the P-channel with the use of a piece of fiber and, in this way, they can use just one detector and no calibration between the two signals is required. A scheme of the acquisition is presented in Fig.4.8. The advantage in the use of the SNSPD consists here in the use of an eye-safe wavelength which also reduce the molecular Rayleigh scattering.

4.4 Raman Lidar

Lidar technique based on elastic scattering is generally applied to the study of atmospheric aerosols and clouds. Raman lidar, based on the weak inelastic scattering, is mainly used to determine the values of α and β parameters but it can be used also for the measurement of the concentration of specific atmospheric molecules, such as water vapour, nitrogen and ozone and to investigate the atmospheric temperature profile [116, 117].
Raman lidar working principle is based on the excitation of molecules vibrational and rotational levels which causes a shift in the wavelength; one refers to Stokes process when the light is red-shifted and to anti-Stokes when it is blue-shifted. The energetic shift depends on the molecule species and on the temperature, as the energetic levels' population follows Boltzmann distribution.
The low value of the cross section of Raman process involves a low signal to noise ratio and typically this type of measurement cannot be operated during daytime. Furthermore, the

dependence of the Raman cross-section on λ^{-4} justifies the fact that this technique makes mainly use of UV light. In the case of Raman technique, the lidar equation can be rewritten as

$$P_R(\lambda_R, R) = \frac{K_R O(R)}{R^2} \beta_R(\lambda_R, R) \exp\left[-\int_0^R (\alpha_0(, \lambda_0, R') + \alpha_R(\lambda_R, R'))\, dR'\right] \tag{4.15}$$

and the extinction coefficient is different on the two ways as the wavelength λ_R on the way back is shifted. The backscatter coefficient β_R depends on the molecule number density N_R of the Raman-active gas and the cross section of Raman process.

Water vapour mixing ratio

The Raman technique can be used for gas concentration measurements as water vapour mixing ratio $\chi_{H_2O}(R)$, defined as

$$\chi_{H_2O}(R) = \frac{n_{H_2O}(R)}{n(R)} \tag{4.16}$$

where $n_{H_2O}(R)$ and $n(R)$ are, respectively, water vapour and atmosphere number density as a function of the altitude R. In order to determine $\chi_{H_2O}(R)$ one can use the nitrogen molecules concentration in the atmosphere which is stable in time up to 100km [15]. Indeed the nitrogen molecule mixing ratio is approximately constant and its value is

$$\chi_{N_2}(R) = \frac{n_{N_2}(R)}{n(R)} = 0,78 \tag{4.17}$$

where $n_{N_2}(R)$ is molecular nitrogen number density.
From a comparison of equations 4.16 and 4.17 one can see that the water vapour mixing ratio can be determined from n_{N_2} and $n_{H_2O}(R)$ according with the equation

$$\chi_{H_2O}(R) = 0,78 \frac{n_{H_2O}(R)}{n_{N_2}(R)} \tag{4.18}$$

and the two number densities can be estimated with simultaneous measurements of the Raman lidar signals at two different wavelengths. The calculation of the signal ratio P_{H_2O}/P_{N_2} permits the determination of the mixing ratio

$$\chi_{H_2O}(R) = C \frac{P_{H_2O}(R) \exp\left[-\int_0^R \alpha_R(\lambda_{N_2}, R') dR'\right]}{P_{N_2}(R) \exp\left[-\int_0^R \alpha_R(\lambda_{H_2O}, R') dR'\right]} \tag{4.19}$$

which is an indicator of the relative concentration of the two gases. The constant C, called calibration constant, accounts for the differences in the two backscatter coefficients. In case of absence of aerosols, one can calculate the transmission coefficients in square brackets

from atmospheric models. Raman cross section, which differs from the two species and the wavelength, is hidden in th β coefficients of eq.4.19 trough expressions 4.2 and 4.1. Fortunately the cross section ratio $\sigma_{N_2}/\sigma_{H_2O}$ has been measured in [118] and its value is about $0.4\pm10\%$. Hence, a measurement of the signals in eq.4.19 provides an indirect measurements of water vapour and molecular nitrogen number densities and one can obtain the mixing ratio.
This kind of measurement can be extended to other molecules species.

Calculation of extinction and backscatter coefficients α and β

As shown in Fig.4.7 the values of Lidar ratio and depolarization ratio are required in order to identify the aerosol. In [119] and inversion method to calculate the lidar ratio $S = \alpha/\beta$ by the elastic signals is presented. However, also the optical parameters α and β, unknown parameters in lidar equation, contain important information about the number of particles, their shape and size. There are computational inversion models that, under certain assumptions, give an estimation of their altitude profiles.
Trough Raman lidar signals analysis it is possible to calculate aerosol extinction coefficient profile and, in combination with elastic signal analysis, the backscatter coefficient profile.

In [120] a method to calculate the extinction coefficient α is presented. This method is based on the fact that Raman molecular signals are affected by the aerosol extinction coefficients α_{aer} because the backscatter radiation is attenuated by the transmission term, but not by aerosol backscatter coefficient β_{aer} because it generates a signal of unchanged wavelength which is blocked when the shifted Raman signal is collected.
As reported before, Raman lidar equation is

$$P(R,\lambda_L,\lambda_R) = P_0 A \eta \frac{c\tau}{2}\frac{O(R)}{R^2}\beta_R(R,\lambda_L,\lambda_R)\exp\left\{-2\int_0^R [\alpha(R',\lambda_L)+\alpha(R',\lambda_R)]\,dR'\right\} \tag{4.20}$$

where the dependence on laser wavelength λ_L and Raman shifted wavelength λ_R is explicitly stressed. The backscatter coefficient β depends on the altitude R just trough the term $N(R)$ as shown in eq.4.2; hence, the derivative of the logarithm of eq.4.20 provides the following expression for the extinction coefficients

$$\alpha(R,\lambda_L)+\alpha(R,\lambda_R) = \frac{d}{dR}\left[\frac{O(R)N(R)}{R^2P(R)}\right] \tag{4.21}$$

where the cross section was omitted because it is just a multiplicative term and the number density $N(R)$ is well known if one considers the signal coming from N_2 or O_2; the overlap function $O(R)$ equals one after the altitude R_{min} is passed.
The two extinction coefficients in eq.4.21 can be written as the combination of aerosol and molecular contributions

$$\alpha(R,\lambda) = \alpha_{mol}(R,\lambda)+\alpha_{aer}(R,\lambda) \tag{4.22}$$

and eq.4.21 becomes

$$\alpha_{aer}(R,\lambda_L)+\alpha_{aer}(R,\lambda_R)=\frac{d}{dR}\left[\frac{O(R)N(R)}{R^2P(R)}\right]-\alpha_{mol}(R,\lambda_L)-\alpha_{mol}(R,\lambda_R) \tag{4.23}$$

where α_{mol} are known quantities. One assumption is required at this point, that is the dependence of α_{aer} on the wavelength. If one assumes $\alpha_{aer}(R,\lambda_L)/\alpha_{aer}(R,\lambda_R)=\lambda_R/\lambda_L$ the aerosol extinction coefficient can be calculated from Raman signal trough the formula

$$\alpha_{aer}(R,\lambda_L)=\frac{\frac{d}{dR}\left[\frac{O(R)N(R)}{R^2P(R)}\right]-\alpha_{mol}(R,\lambda_L)-\alpha_{mol}(R,\lambda_R)}{1+\frac{\lambda_L}{\lambda_R}}. \tag{4.24}$$

As mentioned at the beginning of this paragraph, a combined Raman and elastic lidar signals analysis also provides a way to calculate the aerosol backscatter coefficient. The method is described in [113] and elastic and inelastic signals $P_{\lambda_L}(z)$ and $P_{\lambda_R}(R)$ are required. A combination of eq.4.6 and eq.4.15 written for R and for a reference altitude R_0 leads to

$$\begin{aligned}\beta_{aer}(\lambda_L,R)=-\beta_{mol}(\lambda_L,R)+[\beta_{aer}(\lambda_L,R_0)+\beta_{mol}(\lambda_L,R_0)]\times\\ \times\frac{P(\lambda_R,R_0)P(\lambda_L,R)N_R(R)}{P(\lambda_L,R_0)P(\lambda_R,R)N_R(R_0)}\times\\ \times\frac{\exp\left\{-\int_{R_0}^{R}\left[\alpha_{aer}(\lambda_R,R')+\alpha_{mol}(\lambda_R,R')\right]dR'\right\}}{\exp\left\{-\int_{R_0}^{R}\left[\alpha_{aer}(\lambda_L,R')+\alpha_{mol}(\lambda_L,R')\right]dR'\right\}}.\end{aligned} \tag{4.25}$$

The reference height R_0 is often chosen such that $\beta_{mol}(\lambda_L,R_0)\ll\beta_{aer}(\lambda_L,R_0)$ to neglect the unknown term and obtain $\beta_{aer}(\lambda_L,R_0)+\beta_{mol}(\lambda_L,R_0)\approx\beta_{mol}(\lambda_L,R_0)$; when this condition is not satisfied it is not possible to calculate $\beta_{aer}(\lambda_L,R)$. The other terms in eq.4.25 are all known, except the aerosol extinction coefficient which can be calculated with the method described above.

Temperature profiling with Raman Lidar

The possibility of measuring atmospheric temperature by using the rotational Raman spectrum of N_2 and O_2 molecules is guaranteed by the fact that the population of excited levels depends on the temperature trough Boltzmann distribution. As explained in [121], the intensity $I(J,T)$ of the radiation emitted by the excited molecules is given by

$$I(J,T)=I_0\nu_J^4 g_I\frac{BN_0}{k_BT}(2J+1)S(J)\exp\left[-\frac{B}{k_BT}J(J+1)\right] \tag{4.26}$$

where I_0 is the intensity of the incident radiation, ν_J the frequency of the emitted radiation, g_I the statistical weight of nuclei spin, B is the rotational constant and

$$\begin{cases}(2J+1)S(J)=\dfrac{(J+1)(J+2)}{(2J+3)} & Stokes\\ (2J+1)S(J)=\dfrac{J(J-1)}{(2J-1)} & anti-Stokes\end{cases} \tag{4.27}$$

Table 4.2: Values of α and β Raman parameters.

Gas species	α **[K]**	β
N_2	418.924	-0.7034
O_2	732.667	-1.9041
Air	477.172	-0.5921

Here J is the quantum number of the initial state of a molecule which obeys the selection rules $\Delta J = \pm 2$.
If one now considers the ratio of the intensities of two different lines, the temperature dependence can be expressed by the formula

$$R = \frac{I(J_1, T)}{I(J_2, T)} = \exp\left(\frac{\alpha}{T} + \beta\right) \tag{4.28}$$

where the coefficients $\alpha = [E_{rot}(J_2) - E_{rot}(J_1)]/k_B$ and $\beta = \ln S(J_1) - \ln S(J_2)$ have been introduced. In order to reduce the losses in the backscattered signal, the sum of lines generated from both O_2 and N_2 are considered and eq.4.28 becomes

$$R_\Sigma = \frac{I_{N_2}(J_{N_2,1}) + I_{O_2}(J_{O_2,1})}{I_{N_2}(J_{N_2,2}) + I_{O_2}(J_{O_2,2})} = \cong \exp\left(\frac{\alpha_\Sigma}{T} + \beta_\Sigma\right) \tag{4.29}$$

and α_Σ and β_Σ are calculated from the average values of $E_{rot}(J_i)$ and $\ln S(J_i)$.
Hence, the ratio of Raman signals referring to different lines calculated for different time bins (i.e. altitudes) provides the temperature profile.
The values of α and β for N_2, O_2 and air are listed in Tab.4.2.

The choice of wavelength depends on Raman rotational energies and the most used are visible (VIS) and ultraviolet (UV) sources. In [117] the authors compare visible (λ=532nm) and UV (λ=355nm) results and claim that the use of UV light open the way to daytime measurements due to reduced sky background. Moreover, this spectral region is safer in terms of hazard for eye injury, with retinal damage threshold being more than 3 orders of magnitude lower than in the visible. The signal likelihood is almost unaffected by the change of wavelength.

4.5 Doppler Wind Lidar

The knowledge of wind speed and direction at different altitudes is fundamental in order to validate atmosphere and aerosols dynamics models.
The change of frequency of a wave when the source or the receiver move relative to one another is a well-known phenomenon, called Doppler effect. This effect affects sound waves as well as electromagnetic waves and in the latter case one can write

$$\frac{\Delta f}{f} \propto \frac{v}{c} \tag{4.30}$$

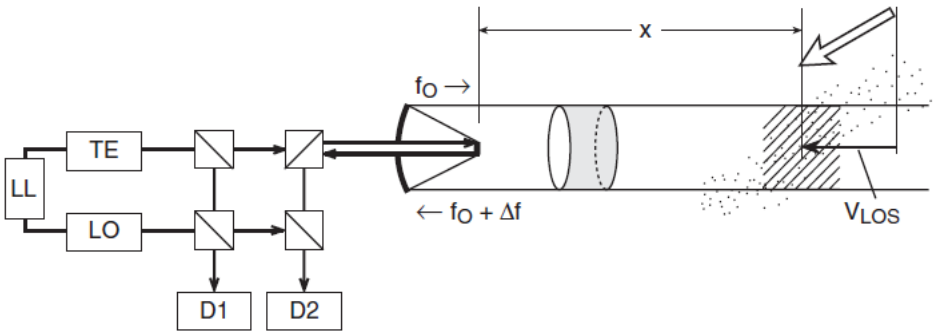

Figure 4.9: Heterodyne detection in coherent wind lidar.

where Δf is the frequency shift, f is the source wavelength frequency, v is the source (or receiver) speed and c is the speed of light.
Doppler effect is widely used to measure stars'velocity and it can be used also to measure wind speed velocity, if the molecules in the atmosphere can emit radiation. This can be done by mean of a lidar system because the backscattered light can be seen as the radiation emitted by a moving source.
The movement of air masses is an overlap between wind velocity and thermal motion; the latter leads to higher velocity for lighter particles hence the spectral distribution of the backscatter radiation will be broader. For heavier particles, as aerosols, the velocity due to thermal motion is lower and the spectral distribution becomes sharper.
In order to reduce the molecular contribution, which leads to a broadening in the spectral distribution, a λ=1550nm source is typically used. Indeed, as discussed before, the molecular scattering is related with Rayleigh cross section which depends on λ^{-4} and is negligible at this wavelength. On the other hand, aerosols contribution depends on λ^{-2} - λ^{+1} and it's still observable also in that spectral range.
The shifted signal is very low and the frequency shift is narrow; hence the signal cannot be discriminated by mean of a filter and the heterodyne detection (HD) technique is often used. In HD wind lidar, the signal is combined with a local oscillator (LO) beam, which has the same frequency of the source f_0, a very precise pulsed laser (TE). A scheme of HD wind lidar is shown in Fig.4.9. The local oscillator and the laser source are synchronized and the signal contains the interference terms due to the sum and difference of the LO and the shifted signal frequencies, $f_{LO} \pm (f_0 + \Delta f)$, resulting in a detector current

$$i_{AC} = \eta\sqrt{2P_{LO}P(\lambda, R)}\,\{\cos[2\pi(f_{LO} - (f_0 + \Delta f))] + \cos[2\pi(f_{LO} + (f_0 + \Delta f))]\} \qquad (4.31)$$

where η is the detector efficiency, P_{LO} the power of the local oscillator, $P(\lambda, R)$ the power of the backscattered radiation, f_{LO} and f_0 the local oscillator and laser source frequencies, respectively. There is also a direct current contribution coming from the unshifted signal.
In eq.4.31, the contribution coming from the sum signal $f_{LO} + (f_0 + \Delta f)$, has a frequency

which is higher than the detector and electronics cut-off while the difference $f_{LO} - (f_0 + \Delta f)$ can be detected with high accuracy.
The coherent Doppler lidar uses two detectors: on D1 the LO frequency is mixed with f_0, on D2 the LO frequency is mixed with the backscattered signal. The two detectors are then connected and the output signal is the difference between S1 and S2. With this method both the detector noise and the direct current term named above are eliminated and just the shifted signal survives.
The output signal is then directed to a spectral analyser and the frequency shift and the velocity can be calculated.
The advantage in the use of heterodyne wind lidar is the low noise, achieved with the double detectors combination. With the exposed technique it is possible to measure only the horizontal (parallel with the telescope axis) wind velocity, but with more complicated systems, based on the same working principle, more accurate information on other directions can be obtained.
In [74], the authors measured wind speed through a wind lidar and an SNSPD. The system was a double-edge wind lidar which makes use of two wavelengths but the operating principle is the same as the one described above. The use of SNSPD instead of the InGaAs APD, leads to two advantages: detector noise is low and just one detector is required, the efficiency is high also at 1550nm [49] and signal current intensity is higher.

4.6 Differential-absorption Lidar (DIAL)

Differential absorption lidar (DIAL) is a remote sensing technique used to obtain the profiles of atmospheric molecules as water vapour H_2O, ozone O_3, sulphur dioxide SO_2, nitrogen dioxide NO_2, carbon dioxide CO_2 and others. This technique is based on the strong dependence of the molecular absorption spectrum on the wavelength. A DIAL lidar requires indeed two wavelengths, one tuned to a strong absorption by the molecule of interest λ_{on}, and the other tuned to a nearby wavelength with weak absorption by the gas λ_{off}. If the two wavelengths are close enough, it is reasonable to accept the assumption $\beta(\lambda_{on}) \sim \beta(\lambda_{off})$. In this case, only the absorption coefficient α will be affected by the wavelength shift $\Delta\lambda$ and the measured signals ratio will be

$$\frac{P_{on}}{P_{off}} = \exp\left\{-2\left[\alpha(R', \lambda_{on}) - \alpha(R', \lambda_{off})dR'\right]\right\}. \tag{4.32}$$

Then, if $\Delta\sigma$ is the shift in the absorption cross section, the number N of scattering centres is

$$\Delta\alpha = N\Delta\sigma \tag{4.33}$$

and it can be calculated with extreme precision from the signals ratio

$$N = \frac{1}{2\Delta\sigma}\left[\frac{d}{dR}\ln\left(\frac{P_{on}}{P_{off}}\right)\right]. \tag{4.34}$$

Molecule	Wavelength [μm]	k [$atm^{-1}cm^{-1}$]
H_2O	0,69	0,00035
O_3	0,29	12
SO_2	0,30	26
NO_2	0,45	7,2
CO_2	2,05	0,09

Table 4.3: DIAL coefficients of different molecules [15, 16]

This formula represents the theoretical molecular number density, calculated in the limit of continuous acquisition. In practice, the backscattered photons are counted in time bins Δt and a similar formula can be written for the discrete case [122]. The time bins'size sets the spatial resolution and the lower limit is related to $\Delta\sigma$.
By means of a DIAL one can easily determine the molecular number density from the acquired signals P_{on} and P_{off} but it is mandatory to have two high precision tunable lasers which can be be transmitted in the atmosphere simultaneously or, similarly, a single laser source able to emit two different pulses with a fast switching time.
An important parameter for the DIAL lidar is the DIAL coefficient k as it is commonly used to indicate the picks in the absorption spectra; it depends on the cross section as follows

$$k = 2,55 \times 10^{19}\sigma; \tag{4.35}$$

some values are reported in Tab.4.6.

4.7 Detectors for Lidar

Photodetectors or light sensors can be divided by their operating principle in two categories: photoelectric and thermal effect detectors.
In thermal effect detectors the heat produced by the incident light is converted in charges as well as electromotive force or conductivity.
The photoelectric effect is a phenomenon in which, when the light strikes a metal or a semiconductor placed in the vacuum, an electron is emitted. The electrons'number is amplified and a photocurrent is measured. Photoelectric conversion is classified into external and inner photoelectric effect. In the former, electrons are emitted from the photocatode in the vacuum chamber, in the latter, which also refers to photovoltaic effect, a photon generates a electron-hole pair and the excited photoelectrons remain into the conduction band of a material.
Photomultiplier tubes (PMT) and avalanche photodiodes (APD) are single photon detectors that are able to count single photons using, respectively, the external and inner photoelectric effect. These two families of sensors are widely used in lidar systems because they can provide a good signal to noise ratio (SNR) also in the case of weak signal.
The critical performance parameters of a detector are:

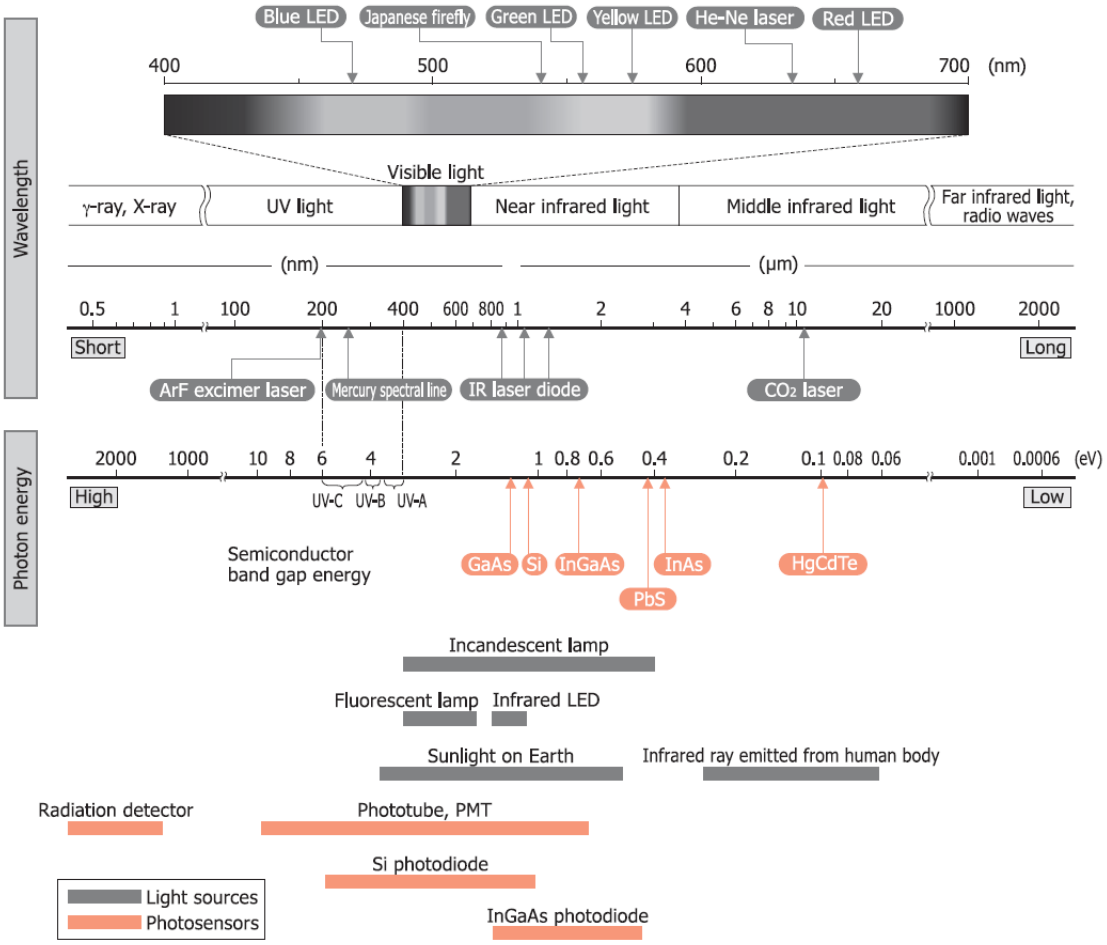

Figure 4.10: Conventional detectors and light sources classification.

- the *spectral responsivity*, measured in A/W, is a ratio of the generated photocurrent to incident light power, which is related with a wavelength dependent parameter, the *quantum efficiency* that is the number of detected photons over the incident photons;
- the *dark current* which accounts for the signal due to the background and the device in absence of incident light;
- the *noise equivalent power* (NEP) which sets the minimum incident power that can produce a signal distinguishable from the noise;
- the *response time* which is the time interval between the photon absorption and the signal emission;
- the *dead time* that also sets the limit to the maximum counting rate.

A wide set of materials and geometries can be chosen to achieve different performances and optimize the detector accordingly with the applications. In Fig.4.7 a scheme of sensors and light sources, provided by Hamamatsu, describes the wavelengths covered and the energy gaps.
In this section the working principles of PMT and APD are described as they are the most used detectors in Lidar systems. Next chapter will be devoted to the description of an SNSPD based lidar measurement and a comparison with conventional detectors is provided.

Photo Multiplier Tubes (PMT)

As shown in Fig.4.11, a photomultiplier tube (PMT) consists of a vacuum chamber with an optical window, a photocathode, focusing electrodes, electron multipliers and an anode.
The working principle is based on external photoelectric effect, the emission of a conduction electron from a metal or a semiconductor when photons hit the material. This phenomenon just occurs when the photon energy passes a threshold level setted by the material extraction potential, the work function. The kinetic energy of the emitted electron is given by

$$K_e = h\nu - U_0 \tag{4.36}$$

where ν is the photon frequency, h the Planck constant and U_0 the work function. When the photons pass trough the input window, electrons in the photocathode are excited so that photoelectrons are emitted in the vacuum chamber. Then the focusing electrodes direct the photoelectrons on the first dynode where they are multiplied by secondary photoelectric effect. The multiplied secondary electrons are collected by the anode and the current is measured.

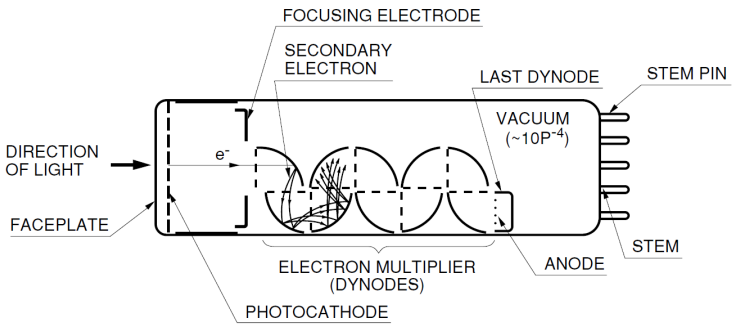

Figure 4.11: Photomultiplier tube.

Most photocathodes are compound materials which include semiconductors and alkali with a low work function which sets the detectable wavelength range. In tab.4.7 some example of photocathode materials and detectable wavelength are presented [123].
Also dynodes'material, mounting geometry and shape can affect the detector performances as quantum efficiency and dead time. A PMT quantum efficiency can range from about 40% in the case of UV light detection to 1% at 1400-1700 nm.

Material	Cs-I	Sb-Cs	Sb-Na-K-Cs	Ag-O-Cs	Ga-As	InP /InGaAs
λ **[nm]**	<200	UV-VIS	UV-900	300-1200	300-900	<1400-1700

Table 4.4: Photocathode materials and detectable wavelength

Avalanche Photodiodes (APD)

In an APD the photon absorption creates an electron-hole pair if the energy is higher than the semiconductor energy gap. The charge multiplication is obtained by applying a reverse high voltage across the semiconductor lattice rather than with the dynodes (see Fig.4.12) and it is more efficient when the detector is cooled. In details, the applied voltage forces the electrons to move towards the n side and holes towards the p side. During this drift, the carriers collide with the lattice and their velocity reaches a saturation value if the applied field is sufficiently high. Some carriers may eventually escape the collision with the lattice and, as a result, they will have a sufficiently high energy to generate another electron-hole pair. These additional carriers will also be accelerated and can create other pairs in a sort of chain reaction, called avalanche multiplication. The number of pairs produced in the time required by a carrier to cross a unit distance is called *ionization rate*. The gain of an APD is the average multiplication of each carrier. However, the ionization rate is not constant and its fluctuations is the origin of APD noise.

The spectral response depends on the sensitive area's material and structure. Indeed, shorter λ can produce a pair on the semiconductor surface while longer wavelengths can penetrate deeper. Different structures can enhance the detection at longer or shorter wavelengths and it is possible to reach also 85% efficiency in VIS but it drops down in the NIR [17].

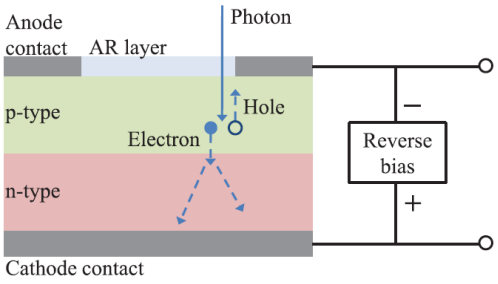

Figure 4.12: Single Photon Avalanche Photodiode.

Compared with a PMT, the APD provide higher efficiency; conversely, the APD dark count rate and response time are higher compared with a PMT.

Summary

In this chapter an overview of Lidar technique is provided. First Lidar setup is described and the main equation is derived. Then we focused on the scattering processes which occur in the atmosphere when a Lidar system is turned on.

We also described the main Lidar systems used for atmosphere monitoring, as elastic backscatter Lidar for aerosol detection, Raman lidar for temperature profiling, water vapour concentration and α and β parameters measurements, Doppler wind Lidar and DIAL Lidar, used

for wind profiles and molecule concentration measurements, respectively.
The last topic treated in this chapter is a description of the most used detectors, as photomultipliers and semiconductor avalanche photodiodes. In the next chapter we will describe the working principles of Superconducting Nanowire Single Photon Detectors (SNSPD), a class of detectors introduced recently which exhibit high efficiency, low dark counts and other interesting features, presented in Chap.2. Such characteristics promote them as good candidates to replace conventional sensor in lidar applications in the cases of low signals or infrared wavelength.

CHAPTER 5

LIDAR measurement with SNSPD in infrared wavelengths domain

Abstract: Lidar technique is widely used today to investigate the properties of specific molecules and aerosols in the atmosphere. Even though Lidar systems for the measurements of water vapour mixing ratio or wind speed have been largely tested and launched onto the market, new systems are being realized today to enlarge the application fields and the set of information which can be obtained with the use of this technique.
Among the mentioned improvements, the realization of IR Lidars would open the way to a better study of aerosols. This wavelengths indeed can reduce the signal due to Rayleigh scattering contribution and increase the maximum reachable distance, providing a better aerosol profile also in the case of low signal. Moreover, some molecules as carbon dioxide, which plays an important role in the global warming issue, have absorption lines in IR spectral region and a Lidar in the IR would open the way to the study of other molecules concentration.
Another advantage in the use of infrared laser sources is that the system would be eye-safe, allowing hence safe measurements of aerosols spatial distribution in urban areas and city centres.
The obstacles to be overcame are the difficulties in the realization of sources and detectors which can operate in the infrared. Till now it is possible to find on the market 1550nm sources (widely used for telecommunications) and CO_2 continuous lasers which can generate $2\mu m$ and $10\mu m$ light (see Fig.4.7) but they require additional work to obtain the short and powerful pulses needed for the Lidar. Conversely, it is not possible to use standard single photon detectors as APD and PMT for infrared applications because signal to noise ratio significantly drops as the quantum efficiency is less than 1% and dark counts rate is high.
SNSPD detectors, described in Chap. 1, have a good signal to noise ratio also in IR domain and their integration onto Lidar systems can definitely open the way to IR-Lidar analysis.
In this chapter we compare the performances of SNSPD in IR with other detectors and present two Lidar measurements with SNSPD at $\lambda > 1\mu m$. The first measurement is a

proof of principle demonstration in which we measured the distance of an hard target with a prototype Lidar at 1550 nm. The second measurement was performed with the multi-wavelength lidar system MALIA in Naples and we measured the temporal evolution of clouds at 1064nm.

5.1 Detector comparison in NIR

The improvement of single photon detection in the IR is an important issue not only for Lidar but also for telecommunication and quantum information. Companies provide single photon detectors which can detect low signals at $\lambda = 1550nm$ and in this chapter we want to compare SNSPD performances with semiconductor based devices.
In order to give a clear idea we report in Tab.5.1 the information about efficiency, dark counts, dead time and other parameter for different detectors. We also added the information about *transition edge sensors* (TES), another superconducting single photon detector, to give a comparison with other low temperature devices.

Detector	**Detection efficiency [%]**	**Dark counts [1/s]**	**Timing jitter [ns]**	**Max count rate [MHz]**
PMT	2@1550nm	10^5	0.3	10
InGaAs SPAD (gated)	10@1550nm	91	0.37	0.01
Hybrid PMT (PMT+APD)	30@1064nm	$3 \cdot 10^4$	0.2	200
Multiplexed INGaAs SPAD	33@1064nm	$160 \cdot 10^6$	0.133	10
Multiplexed INGaAs SPAD	2@1550nm	$160 \cdot 10^6$	0.133	0.3
Frequency up-conversion	8.8@1550nm	$13 \cdot 10^3$	0.4	10
TES	95@1550nm	3	100	0.1
SNSPD	93@1550nm	0.1	0.003	500

Table 5.1: Single photon detectors properties as listed in [4, 17, 18]

From the data in the table, one can see that SNSPD provide the best characteristics and can be considered as the most advanced single photon detector, specially for IR applications.

Indeed they provide the best SNR and the detection efficiency can be tuned on the wavelength [50]. It is also possible to increase the dynamics with photon number resolving (PNR) SNSPD [124, 125]. PNR SNSPD would reduce the acquisition time for Lidar systems.
In [126] the authors compare the results of a Lidar measurement at 1550nm performed with a SNSPD and a InGaAs/InP SPD. The results are that, after numerical correction, the signal obtained with InGaAs/InP SPD is comparable, even if lower, than the one obtained with SNSPD; in this work the high altitudes range, where the SNSPD would show the main advantages, is not explored but one can conclude that in case of high intensity signals SNSPD is not necessary. Anyway, the high detection efficiency, which can be pushed up to 93%, and the low DCR (<1cps) make this device unique and extremely attractive in the case of low signals applications (high altitudes Lidars or low density aerosols/molecules).

5.2 Proof of principle demonstration

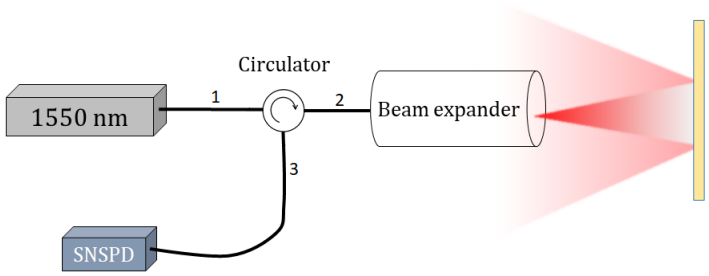

Figure 5.1: Lidar prototype scheme at 1550nm.

In order to prepare a Lidar measurement with a SNSPD detector, we first verified that the electronic setup, the acquisition programs and the measurement setup we realized could detect the backscattered light from an hard target. To do that, we realized a lidar prototype at 1550nm.
The measurement setup consists of a continuous laser ($P_0 = 37\mu W$) operating at 1550nm, a modulator, a circulator, a 20x beam expander (Thorlabs GBE20-C), also used as telescope, and the SNSPD. As one can see in Fig.5.1, the 1550nm laser is modulated and sent with a single mode fiber circulator in the 20x beam expander. The beam is then emitted towards the target and the backscattered light is partially collected back by the beam expander which is also used as a telescope. The anti reflection coating covers the wavelength 1050-1650nm and the fine focus handle guarantee that 1550nm photons are predominantly injected in the circulator single mode fiber. The collected photons reach the SNSPD through the third channel of the circulator.
The SNSPD is a NbTiN round meander with a $\oslash = 15\mu m$ diameter with a cavity which optimize the system detection efficiency value to 25% at 1550nm when cooled at 2,2K. The

device was realized at SIMIT[1]. The count rate and DCR are presented in Fig.1.13 and the dead time is about 90ns.
We modulated the beam to obtain a train of 10ns pulses with a repetition rate of 1kHz.
The preferred directions in the circulator are $1 \rightarrow 2$ and $2 \rightarrow 3$ but a small percent of the signal can also pass in the $1 \rightarrow 3$ channel. We used hence the detected pulses due to this low signal to identify the initial time t_0. In details, when the laser pulse is emitted, some photons directly arrive on the SNSPD and a pulse is measured, then, we measure the delay between the detected photons and t_0 and we calculate the distance of the hard target.
This measurement was repeated after changing the hard target position and the measured distance was in agreement with the results taken with a meter. The resulting signals are shown in Fig.5.2. We also rotated the beam expander and verified the angle dependence of

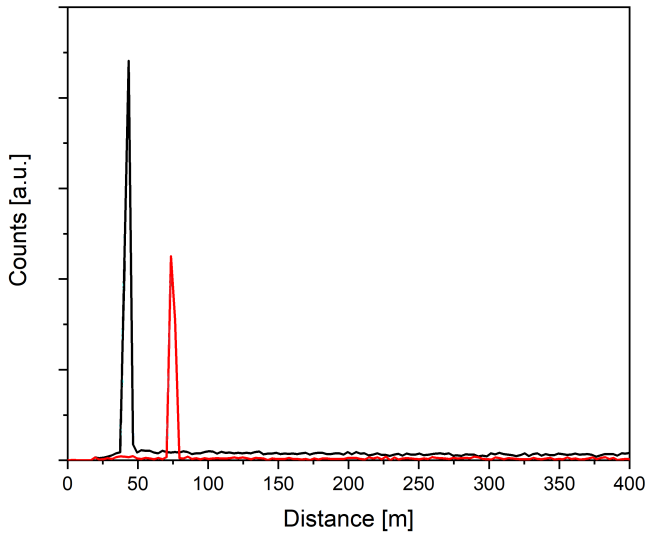

Figure 5.2: Lidar signal of an hard target located at two different distances measured with the prototype system at 1550nm.

the signal intensity.
Even though the laser power is low and the telescope diameter is small (56mm), the signal can be clearly distinguished from the background. As one can see from Fig.5.2, dark counts'contribution is neglectable and SNR is about 40.
With this result we demonstrated the feasibility of a Lidar measurement with the transportable setup assembled in our lab.

[1]Chinese Academy of Sciences, Shanghai, China

5.3 Cloud detection with MALIA system and SNSPD

Multi-wavelength Aerosol LIdar Apparatus is a lidar system operating in the Physics department of university of Naples Federico II, included in the European project EARLINET [127] (Lidar observation for European Aerosol Research Lidar Network). This system is devoted to the detection of aerosols and water vapour and it operates simultaneously at 1064nm, 532nm and 355nm wavelengths.
In order to improve the signal at 1064nm we integrated an SNSPD in MALIA setup with the support of *Advanced Lidar Applications S.r.l.*(ALA[2]). In this section we will first describe the lidar system, then the coupling with the SNSPD and, finally, we will present the results of a measurement.

MALIA measurement setup

The Lidar setup MALIA [128] operates at the fundamental wavelength of 1064nm emitted by a Nd:YAG lasers and its second and third harmonics, 532nm and 355nm. Laser pulses have a duration of 5ns and a repetition rate of 20Hz. Maximum pulses energy is 0.65 J at 1064nm, 0.15 J at 532nm and 0.1 J at 355nm and the beam divergence is 0.5mrad. The receiver is a Newtonian telescope with a focal length of 120cm and a diameter of 30cm and the acquired signal is separated by a series of dichroic mirrors in 11 channels, each one with a detector and readout electronic.
Besides the elastic signals, there are three channels to detect the Raman shifted signals due to the presence of nitrogen and water vapour; moreover, for $\lambda = 532$nm, parallel and perpendicular polarizations are separated.
In order to extend the system dynamic, elastic and Raman signals at 387nm need to be split in low/high range by a quartz plate. For low altitudes the receiving photomultiplier has a stronger attenuation in order to warrant a linear response while for high altitudes a smaller attenuation can be used. The non-linearity due to the dead time can be corrected through the formula $N = n/(1 - n\tau)$, where N is the expected count rate, n is the measured count rate, and τ is the detector dead time. The aim of dead time correction, is to warrant a linear working range for both near and far field channels (low/high), so that the two acquired signals can be normalized over a more extended range. The two signals are merged by software.
A detailed list of channels and detectors is presented in Tab.5.2 and the scheme of the entire setup is shown in Fig.5.3.

MALIA system has the capability to acquire aerosols and water vapour mixing ratio profiles.
The water vapour signal is obtained with the analysis of 407nm channel, that is the Raman shifted signal emitted by H_2O molecules excited at 355nm.
Water vapour mixing ratio is then obtained from the ratio of its number density to ambient

[2]ALA is a company that provides innovative solutions for remote sensing and air quality monitoring. It was born in 2012 and incorporated as spin-off company of University of Naples Federico II and CNR- the Italian National Research Council. Now it develops high quality LIDAR systems, sell all around the world.

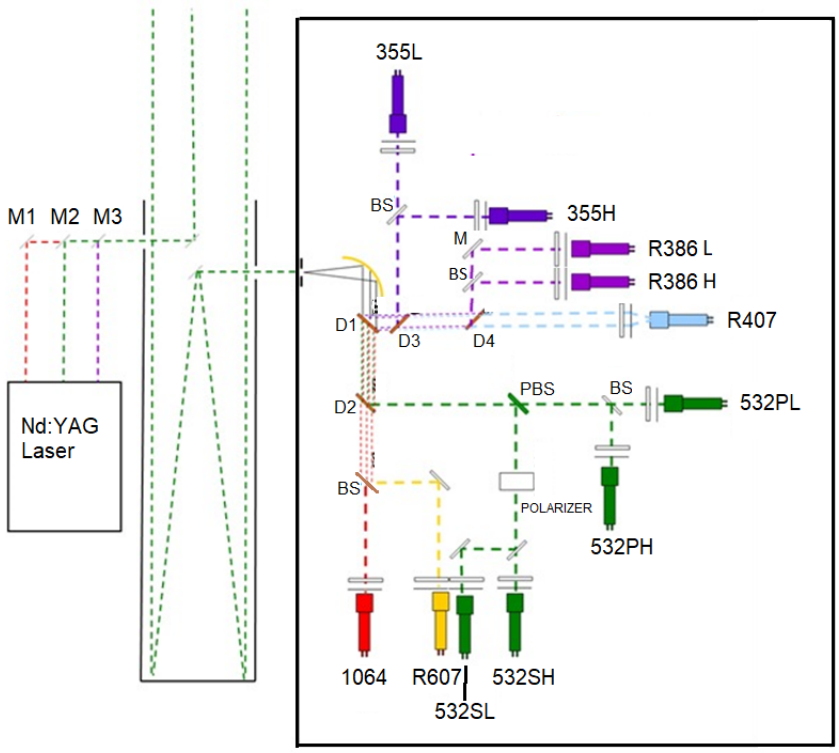

Figure 5.3: Experimental setup of MALIA system. A series of polarizer beam splitters (PBS) separates the parallel and perpendicular polarizations, the beam splitter (50/50 BS) divide the beam and a mirror (M) redirects the beam. A series of dichroic mirrors separates the wavelengths. D1 reflects (R) 407nm, 386nm, 355nm and transmits (T) 532nm, 607nm, 1064nm; D2 R 532nm, T 607nm, 1064nm; D3 R 355nm, T 386nm, 407nm; D4 R 386nm, T 407nm. Each detector (see Tab.5.2 for details) is equipped with an interferential filter.

air's number density. The Raman signal from N_2 can be used to determine the density of the ambient air since nitrogen represents a constant portion of dry air in the atmosphere. Hence from the simultaneous measurement of N_2 and H_2O Raman signals one can calculate the mixing ratio as described in Chap.4. The calibration constant C in eq.4.19 takes into account the differences both in the cross section of process for the two different species and in the acquisition setup for the two wavelengths (as detector efficiency). The determination of this constant is done by comparing the mixing ratio with the radio-sounding data[3].

The aerosols' analysis is performed in terms of backscattering, extinction coefficients and

[3]The radio-sounding is located in Pratica di Mare (RM), about 170km from Naples. It is not possible to place a sounding close to MALIA system because of the proximity with aircraft landing route for Naples International airport. Anyway, it is realistic to make the hypothesis that the water vapour concentration is uniform outside the PBL.

Wavelength [nm]	**Detector**	**Measured signal**	**Measurement mode**
355 (H)	Hamamatsu H6180	High altitude - elastic	Photon Counting
355 (L)	Electron Tubes 9202QB	Low altitude - elastic	Analog
386.7 (H)	Hamamatsu H6180	High altitude - Raman	Photon Counting
386.7 (L)	Electron Tubes PC25P	Low altitude - Raman	Photon Counting
407	Hamamatsu R1828	Raman	Photon Counting
532 (SH)	Hamamatsu H6180	High altitude - $\parallel$ polarization - elastic	Photon Counting
532 (SL)	Electron Tubes 9202QB	Low altitude - $\parallel$ polarization - elastic	Analog
532 (PH)	Hamamatsu H6180	High altitude - $\perp$ polarization - elastic	Photon Counting
532 (PL)	ElectronTubes 9202QB	Low altitude - $\perp$ polarization - elastic	Analog
607	Hamamatsu 7402-20	Raman	Photon Counting
1064	Licel Si APD	Elastic	Analog

Table 5.2: MALIA channels and detectors

polarization ratio vertical profiles [129]. According the Mie theory, the interaction with a spherical particle does not change the polarization state of the incident radiation. The more irregular is the shape of a particle, the more the changes in the polarization state. Therefore, lidar depolarization measurements provide information on shape and thermodynamic state of particles.
In order to measure the depolarization, a linearly polarized laser is used as transmitter and a polarizing beam splitter is used to split the perpendicular-polarized (P) component of the backscatter signal from the parallel-polarized (S) one. The calibrated ratio between the power measured for each channel provides the depolarization ratio.
There are more methods to obtain the depolarization ratio's calibration constant as the molecular technique, the orthogonal calibration method and the 45° rotation technique [130].

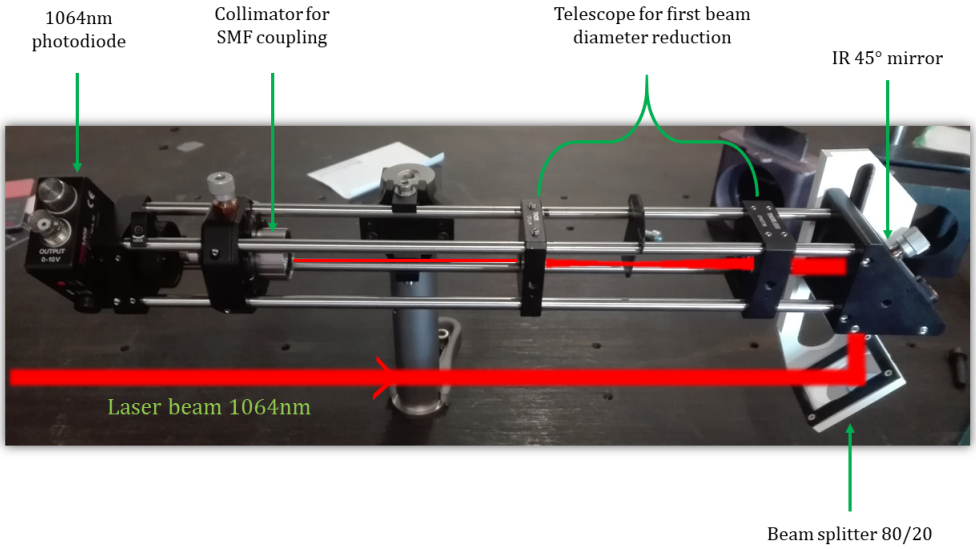

Figure 5.4: Cage system.

Optical coupling

The main problem in the integration of a SNSPD detector in MALIA measurement setup was to reduce the signal beam size from 1cm to single mode fiber's core (5 μm). The difficulty was due to the fact that the system is embedded in a small outdoor lab and it was not possible to modify the optics'disposition of fig.5.3 due to the reduced space. Looking in Fig.5.3, the system to reduce the beam diameter had to be designed to fit between the beam splitter (BS) and the 1064nm detector; this space is less than 3cm. The optical coupling system was designed and tested at the operational headquarters of ALA S.r.l.
In order to measure the signal in the 1064nm channel, we added a 20/80 beam splitter before the 1064 detector to redirect part of the beam along the vertical direction; this BS is united to a cage system (see Fig.5.4-5.6) where we placed a 1064nm mirror inclined at 45^o which is also equipped with two micro handlers to adjust the angle. On the cage we also placed two lenses with focal length 101.6mm and 25.4mm in order to reduce the beam diameter to one fourth. With this small telescope the beam size is acceptable for a single mode fiber collimator (Thorlabs, F810FC-1064) which can inject a beam of 8mm diameters in 5μm core single mode fiber. We realized the 20/80 BS holder with 3D printer to optimize its size with the optic system. On the cage system we also fixed a narrow band filter and attenuators, when required.
Before the mounting on Lidar optic system in Fig.5.3, we tested the cage on the optic desk in the lab. We did that specially to adjust the position of the lenses to avoid the movements in MALIA where the space is very limited.
In the lab we used a P=700mJ Nd:YAG pulsed laser which emits at λ=1064nm. With a BS we selected 10% of the beam and we placed a series of attenuators to further reduce the

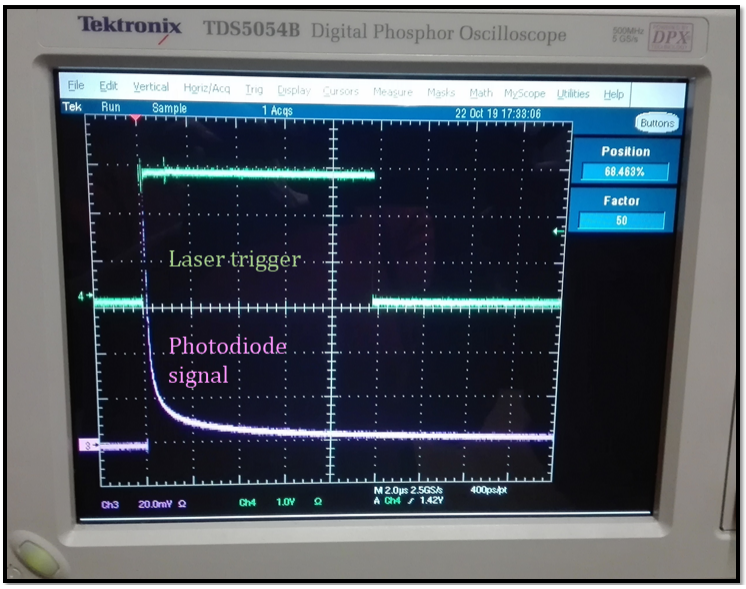

Figure 5.5: Cage system alignment verification with the oscilloscope.

beam power; with an adjustable mirror we directed the beam on the cage 20/80 BS. First, we adjusted the cage vertical and horizontal position to place the beam in the cage axis. Then, we centred the beam in the cage with the handlers on the two mirrors (one is the 45^o on the cage an the other is the one on the desk) and verified that it is parallel with the cage axis. We repeated these two step more times for fine adjustments.
The next step was to move the lenses in order to get a collimated and smaller beam. When we found the correct position we verified that the beam diameter remains unchanged for 3 meters. Then we placed the collimator and the single mode fiber which was coupled with a 1064nm sensitive avalanche photodiode (Thorlabs APD130C). We verified the alignment by connecting the laser trigger and the detector to an oscilloscope and verified that when the laser pulse is emitted (trigger on) we measure the photodiode response (see Fig.5.5).
Finally, we moved the cage inside MALIA optic system (see Fig.5.6). To verify the alignment we opened the telescope and used the sunlight first. The position of the lenses was fixed but we had to move the cage to place the beam in the centre of the BS. We did that with mechanical rotations and translations of the cage along the metallic holder. We also moved the 45^o mirror handlers. Then we turned on the laser but the backscattered signal at 1064nm was too low to be detected by the photodiode and we could not align simultaneously the cage system and Licel Si APD used in MALIA to detect the 1064nm elastic signal. Hence we postponed the last alignment part to the measurement with the SNSPD.

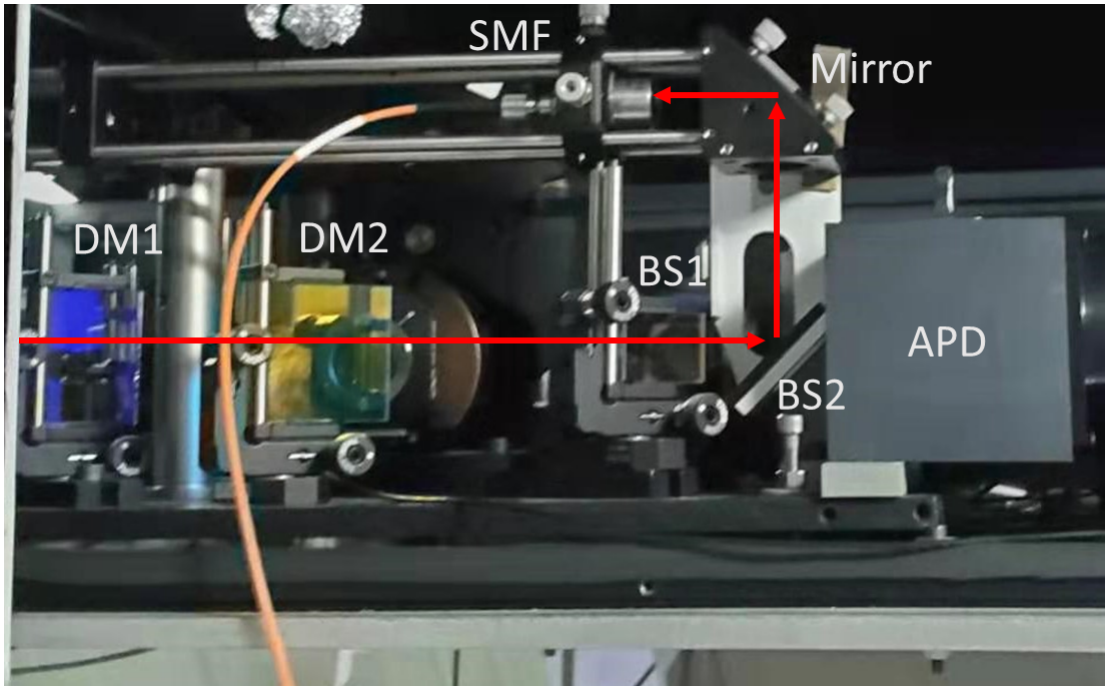

Figure 5.6: Integration of the cage system in MALIA setup. The red arrow represents the laser beam direction. BS1 and BS2 are, respectively, a 50/50 and 20/80 beam splitters.

Test measurement with NbTiN SNSPD

We cooled a NbTiN SNSPD at T=4.2 K and we measured the IV curve, the dark counts and the count rate at 1064nm. As shown in Fig.5.7, the critical current is $9.85\mu A$ and at $I_b \sim 7\mu A$ the count rate enters the saturation zone and the dark count rate is approximately 1cps. Hence we choose $I_b = 7\mu A$ as working point.
At this point we completed the alignment by moving the handlers on the two mirrors (the one in the cage and the other on the emitter beam in Fig.5.3). Then we fixed the SNSPD bias current though the bias tee as explained in chapter 2 and we acquired the signal for two minutes in daytime. The laser trigger is used to identify the initial time and the altitude $h = 0$.

During the first measurement we verified that the signal due to backscattered light is distinguishable from the background noise. In order to do that, we measured the delay between the trigger and the pulses when the laser is on and when it is stopped. The result is shown in Fig.5.8. The red light represents the measurement when the laser is turned on; the first peak is due to secondary reflections of the laser beam while we can clearly identify a cloud between 250 and 500m. The black line is the signal acquired when the laser is stopped, i.e. the background. From this measurement we deduce that the signal is ten times larger than the background and, hence, clearly distinguishable.

Then, we followed the cloud evolution in time within 5 minutes acquisitions and the results

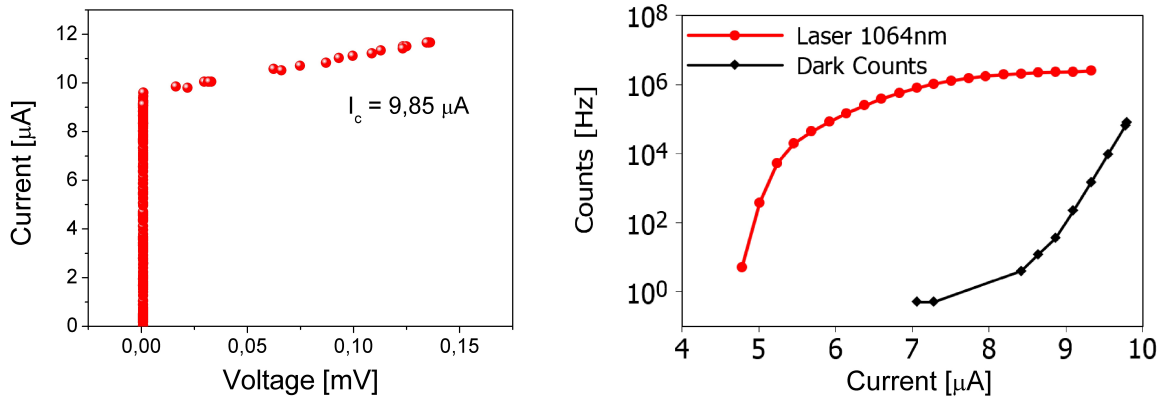

Figure 5.7: IV curve, dark counts and count rate at 1064nm.

are shown in Fig.5.9. It is also possible to notice a smaller structure at 1,3km.
Finally, we tried to measure more distant objects but the presence of a low altitude cloud shielded the photons coming from farther objects. The results are shown in Fig.5.10.
Hence, we can conclude that we successfully integrated the SNSPD in MALIA lidar system. Anyway, we could not align simultaneously the SNSPD and the APD and we could not compare the two signals. Indeed, the reduced space in the optical acquisition system impeded to modify the 20/80 beam splitter orientation and position.
Moreover, due to weather condition we could not explore longer distance's signals and we could not quantify the advantage in the use of a detector with a considerably higher SNR.

5.4 Design of aerosol Lidar in China

Part of this PhD program was spent in China, at BRIT, Beijing Research Institute of Telemetry (Beijing, PRC). The optics department works at the realization of innovative Lidar systems for aerosol, atmosphere profiles, wind speed measurements. During my staying in China I participated at two measurements campaigns organized by BRIT at *Chinese Meteorological Administration* (CMA, Beijing) and at Wuhan University (Aerospace Department).
During this period I worked to combine the SNSPD and the Lidar systems; in details, I worked to make the SNSPD as portable as possible. For the bias I realized a portable bias current generator (Fig. 2.10), I worked at the acquisition programs and adapted them to work with the electronic broads included in the lidar.
The lidar systems provided by BRIT, compared with MALIA, has the advantage that the signal was already injected in the fiber and the optical coupling was straightforward.

During the measurement campaign at CMA I tested the transportable setup and the bias box and tried to measure the aerosol content with a 1064nm lidar, a NbN SNSPD and

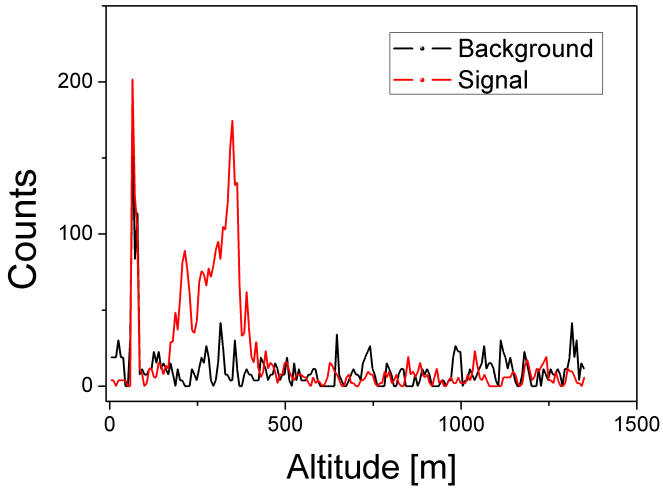

Figure 5.8: Red line represents the signal obtained at 1064nm during two minutes of acquisition. Black line is the signal obtained when the laser beam is stopped (trigger on).

the cryogenic insert that I designed and assembled (Fig.2.12), immersed in liquid helium. Unfortunately the measurement was not complete because the signal was too strong and the SNSPD could not return in the superconducting state and it was not possible to add attenuators to the compact Lidar system in short time.

During the time spent with BRIT campaign at Wuhan University I worked mainly at the design and the realization of a Lidar system for aerosol measurements at $\lambda = 1064nm$ and $\lambda = 1550nm$ with SNSPD.
The setup is a elastic Lidar whose telescope is connected to a collimator which injects the signal in a multimode fiber. The laser source can be changed easily and the collimator focus adjusted, according with the wavelength. Between the collimator and the telescope it is possible to place a filter and three attenuation levels.

For the measurement at $\lambda = 1064nm$, the collimator is connected to a in-fiber beam splitter (90/10 TM200R2F1B or 50/50 TM200R5F1B) which splits the signal to the SNSPD and to a standard PMT[4] (see Fig.5.11).
This setup was realized to compare the performances of a standard PMT and an SNSPD in aerosol profiles measurements with 1064nm elastic lidar.
The same setup can be used also for aerosol profile measurements at 1550nm. The signal reaching the collimator is directed, via single/multi-mode fiber, to the SNSPD. In this case it is not possible to compare the result with a standard detector as the SNR at $\lambda = 1550nm$

[4]The PMT is Excelitas SPCM CD, with 1.8-3% photon detection efficiency at 1064nm, 24-40nm dead time, 250-1500Hz DCR.

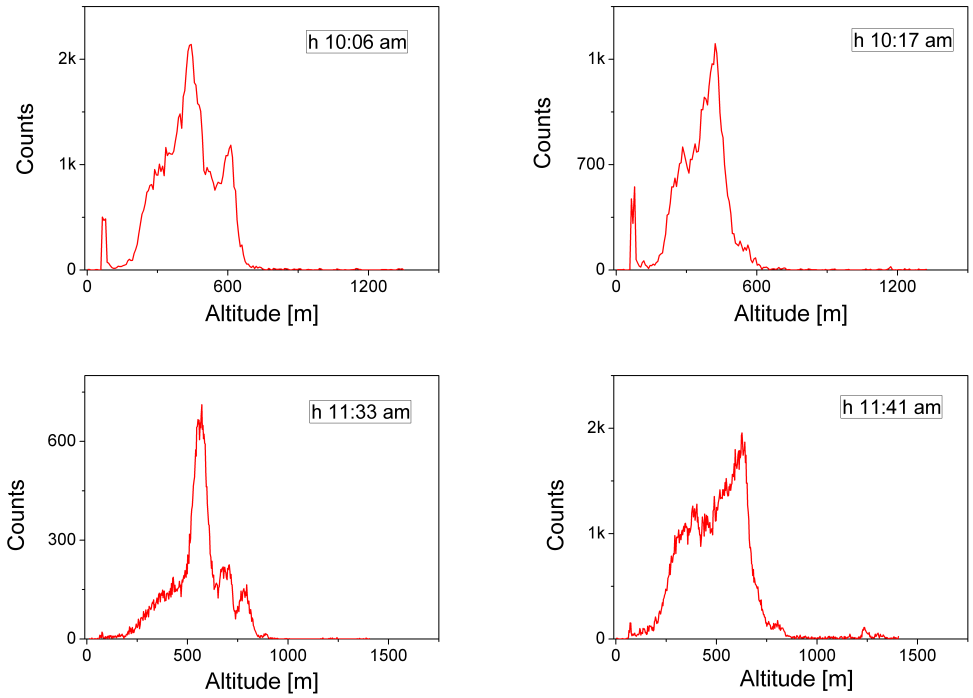

Figure 5.9: Signals of 5 minutes long acquisitions at different times.

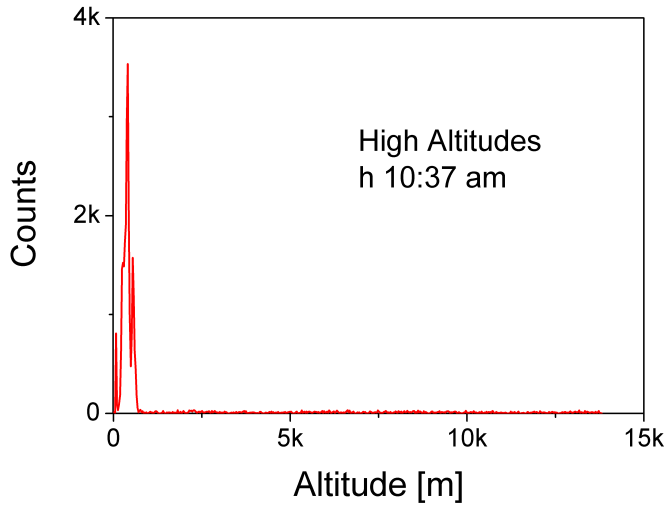

Figure 5.10: High altitude signal at 1064nm.

for every classical sensor is too low to be used here.

The measurement, not performed due to the COVID-19 outbreak, is expected to be realized

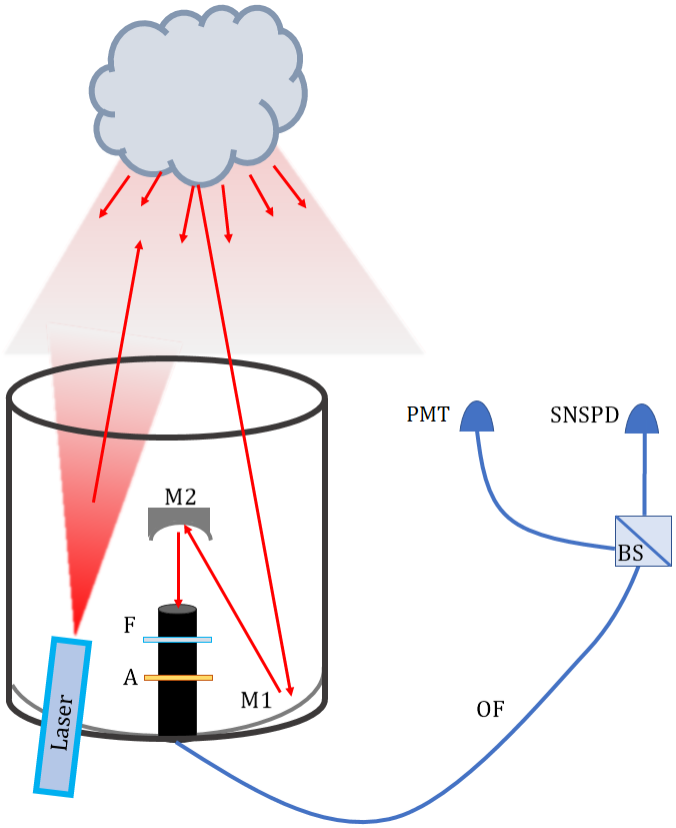

Figure 5.11: Sketch of Lidar measurement setup assembled during BRIT measurement campaign at Wuhan University. The laser is placed inside the telescope though a hole in the mirror M1. The laser direction can be adjusted with mechanic handlers. The backscattered light is collected by M1 and M2 (placed in the focus) and directed inside the collimator (black cylinder) where a filter (F) and variable attenuators (A) can be placed. An optical fiber (OF) with beam splitter (BS) separates the signal in two channels directed to the PMT and the SNSPD.

in the next future and will be organised in the following steps:

- aerosol measurement with 1064nm and 532nm elastic Lidars;
- simultaneous aerosol measurement at 1064nm with conventional PMT and SNSPD and comparison;
- aerosol measurement with SNSPD at 1550nm.

Summary

In this chapter the results of lidar measurement with NbTiN SNSPD are presented.
First, we calculated the distance of an hard target by measuring the time of flight of 1550nm photons. In order to do that, we realized a prototype lidar with a 20x collimator, a low power continuous laser and a modulator. Through this measurement we demonstrated the technical feasibility of a lidar measurement with SNSPD at 1550nm, we tested the acquisition programs and the electronics.
After this proof of principle demonstration, we worked at the integration of a SNSPD in MALIA setup, a multi-wavelength lidar which provides information about aerosols and clouds to the European network EARLINET. The integration of the SNSPD was not straightforward as the receiver setup could not be modified and the space to introduce new optical elements was reduced. We could integrate the SNSPD in MALIA with the support of a cage system and we successfully measured the signal at 1064nm.
In the end of the Chapter, I give a description of the activities carried on during the abroad period spent at Beijing Research Institute of Telemetry (Beijing, PRC).

Conclusions and future perspectives

The main goal to be achieved in this thesis work was to show that the Superconducting Nanowire Single Photon Detectors can be used for a Lidar measurement in the infrared wavelength domain. In order to achieve this goal, all the topics concerning fabrication, characterization, measurement setup, operating principles, were dealt with.

The main requirements to be accomplished for a Lidar measurement with SNSPD at A.l.a. shared laboratories (Naples, Italy) and at BRIT (Beijing, PRC) was to realize a versatile and transportable measurement setup and to fabricate and test a large area SNSPD, with a good signal to noise ratio at $\lambda = 1 - 2\mu m$.
In order to do that, the first step was to design and test the electronic readout circuits and write the acquisition programs. In this sense, the steps followed the literature and no innovation were introduced in the setup; hence, this aspect was marginally treated here.
Secondly, lots of work was devoted to the fabrication and characterization of SNSPD with different materials and geometries. In particular, both crystalline and amorphous materials were explored, some of which may be considered as *classical*, such as NbN, NbTiN, MoSi, while others, such as NbRe, have never been used as detectors. All the SNSPDs and nanowires were tested in a wide range of temperatures but a special care was dedicated to the research of good performances at a temperature of 4.2K. This requirement was due to the fact that a measurement in liquid helium was considered, at this stage, more versatile.
Beside the materials, also different geometries have been realized and tested. In particular, a parallel nanowires geometry was tested with 2-4 NbN nanowires of different widths (80,100,120 nm). Increasing the number of parallel nanowires meant the reduction of the dead time and, at the same time, larger area devices.
Some months were also spent to design and test a new cryogenic insert, dedicated to the measurement of two chips at different wavelengths. It was equipped with two $50\mu m$ core multimode fibers with acceptable wavelengths in the range 400-2200nm and two coaxial cables. Each detector is connected to a stage of low temperature filters and both channels are equipped with a 50Ω parallel resistor. The insert is vacuum sealed and can be used in liquid

helium, also when pumped ($T \sim 1.5K$). The fiber connectors are FC/PC and coaxial cables are endowed of SMA connectors.

Before the realization of a Lidar measurement with SNSPD, we realized a prototype Lidar system at 1550nm and measured the distance of an hard target with a NbTiN detector at 4.2K. This measurement was carried on also to test the electronic setup, the acquisition programs and the cryogenic insert.

With the support of A.l.a. S.r.l. and the Lidar team in the University of Naples, a method to couple the 1064nm signal collected with MALIA to a SNSPD was designed, assembled and tested.
MALIA, Multi-wavelength Aerosol LIdar Apparatus, is a system which collects the Lidar elastic and inelastic signals at 1064nm, 607nm, 532nm (P and S components), 407nm, 386nm, 355nm. It also analyses the polarization and with these informations the system is able to measure aerosols and cloud profiles, water vapour mixing ratio and α and β coefficients as a function of the altitude.
MALIA is embedded in the European network EARLINET and it uploads the collected data twice a week. Hence, to perform a measurement with a SNSPD it was not possible to make great modifications to the system. Therefore, a cage system to collect part of the 1064nm signal, reduce the beam size and collimate the light on a single mode fiber was realized. It was first aligned and tested in the lab and that moved onto MALIA.
With that cage system we were able to measure the signal at 1064nm with a NbTiN SNSPD, successfully demonstrating the feasibility of a Lidar measurement with SNSPD. Unfortunately, the weather was not good during the measurement campaign and we could not measure the aerosol content but just a low altitude cloud.

Part of this PhD was spent at Beijing Institute of Telemetry (Beijing, PRC) where I used different lidar systems with $\lambda > 1\mu m$. Moreover, a setup for simultaneous measurement of aerosols at 1064nm with a PMT and SNSPD was realized. With the help of BRIT and Wuhan University, also an aerosol Lidar system at 1550nm was designed and assembled where I predisposed the optics for a measurement with SNSPD. Indeed, at this wavelength, it is not possible to realize an aerosol measurement with conventional detectors and just the SNSPD coupling was prepared.
Due to the spreading of COVID-19 the measurement campaign, planned to take place at Wuhan University, was suspended.

Finally, a study of dark counts formation though the analysis of switching current distributions in SNSPD was carried on. Reducing the dark counts is fundamental for all those applications which involves low signals, as dark matter detection or Lidar for low density aerosols or high altitudes molecules and compound profiling.
The experimental results show that the dark count rate depends on the temperature and on the current in a more complicated way than as expected. In details, we observed a crossover

temperature T^* before which a single thermal fluctuation can produce a dark count while, above T^* more fluctuations are required. The direct consequence in a counter-intuitive result: as the temperature increases, the statistical noise il lowered with the effect that dark count rate, at $I_b \sim 0.95 I_c$ lowers as the temperature increases.
We also compared the dark count statistics of a NbN and a NbTiN SNSPD; the latter was introduced because of lower DCR but we observed that this feature is strictly connected with temperature and bias current and, in some conditions, DCR is lower in NbN than in NbTiN.

Many activities have been carried out and the basis for future work were settled down. In particular, next activities may include

- a comparison between the performances of SNSPD and PMT in a aerosol measurement with a Lidar at $\lambda = 1064nm$;
- a measurement of aerosol with a SNSPD-based Lidar operating at $\lambda = 1550nm$
- a study of switching current distributions on superconducting strips of different width and on meanders to investigate the role the geometry play in dark count formation;
- a study of switching current distribution on SNSPD realized with MoSi and other amorphous materials to explore the role of lattice and materials in dark count formation.

Lidar measurements with SNSPD will be included in the activities of OT4CLIMA, a PON project funded by Miur devoted to the monitoring of the climate changes with innovative methods aimed at a quantification of the damages due to environmental pollution.
After these measurements an accurate knowledge of SNSPD physics and Lidar systems in the infrared will be reached and a Lidar at $2\mu m$ for carbon dioxide profiles measurements with SNSPD will be realized.
The technology presented here will hence give a significant contribution in environmental monitoring, now fundamental and of primary importance given the latest critical weather phenomena.

List of Publications and Awards

- *Characterization of scalable Josephson memory element containing a strong ferromagnet*, L. Parlato, R. Caruso, A. Vettoliere, R. Satariano, H. Ahmad, A. Miano, D. Montemurro, **D. Salvoni**, G. Ausanio, F. Tafuri, G. P. Pepe, D. Massarotti, C. Granata, [to be published in *Journal of Applied Physics*].

- *Dark counts double switching rates in NbTiN Superconducting Nanowire Single Photon Detectors*, **D. Salvoni**, M. Ejrnaes, L. Parlato, X. Y. Yang, L. X. You, Z. Wang, G. P. Pepe and R. Cristiano, [to be published in *Journal of Physics: Conference Series*].

- *Ultrathin superconducting NbRe microstrips with hysteretic Voltage-Current characteristic*, C. Cirillo, M. Caputo, L. Parlato, M. Ejrnaes, **D. Salvoni**, R. Cristiano, G. P. Pepe and C. Attanasio, 2020, Low Temperature Physics, 46(4), pp. 379-382.

- *The role of multiple fluctuation events in NbN and NbTiN Superconducting Nanostrip Single-Photon Detectors*, L. Parlato, **D. Salvoni**, M. Ejrnaes, D. Massarotti, R. Caruso, R. Satariano, F. Tafuri, X. Y. Yang, L. You, Z. Wang, G. P. Pepe and R. Cristiano, 2020, Journal of Low Temperature Physics, pp. 1-6.

- *Application of Doppler Radar Parameters in Hail Cloud Identification in the Ili River Valley*, W.Y. Feng, Z. Wang, L. Shi, X. Huang, **D. Salvoni**, L. Zhang, in 2019 International Conference on Meteorology Observations (ICMO) pp. 1-4. IEEE.

- *Superconductor to resistive state switching by multiple fluctuation events in NbTiN nanostrips*, M. Ejrnaes, **D. Salvoni**, L. Parlato, D. Massarotti, R. Caruso, F. Tafuri, X. Y. Yang, L. X. You, Z. Wang, G. P. Pepe and R. Cristiano, 2019, Scientific Reports, 9(1) pp.1-6.

- *Lidar techniques for a SNSPD-based measurement*, **D. Salvoni**, M. Ejrnaes, L. Parlato, A. Sannino, A. Boselli, G. P. Pepe, R. Cristiano and X. Wang, 2019, Journal of Physics: Conference Series, 1182(1) pp. 012014-20.

- **Best Poster Awards** [Third Prize], *Superconductor to resistive state switching by multiple fluctuation events in NbTiN nanostrips*, SNSPD Workshop, Bad Honnef (Germany), 12-16 November 2018.

Acknowledgements

There are many people that, with their support, helped me to achieve the results presented in this thesis and I want to mention them here.

First, I want to express my gratitude to my supervisor Prof. Giampiero Pepe who introduced me to this fascinating topic and often stimulated my professional growth with interesting readings, challenges and discussions. I also want to thank him for the constant sustain and trust.

I want to mention also Prof. Roberto Cristiano and Dr. Mikkel Ejrnaes of *National Research Council* who guided me in the delicate passage from high energy theoretical physics to experimental superconductivity. Apart from their friendly and daily presence, I want to thank Roberto for his guidance and discussions on superconductivity and Mikkel for teaching me everything about the Lab life.

A special contribution to this work was given by Prof. Loredana Parlato, not only for the plenty of interesting scientific discussions, but also for the constant and affectionate human support. I also want to thank her for the enthusiastic and propositive spirit that often motivated me to give my best.

A great sustain was also given by Prof. Xuan Wang, Dr. Antonella Boselli and Prof. Nicola Spinelli, ALA S.r.l. founders and experts in the field of Lidar. In particular I want to thank Prof. Spinelli for the introductory discussions, Prof. Wang for his technical suggestions and original ideas and Dr. Boselli for the intense help in the realization of the optical coupling between MALIA and SNSPD and the constant guidance in the field of Lidar.

I want to thank my supervisor at BRIT, Dr. Zhao Yiming who involved me in very interesting and constitutive measurement campaigns. I am extremely grateful to Mr. Chen, Miss Buzhichao of *Chinese Meteorological Administration* and Prof. Xuan Wang for the help

during the measurements in Beijing and Wuhan and for the continuous practical support during my stay in China.

I to mention here also Prof. Francesco Tafuri, Dr. Davide Massarotti and Dr. Roberta Caruso for the acquisition of the switching current distributions analysed in Chap.3 and for the clear and interesting discussions which followed.

I want to thank the group of Prof. Roberto Leoni, in particular Dr. Francesco Mattioli, of the Institute for Photonics and Nanotechnologies - CNR in Rome (Italy), for the fruitful collaboration in the nanopattering of MoSi and NbN SNSPDs.

Moreover, I want to thank the group of Prof. Lixing You od SIMIT (Shanghai, PRC) for supplying the NbTiN and NbN SNSPD used for the study of switching current distributions and the Lidar measurement at 1064nm.

I cannot skip my special thanks to the technical support received by Mr. Giuseppe Passeggio (ALA), Mr. Giuseppe Pontoriere, Mr. Stefano Marrazzo and Mr. Paolo Scotto di Vettimo, for the rapid and precise interventions on the experimental setup.

I want also to remember Dr. Alessia Sannino, all the collegues in the PhD room and my friends for the friendly support during these three years and the scientific suggestions.

My affectionate thanks goes to Mr. Guido Celentano, a safety net in all the plenty of complicated papers, documentation and difficult issues we had to face during these years. I could always rely on his prepared and precise intervention.

Last but not least I must express my gratitude to Pierpaolo and my family that always stand by my side, even with thousand kilometers in between.

Bibliography

[1] Alexei D Semenov, Gregory N Gol'tsman, and Roman Sobolewski. Hot-electron effect in superconductors and its applications for radiation sensors. *Superconductor Science and Technology*, 15(4):R1, 2002.

[2] Andreas Engel, AD Semenov, H-W Hübers, Konstantin Il'in, and Michael Siegel. Fluctuation effects in superconducting nanostrips. *Physica C: Superconductivity and its applications*, 444(1-2):12–18, 2006.

[3] Chandra M Natarajan, Michael G Tanner, and Robert H Hadfield. Superconducting nanowire single-photon detectors: physics and applications. *Superconductor science and technology*, 25(6):063001, 2012.

[4] F Marsili, Varun B Verma, Jeffrey A Stern, S Harrington, Adriana E Lita, Thomas Gerrits, Igor Vayshenker, Burm Baek, Matthew D Shaw, Richard P Mirin, et al. Detecting single infrared photons with 93% system efficiency. *Nature Photonics*, 7(3):210, 2013.

[5] Francesco Marsili, Francesco Bellei, Faraz Najafi, Andrew E Dane, Eric A Dauler, Richard J Molnar, and Karl K Berggren. Efficient single photon detection from 500 nm to 5 μm wavelength. *Nano letters*, 12(9):4799–4804, 2012.

[6] H Bartolf, A Engel, A Schilling, K Il'In, M Siegel, H-W Hübers, and A Semenov. Current-assisted thermally activated flux liberation in ultrathin nanopatterned nbn superconducting meander structures. *Physical Review B*, 81(2):024502, 2010.

[7] D Massarotti, L Longobardi, L Galletti, D Stornaiuolo, D Montemurro, G Pepe, Giacomo Rotoli, A Barone, and Francesco Tafuri. Escape dynamics in moderately damped josephson junctions. *Low Temperature Physics*, 38(4):263–272, 2012.

[8] Mitrabhanu Sahu, Myung-Ho Bae, Andrey Rogachev, David Pekker, Tzu-Chieh Wei, Nayana Shah, Paul M Goldbart, and Alexey Bezryadin. Individual topological tunnelling events of a quantum field probed through their macroscopic consequences. *Nature Physics*, 5(7):503–508, 2009.

[9] Peng Li, Phillip M Wu, Yuriy Bomze, Ivan V Borzenets, Gleb Finkelstein, and AM Chang. Switching currents limited by single phase slips in one-dimensional superconducting al nanowires. *Physical review letters*, 107(13):137004, 2011.

[10] David Pekker, Nayana Shah, Mitrabhanu Sahu, Alexey Bezryadin, and Paul M Goldbart. Stochastic dynamics of phase-slip trains and superconductive-resistive switching in current-biased nanowires. *Physical Review B*, 80(21):214525, 2009.

[11] Andrew Murphy, Alexander Semenov, Alexander Korneev, Yulia Korneeva, Gregory Gol'tsman, and Alexey Bezryadin. Three temperature regimes in superconducting photon detectors: quantum, thermal and multiple phase-slips as generators of dark counts. *Scientific reports*, 5(1):1–10, 2015.

[12] Anthony J Illingworth, HW Barker, A Beljaars, Marie Ceccaldi, H Chepfer, Nicolas Clerbaux, J Cole, Julien Delanoë, C Domenech, David P Donovan, et al. The earthcare satellite: The next step forward in global measurements of clouds, aerosols, precipitation, and radiation. *Bulletin of the American Meteorological Society*, 96(8):1311–1332, 2015.

[13] Jiawei Qiu, Haiyun Xia, Mingjia Shangguan, Xiankang Dou, Manyi Li, Chong Wang, Xiang Shang, Shengfu Lin, and Jianjiang Liu. Micro-pulse polarization lidar at 1.5 μm using a single superconducting nanowire single-photon detector. *Optics letters*, 42(21):4454–4457, 2017.

[14] Nobuo Sugimoto and Choo Hie Lee. Characteristics of dust aerosols inferred from lidar depolarization measurements at two wavelengths. *Applied optics*, 45(28):7468–7474, 2006.

[15] RTH Collis and PB Russell. Lidar measurement of particles and gases by elastic backscattering and differential absorption. In *Laser monitoring of the atmosphere*, pages 71–151. Springer, 1976.

[16] Raymond M Sova, Michael E Thomas, David Tobin, Daniel Byrum, and L Larrabee Strow. Characterization of candidate dial lidar water-vapor and carbon dioxide absorption lines in the 2-um region. In *Optical Instrumentation for Gas Emissions Monitoring and Atmospheric Measurements*, volume 2366, pages 383–393. International Society for Optics and Photonics, 1995.

[17] Matthew D Eisaman, Jingyun Fan, Alan Migdall, and Sergey V Polyakov. Invited review article: Single-photon sources and detectors. *Review of scientific instruments*, 82(7):071101, 2011.

[18] Boris Korzh, Qing-Yuan Zhao, Jason P Allmaras, Simone Frasca, Travis M Autry, Eric A Bersin, Andrew D Beyer, Ryan M Briggs, Bruce Bumble, Marco Colangelo, et al. Demonstration of sub-3 ps temporal resolution with a superconducting nanowire single-photon detector. *Nature Photonics*, pages 1–6, 2020.

[19] GN Gol'Tsman, O Okunev, G Chulkova, A Lipatov, A Semenov, K Smirnov, B Voronov, A Dzardanov, C Williams, and Roman Sobolewski. Picosecond superconducting single-photon optical detector. *Applied physics letters*, 79(6):705–707, 2001.

[20] Alex D Semenov, Gregory N Gol'tsman, and Alexander A Korneev. Quantum detection by current carrying superconducting film. *Physica C: Superconductivity*, 351(4):349–356, 2001.

[21] Hiroyuki Shibata, Kaoru Shimizu, Hiroki Takesue, and Yasuhiro Tokura. Superconducting nanowire single-photon detector with ultralow dark count rate using cold optical filters. *Applied Physics Express*, 6(7):072801, 2013.

[22] G Fiocco and LD Smullin. Detection of scattering layers in the upper atmosphere (60-140 km) by optical radar. *Nature*, 199(4900):1275–1276, 1963.

[23] Kamerlingh H Onnes. Further experiments with liquid helium. c. on the change of electric resistance of pure metals at very low temperatures etc. Comm. 120b, 122b, 124c, Phys. Lab. Leiden University, 1911.

[24] Kamerlingh H Onnes. Further experiments with liquid helium. c. on the change of electric resistance of pure metals at very low temperatures etc. Comm. 133b, 133d, Phys. Lab. Leiden University, 1913.

[25] Walther Meissner and Robert Ochsenfeld. Ein neuer effekt bei eintritt der supraleitfähigkeit. *Naturwissenschaften*, 21(44):787–788, 1933.

[26] John Bardeen, Leon N Cooper, and John Robert Schrieffer. Theory of superconductivity. *Physical review*, 108(5):1175, 1957.

[27] Lev Petrovich Gor'kov. Microscopic derivation of the ginzburg-landau equations in the theory of superconductivity. *Sov. Phys. JETP*, 9(6):1364–1367, 1959.

[28] Charles K Poole, Horacio A Farach, and Richard J Creswick. *Handbook of superconductivity*. Elsevier, 1999.

[29] Michael Tinkham. *Introduction to superconductivity*. Courier Corporation, 2004.

[30] Judea Pearl. Structure of superconductive vortices near a metal-air interface. *Journal of Applied Physics*, 37(11):4139–4141, 1966.

[31] Milind N Kunchur. Evaluating superconductors through current induced depairing. *Condensed Matter*, 4(2):54, 2019.

[32] Berggren K. Kinetic inductance explained. Youtube, 2011.

[33] AM Kadin and MW Johnson. Nonequilibrium photon-induced hotspot: A new mechanism for photodetection in ultrathin metallic films. *Applied Physics Letters*, 69(25):3938–3940, 1996.

[34] SN Dorenbos, P Forn-Diaz, T Fuse, AH Verbruggen, T Zijlstra, TM Klapwijk, and V Zwiller. Low gap superconducting single photon detectors for infrared sensitivity. *Applied Physics Letters*, 98(25):251102, 2011.

[35] Joel KW Yang, Andrew J Kerman, Eric A Dauler, Vikas Anant, Kristine M Rosfjord, and Karl K Berggren. Modeling the electrical and thermal response of superconducting nanowire single-photon detectors. *IEEE transactions on applied superconductivity*, 17(2):581–585, 2007.

[36] AG Kozorezov, AF Volkov, JK Wigmore, A Peacock, A Poelaert, and R Den Hartog. Quasiparticle-phonon downconversion in nonequilibrium superconductors. *Physical Review B*, 61(17):11807, 2000.

[37] AG Kozorezov, C Lambert, F Marsili, MJ Stevens, VB Verma, JP Allmaras, MD Shaw, RP Mirin, and Sae Woo Nam. Fano fluctuations in superconducting-nanowire single-photon detectors. *Physical Review B*, 96(5):054507, 2017.

[38] L Parlato, R Latempa, G Peluso, GP Pepe, R Cristiano, and R Sobolewski. The characteristic electron–phonon coupling time of unconventional superconductors and implications for optical detectors. *Superconductor Science and Technology*, 18(9):1244, 2005.

[39] Francesco Marsili, Martin J Stevens, Alex Kozorezov, Varun B Verma, Colin Lambert, Jeffrey A Stern, Robert D Horansky, S Dyer, S Duff, David P Pappas, et al. Hotspot relaxation dynamics in a current-carrying superconductor. *Physical Review B*, 93(9):094518, 2016.

[40] AN Zotova and D Yu Vodolazov. Intrinsic detection efficiency of superconducting nanowire single photon detector in the modified hot spot model. *Superconductor Science and Technology*, 27(12):125001, 2014.

[41] WJ Skocpol, MR Beasley, and M Tinkham. Self-heating hotspots in superconducting thin-film microbridges. *Journal of Applied Physics*, 45(9):4054–4066, 1974.

[42] Andrew J Kerman, Eric A Dauler, William E Keicher, Joel KW Yang, Karl K Berggren, G Gol'Tsman, and B Voronov. Kinetic-inductance-limited reset time of superconducting nanowire photon counters. *Applied physics letters*, 88(11):111116, 2006.

[43] M Ejrnaes, A Casaburi, O Quaranta, S Marchetti, A Gaggero, F Mattioli, R Leoni, S Pagano, and R Cristiano. Characterization of parallel superconducting nanowire single photon detectors. *Superconductor Science and Technology*, 22(5):055006, 2009.

[44] Lixing You, Xiaoyan Yang, Yuhao He, Wenxing Zhang, Dengkuan Liu, Weijun Zhang, Lu Zhang, Ling Zhang, Xiaoyu Liu, Sijing Chen, et al. Jitter analysis of a superconducting nanowire single photon detector. *Aip Advances*, 3(7):072135, 2013.

[45] Mariia Sidorova, Alexej Semenov, Heinz-Wilhelm Hübers, Ilya Charaev, Artem Kuzmin, Steffen Doerner, and Michael Siegel. Physical mechanisms of timing jitter in photon detection by current-carrying superconducting nanowires. *Physical Review B*, 96(18):184504, 2017.

[46] Niccolò Calandri, Qing-Yuan Zhao, Di Zhu, Andrew Dane, and Karl K Berggren. Superconducting nanowire detector jitter limited by detector geometry. *Applied Physics Letters*, 109(15):152601, 2016.

[47] JA O'Connor, MG Tanner, CM Natarajan, GS Buller, RJ Warburton, S Miki, Z Wang, SW Nam, and RH Hadfield. Spatial dependence of output pulse delay in a niobium nitride nanowire superconducting single-photon detector. *Applied physics letters*, 98(20):201116, 2011.

[48] Lars Lydersen, Carlos Wiechers, Christoffer Wittmann, Dominique Elser, Johannes Skaar, and Vadim Makarov. Hacking commercial quantum cryptography systems by tailored bright illumination. *Nature photonics*, 4(10):686, 2010.

[49] WeiJun Zhang, LiXing You, Hao Li, Jia Huang, ChaoLin Lv, Lu Zhang, XiaoYu Liu, JunJie Wu, Zhen Wang, and XiaoMing Xie. Nbn superconducting nanowire single photon detector with efficiency over 90% at 1550 nm wavelength operational at compact cryocooler temperature. *Science China Physics, Mechanics & Astronomy*, 60(12):120314, 2017.

[50] Hao Li, Heqing Wang, Lixing You, Peng Hu, Weidong Shen, Weijun Zhang, Xiaoyan Yang, Lu Zhang, Hui Zhou, Zhen Wang, et al. Multispectral superconducting nanowire single photon detector. *Optics express*, 27(4):4727–4733, 2019.

[51] Andreas Engel, Kevin Inderbitzin, Andreas Schilling, Robert Lusche, Alexei Semenov, Heinz-Wilhelm Hübers, Dagmar Henrich, Matthias Hofherr, Konstantin Il'in, and Michael Siegel. Temperature-dependence of detection efficiency in nbn and tan snspd. *IEEE Transactions on Applied Superconductivity*, 23(3):2300505–2300505, 2013.

[52] WJ Zhang, XY Yang, H Li, LX You, CL Lv, L Zhang, CJ Zhang, XY Liu, Z Wang, and XM Xie. Fiber-coupled superconducting nanowire single-photon detectors integrated with a bandpass filter on the fiber end-face. *Superconductor Science and Technology*, 31(3):035012, 2018.

[53] M Ejrnaes, D Salvoni, L Parlato, D Massarotti, R Caruso, F Tafuri, XY Yang, LX You, Z Wang, GP Pepe, et al. superconductor to resistive state switching by multiple fluctuation events in nbtin nanostrips. *Scientific reports*, 9(1):1–6, 2019.

[54] Yonit Hochberg, Ilya Charaev, Sae-Woo Nam, Varun Verma, Marco Colangelo, and Karl K Berggren. Detecting sub-gev dark matter with superconducting nanowires. *Physical review letters*, 123(15):151802, 2019.

[55] Mark A Itzler, Xudong Jiang, Mark Entwistle, Krystyna Slomkowski, Alberto Tosi, Fabio Acerbi, Franco Zappa, and Sergio Cova. Advances in ingaasp-based avalanche diode single photon detectors. *Journal of Modern Optics*, 58(3-4):174–200, 2011.

[56] Nicolas Gisin, Grégoire Ribordy, Wolfgang Tittel, and Hugo Zbinden. Quantum cryptography. *Reviews of modern physics*, 74(1):145, 2002.

[57] Hua-Lei Yin, Teng-Yun Chen, Zong-Wen Yu, Hui Liu, Li-Xing You, Yi-Heng Zhou, Si-Jing Chen, Yingqiu Mao, Ming-Qi Huang, Wei-Jun Zhang, et al. Measurement-device-independent quantum key distribution over a 404 km optical fiber. *Physical review letters*, 117(19):190501, 2016.

[58] Xiao-Tian Fang, Pei Zeng, Hui Liu, Mi Zou, Weijie Wu, Yan-Lin Tang, Ying-Jie Sheng, Yao Xiang, Weijun Zhang, Hao Li, et al. Implementation of quantum key distribution surpassing the linear rate-transmittance bound. *Nature Photonics*, pages 1–4, 2020.

[59] Jiu-Peng Chen, Chi Zhang, Yang Liu, Cong Jiang, Weijun Zhang, Xiao-Long Hu, Jian-Yu Guan, Zong-Wen Yu, Hai Xu, Jin Lin, et al. Sending-or-not-sending with independent lasers: Secure twin-field quantum key distribution over 509 km. *Physical Review Letters*, 124(7):070501, 2020.

[60] Scott Aaronson and Alex Arkhipov. The computational complexity of linear optics. In *Proceedings of the forty-third annual ACM symposium on Theory of computing*, pages 333–342, 2011.

[61] Bryan T Gard, Keith R Motes, Jonathan P Olson, Peter P Rohde, and Jonathan P Dowling. An introduction to boson-sampling. In *From atomic to mesoscale: The role of quantum coherence in systems of various complexities*, pages 167–192. World Scientific, 2015.

[62] Hui Wang, Wei Li, Xiao Jiang, Y-M He, Y-H Li, Xing Ding, M-C Chen, Jian Qin, C-Z Peng, Christian Schneider, et al. Toward scalable boson sampling with photon loss. *Physical review letters*, 120(23):230502, 2018.

[63] Han-Sen Zhong, Yuan Li, Wei Li, Li-Chao Peng, Zu-En Su, Yi Hu, Yu-Ming He, Xing Ding, Weijun Zhang, Hao Li, et al. 12-photon entanglement and scalable scattershot boson sampling with optimal entangled-photon pairs from parametric down-conversion. *Physical review letters*, 121(25):250505, 2018.

[64] Hui Wang, Jian Qin, Xing Ding, Ming-Cheng Chen, Si Chen, Xiang You, Yu-Ming He, Xiao Jiang, L You, Z Wang, et al. Boson sampling with 20 input photons and a 60-mode interferometer in a 1 0 14-dimensional hilbert space. *Physical review letters*, 123(25):250503, 2019.

[65] John S Bell. On the einstein podolsky rosen paradox. *Physics Physique Fizika*, 1(3):195, 1964.

[66] Alain Aspect, Philippe Grangier, and Gérard Roger. Experimental tests of realistic local theories via bell's theorem. *Physical review letters*, 47(7):460, 1981.

[67] Yang Liu, Qi Zhao, Ming-Han Li, Jian-Yu Guan, Yanbao Zhang, Bing Bai, Weijun Zhang, Wen-Zhao Liu, Cheng Wu, Xiao Yuan, et al. Device-independent quantum random-number generation. *Nature*, 562(7728):548–551, 2018.

[68] MD Shaw, Francesco Marsili, AD Beyer, JA Stern, GV Resta, Prasana Ravindran, S Chang, Joseph Bardin, DS Russell, JW Gin, et al. Arrays of wsi superconducting nanowire single photon detectors for deep-space optical communications. In *2015 Conference on Lasers and Electro-Optics (CLEO)*, pages 1–2. IEEE, 2015.

[69] Kazuharu Bamba, Salvatore Capozziello, Shin'ichi Nojiri, and Sergei D Odintsov. Dark energy cosmology: the equivalent description via different theoretical models and cosmography tests. *Astrophysics and Space Science*, 342(1):155–228, 2012.

[70] Carlos Munoz. Dark matter detection in the light of recent experimental results. *International Journal of Modern Physics A*, 19(19):3093–3169, 2004.

[71] James Abshire, Anand Ramanathan, Haris Riris, Jianping Mao, Graham Allan, William Hasselbrack, Clark Weaver, and Edward Browell. Airborne measurements of co2 column concentration and range using a pulsed direct-detection ipda lidar. *Remote Sensing*, 6(1):443–469, 2014.

[72] D Salvoni, M Ejrnaes, L Parlato, A Sannino, A Boselli, GP Pepe, R Cristiano, and X Wang. Lidar techniques for a snspd-based measurement. In *Journal of Physics: Conference Series*, volume 1182, page 012014. IOP Publishing, 2019.

[73] Jiang Zhu, Yajun Chen, Labao Zhang, Xiaoqing Jia, Zhijun Feng, Ganhua Wu, Xiachao Yan, Jiquan Zhai, Yang Wu, Qi Chen, et al. Demonstration of measuring sea fog with an snspd-based lidar system. *Scientific reports*, 7(1):15113, 2017.

[74] Mingjia Shangguan, Haiyun Xia, Chong Wang, Jiawei Qiu, Shengfu Lin, Xiankang Dou, Qiang Zhang, and Jian-Wei Pan. Dual-frequency doppler lidar for wind detection with a superconducting nanowire single-photon detector. *Optics letters*, 42(18):3541–3544, 2017.

[75] Lu Zhang, Lixing You, Xiaoyan Yang, Junjie Wu, Chaolin Lv, Qi Guo, Weijun Zhang, Hao Li, Wei Peng, Zhen Wang, et al. Hotspot relaxation time of nbn superconducting nanowire single-photon detectors on various substrates. *Scientific reports*, 8(1):1486, 2018.

[76] Francesco Mattioli, Mikkel Ejrnaes, Alessandro Gaggero, Alessandro Casaburi, Roberto Cristiano, Sergio Pagano, and Roberto Leoni. Large area single photon detectors based on parallel configuration nbn nanowires. *Journal of Vacuum Science & Technology B, Nanotechnology and Microelectronics: Materials, Processing, Measurement, and Phenomena*, 30(3):031204, 2012.

[77] Chengjun Zhang, Weijun Zhang, Jia Huang, Lixing You, Hao Li, Chaolin lv, Tatsuki Sugihara, Masahiko Watanabe, Hui Zhou, Zhen Wang, et al. Nbn superconducting nanowire single-photon detector with an active area of 300 μm-in-diameter. *AIP Advances*, 9(7):075214, 2019.

[78] M Ejrnaes, A Casaburi, S Pagano, F Mattioli, A Gaggero, R Leoni, and R Cristiano. Superconducting single photon detectors based on parallel nbn nanowires. In *Photon Counting Applications, Quantum Optics, and Quantum Information Transfer and Processing III*, volume 8072, page 807203. International Society for Optics and Photonics, 2011.

[79] Yu P Korneeva, M Yu Mikhailov, Yu P Pershin, NN Manova, AV Divochiy, Yu B Vakhtomin, AA Korneev, KV Smirnov, AG Sivakov, A Yu Devizenko, et al. Superconducting single-photon detector made of mosi film. *Superconductor Science and Technology*, 27(9):095012, 2014.

[80] C Cirillo, R Fittipaldi, M Smidman, G Carapella, C Attanasio, A Vecchione, Ravi P Singh, MR Lees, G Balakrishnan, and M Cuoco. Evidence of double-gap superconductivity in noncentrosymmetric nb 0.18 re 0.82 single crystals. *Physical Review B*, 91(13):134508, 2015.

[81] C Cirillo, G Carapella, M Salvato, R Arpaia, M Caputo, and C Attanasio. Superconducting properties of noncentrosymmetric nb 0.18 re 0.82 thin films probed by transport and tunneling experiments. *Physical Review B*, 94(10):104512, 2016.

[82] M Caputo, C Cirillo, and C Attanasio. Nbre as candidate material for fast single photon detection. *Applied Physics Letters*, 111(19):192601, 2017.

[83] Yu P Korneeva, NN Manova, IN Florya, M Yu Mikhailov, OV Dobrovolskiy, AA Korneev, and D Yu Vodolazov. Different single-photon response of wide and narrow superconducting mo x si 1- x strips. *Physical Review Applied*, 13(2):024011, 2020.

[84] C Cirillo, M Caputo, L Parlato, M Ejrnaes, D Salvoni, R Cristiano, GP Pepe, and C Attanasio. Ultrathin superconducting nbre microstrips with hysteretic voltage-current characteristic. *Low Temperature Physics*, 46(4), 2020.

[85] John Michael Kosterlitz and David James Thouless. Ordering, metastability and phase transitions in two-dimensional systems. *Journal of Physics C: Solid State Physics*, 6(7):1181, 1973.

[86] MR Beasley, JE Mooij, and TP Orlando. Possibility of vortex-antivortex pair dissociation in two-dimensional superconductors. *Physical Review Letters*, 42(17):1165, 1979.

[87] William A Little. Decay of persistent currents in small superconductors. *Physical Review*, 156(2):396, 1967.

[88] James S Langer and Vinay Ambegaokar. Intrinsic resistive transition in narrow superconducting channels. *Physical Review*, 164(2):498, 1967.

[89] Fabio Altomare and Albert M Chang. *One-dimensional superconductivity in nanowires*. John Wiley & Sons, 2013.

[90] Holger Bartolf. Fluctuation mechanisms in superconductors. In *Fluctuation Mechanisms in Superconductors*, pages 181–184. Springer, 2016.

[91] J Kitaygorsky, J Zhang, A Verevkin, A Sergeev, A Korneev, V Matvienko, P Kouminov, K Smirnov, B Voronov, G Gol'tsman, et al. Origin of dark counts in nanostructured nbn single-photon detectors. *IEEE transactions on applied superconductivity*, 15(2):545–548, 2005.

[92] J Kitaygorsky, I Komissarov, A Jukna, D Pan, O Minaeva, N Kaurova, A Divochiy, A Korneev, M Tarkhov, B Voronov, et al. Dark counts in nanostructured nbn superconducting single-photon detectors and bridges. *IEEE Transactions on Applied Superconductivity*, 17(2):275–278, 2007.

[93] John Bardeen and MJ Stephen. Theory of the motion of vortices in superconductors. *Physical Review*, 140(4A):A1197, 1965.

[94] KK Likharev. Superconducting weak links. *Reviews of Modern Physics*, 51(1):101, 1979.

[95] Chunyin Qiu and Tiezheng Qian. Numerical study of the phase slip in two-dimensional superconducting strips. *Physical Review B*, 77(17):174517, 2008.

[96] Umberto Nasti, L Parlato, M Ejrnaes, R Cristiano, T Taino, H Myoren, Roman Sobolewski, and G Pepe. Thermal fluctuations in superconductor/ferromagnet nanostripes. *Physical Review B*, 92(1):014501, 2015.

[97] T Yamashita, S Miki, K Makise, W Qiu, H Terai, M Fujiwara, M Sasaki, and Z Wang. Origin of intrinsic dark count in superconducting nanowire single-photon detectors. *Applied Physics Letters*, 99(16):161105, 2011.

[98] Allen Goldman. *Percolation, localization, and superconductivity*, volume 109. Springer Science & Business Media, 2013.

[99] LN Bulaevskii, MJ Graf, CD Batista, and VG Kogan. Vortex-induced dissipation in narrow current-biased thin-film superconducting strips. *Physical Review B*, 83(14):144526, 2011.

[100] John Clarke and Frank K Wilhelm. Superconducting quantum bits. *Nature*, 453(7198):1031–1042, 2008.

[101] TA Fulton and LN Dunkleberger. Lifetime of the zero-voltage state in josephson tunnel junctions. *Physical Review B*, 9(11):4760, 1974.

[102] DE McCumber and BI Halperin. Time scale of intrinsic resistive fluctuations in thin superconducting wires. *Physical Review B*, 1(3):1054, 1970.

[103] James S Langer and Vinay Ambegaokar. Intrinsic resistive transition in narrow superconducting channels. *Physical Review*, 164(2):498, 1967.

[104] Dmitri S Golubev and Andrei D Zaikin. Thermal fluctuations in superconducting nanowires. *arXiv preprint arXiv:0806.2959*, 2008.

[105] Nayana Shah, David Pekker, and Paul M Goldbart. Inherent stochasticity of superconductor-resistor switching behavior in nanowires. *Physical review letters*, 101(20):207001, 2008.

[106] Luigi Longobardi, Davide Massarotti, Giacomo Rotoli, Daniela Stornaiuolo, Gianpaolo Papari, Akira Kawakami, Giovanni Piero Pepe, Antonio Barone, and Francesco Tafuri. Thermal hopping and retrapping of a brownian particle in the tilted periodic potential of a nbn/mgo/nbn josephson junction. *Physical Review B*, 84(18):184504, 2011.

[107] L Parlato, D Salvoni, M Ejrnaes, D Massarotti, R Caruso, R Satariano, F Tafuri, XY Yang, L You, Z Wang, et al. The role of multiple fluctuation events in nbn and nbtin superconducting nanostrip single-photon detectors. *Journal of Low Temperature Physics*, pages 1–6, 2020.

[108] Xiaoyan Yang, Lixing You, Lu Zhang, Chaolin Lv, Hao Li, Xiaoyu Liu, Hui Zhou, and Zhen Wang. Comparison of superconducting nanowire single-photon detectors made of nbtin and nbn thin films. *IEEE Transactions on Applied Superconductivity*, 28(1):1–6, 2017.

[109] Ulla Wandinger. Introduction to lidar. In *Lidar*, pages 1–18. Springer, 2005.

[110] CMR Platt and RL Collins. Lidar backscatter. 2015.

[111] VCPJ Ramanathan, PJ Crutzen, JT Kiehl, and Daniel Rosenfeld. Aerosols, climate, and the hydrological cycle. *science*, 294(5549):2119–2124, 2001.

[112] Zhanqing Li, Jianping Guo, Aijun Ding, Hong Liao, Jianjun Liu, Yele Sun, Tijian Wang, Huiwen Xue, Hongsheng Zhang, and Bin Zhu. Aerosol and boundary-layer interactions and impact on air quality. *National Science Review*, 4(6):810–833, 2017.

[113] Albert Ansmann, Ulla Wandinger, Maren Riebesell, Claus Weitkamp, and Walfried Michaelis. Independent measurement of extinction and backscatter profiles in cirrus clouds by using a combined raman elastic-backscatter lidar. *Applied optics*, 31(33):7113–7131, 1992.

[114] KN Liou and Y Takano. Light scattering by nonspherical particles: remote sensing and climatic implications. *Atmospheric research*, 31(4):271–298, 1994.

[115] K Sassen. Lidar backscatter depolarization technique. light scattering by nonspherical particles, 2000.

[116] P Di Girolamo, D Summa, RF Lin, T Maestri, R Rizzi, and G Masiello. Uv raman lidar measurements of relative humidity for the characterization of cirrus cloud microphysical properties. *Atmos. Chem. Phys*, 9(22):8799–8811, 2009.

[117] P Di Girolamo, R Marchese, DN Whiteman, and BB Demoz. Rotational raman lidar measurements of atmospheric temperature in the uv. *Geophysical Research Letters*, 31(1), 2004.

[118] CM Penney and M Lapp. Raman-scattering cross sections for water vapor. *JOSA*, 66(5):422–425, 1976.

[119] James D Klett. Stable analytical inversion solution for processing lidar returns. *Applied optics*, 20(2):211–220, 1981.

[120] Albert Ansmann, Maren Riebesell, and Claus Weitkamp. Measurement of atmospheric aerosol extinction profiles with a raman lidar. *Optics letters*, 15(13):746–748, 1990.

[121] Yu F Arshinov, SM Bobrovnikov, Vladimir E Zuev, and VM Mitev. Atmospheric temperature measurements using a pure rotational raman lidar. *Applied Optics*, 22(19):2984–2990, 1983.

[122] Claus Weitkamp. *Lidar: range-resolved optical remote sensing of the atmosphere*, volume 102. Springer Science & Business, 2006.

[123] Hamamatsu Photonics K.K. *Photomultipler tubes, basics and applications. Third Edition.* 2006.

[124] Maria Moshkova, Alexander Divochiy, Pavel Morozov, Yury Vakhtomin, Andrey Antipov, Philipp Zolotov, Vitaly Seleznev, Marat Ahmetov, and Konstantin Smirnov. High-performance superconducting photon-number-resolving detectors with 86% system efficiency at telecom range. *JOSA B*, 36(3):B20–B25, 2019.

[125] Francesco Mattioli, Zili Zhou, Alessandro Gaggero, Rosalinda Gaudio, Saeedeh Jahanmirinejad, Döndü Sahin, Francesco Marsili, Roberto Leoni, and Andrea Fiore. Photon-number-resolving superconducting nanowire detectors. *Superconductor Science and Technology*, 28(10):104001, 2015.

[126] Chao Yu, Mingjia Shangguan, Haiyun Xia, Jun Zhang, Xiankang Dou, and Jian-Wei Pan. Fully integrated free-running ingaas/inp single-photon detector for accurate lidar applications. *Optics express*, 25(13):14611–14620, 2017.

[127] Jens Bösenberg and Volker Matthias. Earlinet: A european aerosol research lidar network to establish an aerosol climatology. 2003.

[128] Gianluca Pisani. *Lidar study of high density aerosol clouds: the Aerosol Multi-wavelength Polarization lidar Experiment*. PhD thesis, University of Naples Federico II, 2013.

[129] Kenneth Sassen. Lidar backscatter depolarization technique for cloud and aerosol research. *Light scattering by nonspherical particles: theory, measurements, and applications*, page 393, 2000.

[130] Andreas Behrendt and Takuji Nakamura. Calculation of the calibration constant of polarization lidar and its dependency on atmospheric temperature. *Optics express*, 10(16):805–817, 2002.